Eivind Hugaas

Long term material properties of pressure vessels made of composite material

Doctoral thesis

Eivind Hugaas

Doctoral theses at NTNU, 2022:56

NTNU
Norwegian University of
Science and Technology

NTNU
Norwegian University of
Science and Technology

NTNU

Eivind Hugaas

Long term material properties of pressure vessels made of composite material

Thesis for the degree of Philosophiae Doctor

Trondheim, February 2022

Norwegian University of Science and Technology
Faculty of Engineering
Department of Mechanical and Industrial Engineering

NTNU
Norwegian University of
Science and Technology

Preface

This thesis is submitted to the Norwegian University of Science and Technology (NTNU) in partial fulfilment of the requirements for the degree of Philosophiae Doctor, under the supervision of Prof. Andreas T. Echtermeyer and co-supervisor Assoc. Prof. Kaspar Lasn. This doctoral work has been carried out at the Department of Mechanical and Industrial Engineering at NTNU, Trondheim, between September 2017 and September 2020. This work was performed within MoZEES, a Norwegian Centre for Environment-friendly Energy Research (FME), co-sponsored by the Research Council of Norway (project number 257653) and 40 partners from research, industry and the public sector.

Abstract

Pressure vessels are currently the limiting factor in the hydrogen distribution chain. The pressure vessels are preferably made out of composite materials to achieve practical weight to strength ratios and avoid hydrogen cracking in steels, which is the alternative material. While composites are more environmentally stable and stronger, they are inherently more complex mechanically. To allow full use of the composite materials potential, better modelling and structural integrity monitoring methods needs to be developed.

In this work, methods have been developed to better model and monitor damage from mechanical loads on composite materials, with particular application to filament wound materials such as used in pressure vessels. The goal of the work is to allow better use of composite material's potential in hydrogen pressure vessels. The methods may achieve this by allowing better lifetime estimates and structural integrity monitoring along with increased understanding for the failure mechanisms.

The failure mechanisms and progressive fatigue damage was studied using digital image correlation (DIC) applied on split disk fatigue tests of pressure vessel cut outs. As part of this work a novel method for monitoring damage progression was used and suggested on the experimental level.

The DIC data was used to estimate S-N curves for the fiber direction on the local level using a novel method that may also be used as a damage monitoring method. The S-N curves were used as input for a fatigue damage model formulated as a user material subroutine (UMAT) in the finite element software Abaqus capable of modelling fatigue damage in composite materials. The UMAT and the experiment matched in terms of damage development.

Acknowledgments

I wish to thank my supervisor Andreas T. Echtermeyer for allowing me to chase my own ideas and pave my way in an interesting field. His critical voice and high level view helped me focus and make the work efforts concentrated and fruitful.

Special mention needs to be addressed to my great colleagues, providing interesting discussions and a friendly atmosphere at work, they are too many to mention.

Figure 1 Looking at the sunset at the end of a hard day's work.

Contents

Abbreviations and symbols
Abbreviations

AOI	Area Of Interest
CFRP	Carbon Fiber Reinforced Polymer
DIC	Digital Image Correlation
DOE	U.S. Department of Energy
FEA	Finite Element Analysis
FW	Filament Winding
GFRP	Glass Fiber Reinforced Polymer
MoZEES	Mobility Zero Emissions Energy Solutions
NTNU	Norwegian University of Science and Technology
PhD	Philosophiae Doctor
S-N curve	Stress vs N curve (N being number of cycles)
UEL	User defined Element, long version: User defined element subroutine
UMAT	User Material subroutine, long version: User defined mechanical material behavior subroutine

Symbols

	General	Material direction specific
Material direction, with examples:	ij	
Fiber direction	-	11
Matrix direction	-	22
In plane shear direction	-	12
Through thickness direction	-	33
General sign of peak/max value	$\hat{}$	$\hat{}_{ij}$
Tensional property	T	ijT
Compressive property	C	ijC
Strain	ε	ε_{ij}
Stress	σ	σ_{ij}
Poisson's ratio	ν	ν_{ij}
Stiffness in stiffness matrix	C	C_{ij}
Differential value	Δ	
Reduction factor	S	S_{ij}
Residual strain	ε_{res}	$\varepsilon_{res,ij}$
Cycles	N	-
E-modulus	E	E_{ij}
Shear modulus	G	G_{ij}
Traction directions:		
Normal direction (Mode I)	n	
First shear direction (Mode II)	s	
Second shear direction (Mode III)	t	
Max traction	t	t_n, t_s, t_t
Contact stiffness	K	K_n, K_s, K_t
Fracture energy	G	G_n, G_s, G_t
Exposure factor	f	f_{ij}
Slope of S-N curve	α	α_{ij}
Origin of S-N Curve	0	$\hat{\varepsilon}_{22T}^{0}$
Cumulative damage (Miner sum)	M	M_{ij}

Introduction

Research problem and motivation

The work in this thesis has the goal of contributing to increasing the capacity of hydrogen pressure vessels and ease the testing and verification regimes, particularly for vessels with wear and small damage. The research problem rests on the following arguments.

- A better understanding is necessary to answer how and how much wear and small damage in the laminate can be tolerated and dealt with. Currently replacement is required, not allowing for repair.

- Mechanical fatigue in composite components and particularly in filament wound composites is not well enough understood.

- Better understanding is necessary to optimize testing regimes. The testing and verification requirements are a cost driver for hydrogen pressure vessels.

Better understanding is achieved through a cycle of trial and error with learning as a result. The work presented herein is a result of trial and error through a three year period. Figure 2 illustrates the work cycle. The results are in the form of two main deliveries:

- An Abaqus UMAT user subroutine capable of simulating fatigue in composite components, with main appliance to pressure vessels.

- A monitoring method based on digital image correlation capable of monitoring fatigue damage and residual strength in composite materials.

The deliveries answer the industrial problem in the following ways:

- The UMAT can simulate how the vessels behave under high pressures over time.

- The structural integrity around worn and damaged areas can be monitored with the digital image correlation method, answering the damage state and structural integrity and condition of the vessel.

- The monitoring method can give better estimates of fatigue material properties than current testing standards.

The deliveries have been developed on the experimental stage. Industrial full scale testing still remain along with more experimental case studies to further verify the developed methods. The most valuable takeaway from the work is the concepts and ways of thinking as much as the final deliveries.

Testing and development of the methods have been described in three research articles:

Paper I - Filament wound composite fatigue mechanisms investigated with full field DIC strain monitoring.

Paper II - Estimating S-N curves for local fiber dominated fatigue failure in filament wound pressure vessels

Paper III - Progressive Fatigue Failure Analysis of a Filament Wound Ring Specimen with a Hole

Figure 2 The cycle of trial and error in the work presented in this thesis along with what paper belongs to which part of the circle.

Background

Introduction to composites

Composites are materials with several constituents that do not mix in production. They can consist of any two or more types of material. In this work the focus is on fiber reinforced polymers. The composite then consist of a matrix material; the polymer, and a fiber material which is usually carbon or glass fiber. Figure 3 shows the typical configurations. Unidirectional continuous or weaved (continuous) configurations are typical for high performance applications, ranging from pressure vessels to skis. Randomly distributed configurations may be found in less performance critical applications such as recreational boat hulls.
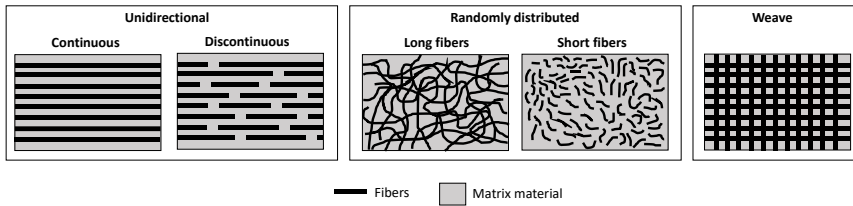
Figure 3 Different types of fiber reinforced polymers. The matrix material is typically epoxy and the fibers either carbon or glass fibers.

Unidirectional materials are commonly produced as a layup of several layers, together they make up a laminate. The layers serve different purposes, contributing to the stiffness in the direction which they are placed. Figure 4 shows a simple laminate consisting of a layup of two layers at right angles.
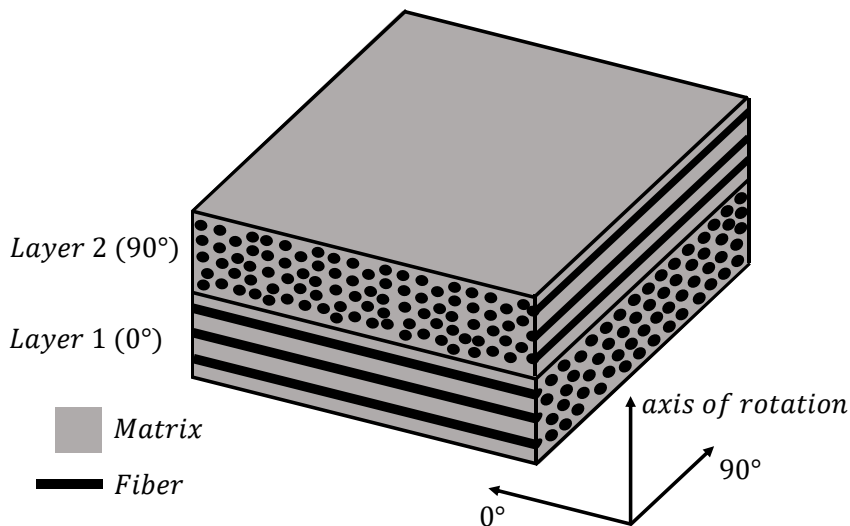

Figure 4 A simple laminate consisting of a layup of two layers.

The laminates are commonly produced by vacuum infusion. Prepreg manufacturing may be another alternative, where mats with layer(s) are pre impregnated with epoxy from the producer and commonly hardened by heat (thermosetting epoxy). In vacuum infusion, fiber mats are laid on top of each other in the wished configuration and epoxy is infused through the layup using a vacuum pump. The resulting layup can be as in Figure 4 if two unidirectional mats are laid on top of each other at a right angle. All layers are impregnated simultaneously using this method and this method is typically used for a wide range of applications from Formula 1 cars to skis. This production method is however not the preferred method for pressure vessels, then filament winding (FW) is used. In filament winding, one or more strands of fibers (typically up to eight strands) are wound onto a rotating mandrel. The fibers/strands are impregnated with epoxy continuously as they are wound, which is in contrast to vacuum infusion. Figure 5 shows a schematic of the method and Figure 6 the filament winding machine at NTNU used for the work in this thesis. Using the FW production method it is not possible to achieve exactly straight angles (0° and 90°) using conventional winding techniques. The very low angle layers are limited by the shape of the mandrel and the friction of the impregnated fibers against the mandrel. The high angle layers can however get close to 90°, usually 89°, but then without any winding around the cone part of the mandrel. When winding around the cone part, the layers get a woven layup of $\pm\theta$. The mandrel may be

left inside the structure or removed. Often it is left as a pressure liner or as part of the loadbearing structure or both.
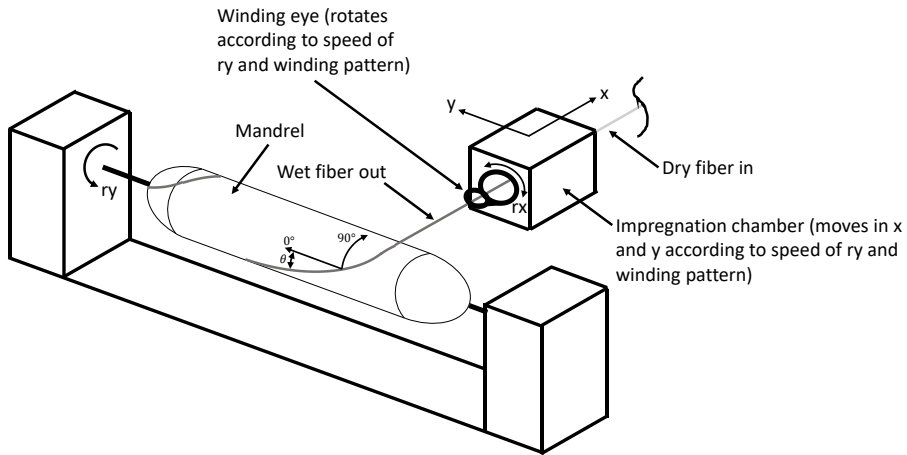

Figure 5 Schematic showing how a filament winding machine works.

Figure 6 The filament winding machine at NTNU winding a low angle glass fiber reinforced polymer layer. The rx axis is labelled "W" on the impregnation chamber.

Besides the production method itself, filament wound materials differ from vacuum infused layups in a number of ways on the microscopic scale. While the vacuum infusion production method is very controlled and stepwise, the filament winding production methods' variables are usually harder to control. The fibers will vary how they arrange themselves as they land on the mandrel and epoxy will never be impregnated equally throughout the process due to variations in the fiber and the curing process. A filament wound laminate will therefor be prone to more imperfections and variations in properties throughout the material than a comparable vacuum infused laminate. These variations are the focus of a large part of the work in this thesis.

Composite pressure vessels for hydrogen storage
Pressure vessels for hydrogen storage are divided into four main categories, type I – V, described in Table 1. The gas is preferably stored compressed, allowing for rapid refueling on par with liquid fuels. Due to the weight to strength ratio of carbon fiber composites and the

added security of having a liner, the type IV is the preferred alternative for storage. At high pressures, a type IV vessel may store 4 times as much hydrogen relative to the weight of the vessel than a type I or II [1]. The work in this thesis is based on type IV cylinders, only considering the composite material. Due to the novel nature of carbon fiber composites, testing and approval standards drive costs and likely limit the use of the material´s full potential [2, 3, 4, 5, 6, 7]. Better monitoring, modelling and testing methods may cut approval costs and allow for safer transport of hydrogen.

Table 1 Composite pressure vessel types.

Name	Description
Type I	All metal
Type II	All metal, but with composite overwrapped reinforcement in the hoop direction.
Type III	Fully composite cylinders with metallic liner.
Type IV	Fully composite cylinders with plastic liner.
Type V	Fully composite cylinders without plastic liner.

Interest in composite pressure vessel research has increased the past years as industrial interest has increased. The interest was expressed for automotive applications as early as 2003 by The U.S. Department of Energy (DOE) [8, 9] launching the 'National Hydrogen Storage Project'. The project allocated governmental funding to research along with industry partners and set clear performance goals on the storage solutions. The type IV pressure vessel storage solution was a big part of the research and showed promise. Today the type IV can be found in commercially available vehicles at the target pressure expressed by DOE of 700 bar, proving that investments in the technology gives results.

So far the type IV research efforts have for the most part focused on vessels for onboard storage in automobile applications and how the tank design may be optimized in smaller cylinders. One research project in particular stands out, the OSIRHYS IV project. The project was aimed at developing and validating models and methods for design and optimization of high pressure type IV vessels [10]. Despite the project only focusing on the static case (not fatigue), it proved how finite element analysis may predict and optimize vessel design. The current academic status is that the static load case is possible to model with a high degree of accuracy in pressure vessels, but the fatigue case remains at large unexplored. This is no surprise considering the complex nature of composite materials, adding the time component naturally increases the complexity to a point where it is hard to handle. The models in the OSIRHYS IV project were full scale and with enough detail to catch all effects.

In 2017 the Norwegian Research Council launched MoZEES (Mobility Zero Emissions Energy Solutions). MoZEES is a Norwegian Research Center on Zero Emission Energy Systems for Transport (Mobility Zero Emissions Energy Solutions). The project focus on battery and hydrogen value chains. This PhD is part of the hydrogen value chain.

Fatigue and damage mechanisms in composites

The distribution and development of damage, strain and stress fields over time in a composite component subjected to cyclic loading is dependent on how the forces are distributed within the material between the fiber and the matrix. While the fibers carry the load, the matrix distributes the load between the fibers. Throughout cycling, the amount of fiber failures and matrix failures will gradually increase [11]. At some point, enough fiber failures will have coalesced to form a macro failure, upon which the laminate is visibly destroyed. Before this stage, failure occurs on the micro level.

Fatigue failure propagation is schematically explained in Figure 7 for a small piece of composite loaded in the fiber's direction at high and low load. Depending on the loading and the properties of the fiber and the matrix, the failure will propagate with varying extent of matrix splitting/debonding to interconnect weaker imperfections in the fiber and in the matrix [11]. Ideally, the failure would propagate as a straight crack, however, material imperfections

make the crack change direction. Figure 8 shows the different failure mechanisms and imperfections relevant for this work schematically. How the fiber imperfections are distributed depends on the production and is as such a fiber property [12], the matrix voids are introduced in the production of the laminate and is a laminate production property. The filament winding production process induces a particularly high amount of matrix voids and imperfections compared to vacuum infusion.

For low loads in the fibers' direction, matrix damage needs to travel further than for high loads to find large enough imperfections in the fiber to travel through. Pardini et. al. found that for single strand tests of GFRP and CFRP the static failure load decreased with increase in fiber length as more and bigger weaknesses were exposed to loading [13]. Mandell et. al. [14] found that the S-N curves of perfect glass fibers have a slope of 3% in a linear log diagram, a lot less than 10%, which was found as the slope for the composite material in the same study. The results of Mandell and Pardini confirm that fatigue grows through imperfections in the fibers, as imperfection free fibers have superior fatigue life.

The nature of the matrix failures connecting the fiber failures can vary between all the mechanisms described in Figure 8, including delamination. Work by Seyhan [15] indicates that high cycle/low load fatigue is more prone to fiber debonding, while low cycle/high load fatigue favors matrix splitting to a greater extent. It is important to keep in mind that schematics and theory are often displayed in the 2D format, however, failure is a 3D phenomenon and must be treated as such, therefore it is very likely a combination of all failure mechanisms that leads to final catastrophic failure. However, as indicated by Seyhan, it is to be expected that different failure mehcanisms may dominate at different loads and loadcases as outlined in Figure 7.
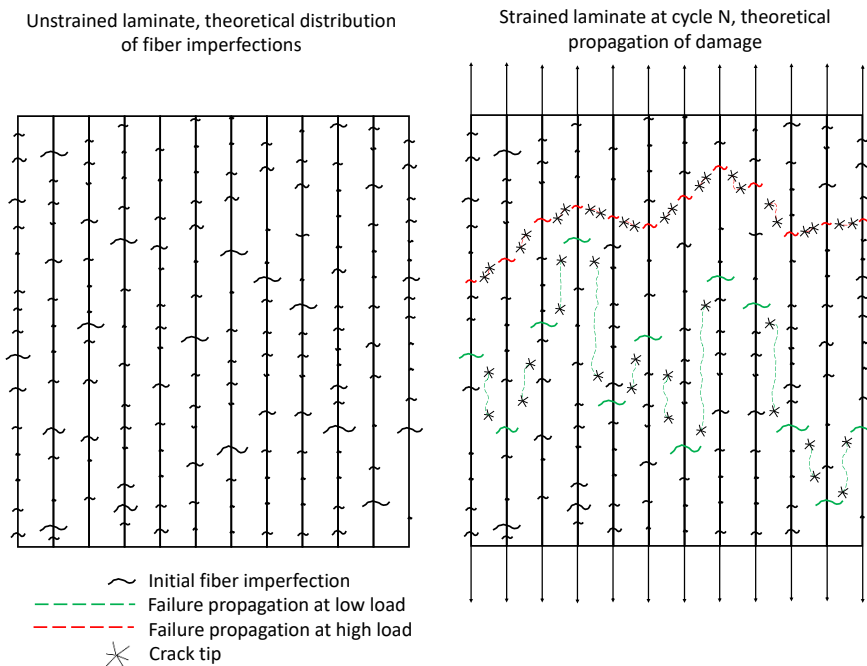
Figure 7 Schematic of failure propagation for high and low load at an arbitrary cycle.

The matrix also contains imperfections, voids being the most important. In an otherwise uniformly loaded laminate, locally uneven strain fields will be induced through variations in fiber volume fraction, initially broken fibers and void content. The locally uneven strain fields will drive damage in the matrix and consequently in the fibers. The higher the void content, the faster the matrix will split, delaminate or debond with the fibers. Fiber failure will induce

shear in the matrix along the fibers and the degree of shear will depend on how far the failure needs to travel before it finds the next imperfection to travel through.
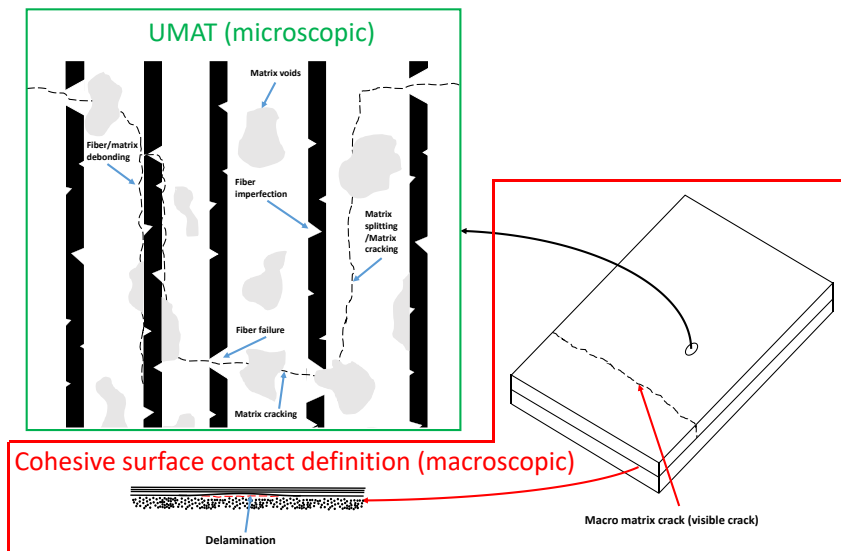

Figure 8 Damage mechanisms and imperfections in a composite.

Seeing as the matrix acts as the load distributor for the fibers, progressive matrix failure throughout cycling will alter the initial strain fields. Given a geometric strain concentrator, such as a hole or some arbitrary initial damage, strain concentrations may move throughout cycling. This can be advantageous, potentially alleviating geometric strain concentrators from design or damage. Complementing this is work by Plumtree et. al. [16] who observed that for short cycle fatigue, the failure propagation will favor fiber failure to a higher degree and the redistribution will be less and global failure more sudden.

The failure mechanism explained above have theoretically been described with the shear lag theory and several modifications of this [17]. The shear lag theory describes how forces are distributed in a fiber that is embedded in a matrix with varying degrees of debonding. Imperfections in a composite can vary from production batch to batch, it is therefore somewhat difficult to apply the shear lag micromechanics model to predict failure given a specific material [17]. By employing high frequency DIC, the strain trends and material behavior should be observable and explainable with the outlined micromechanics.

Basic challenges

The main challenge with the work has been the broad scope and the search for an absolute answer formulated for industry and also academia. That means finding methods that are simple enough for industrial implementation while still fulfilling the quality requirements of scientific work. Finding a balance between the two and striking a line of pragmatism has been the key to success. For example, common testing procedures could easily have set two pressure vessel materials apart. However, developing methods that has the potential to predict the lifetime and capacity of any pressure vessel and material has required looking beyond already established testing and modelling methods. It has required being innovative while not complicating the problem too much, again finding the fine line of pragmatism necessary for industrial use.

Steel is the most common material to compare with composites. If weight to strength is an issue, composites may serve as a viable alternative to steel in designs. Design wise, composites are markedly different from steels. Composites are also fairly novel materials compared to steels, using them in design therefor raises several questions that the steel

alternative may answer in a more exact manner using established procedures. Fatigue life is one of the issues where composites behave differently from steels and where steels have established procedures and standards to account for fatigue issues analytically [18]. Figure 9 illustrates the difference in fatigue behavior for a composite and a steel plate with a hole loaded cyclically over time. The main differences between the two are:

- Composites will have a gradual change of structural response throughout cycling. Steels will, in comparison, be relatively stable up until failure, at least compared to composites.
- The strain and stress distribution may change markedly in a composite component throughout it's lifetime, substantially more than yielding in a metal (yielding is not illustrated in Figure 9).
- Variations in material properties in a composite component may give variations in progressive fatigue damage throughout the component in question.
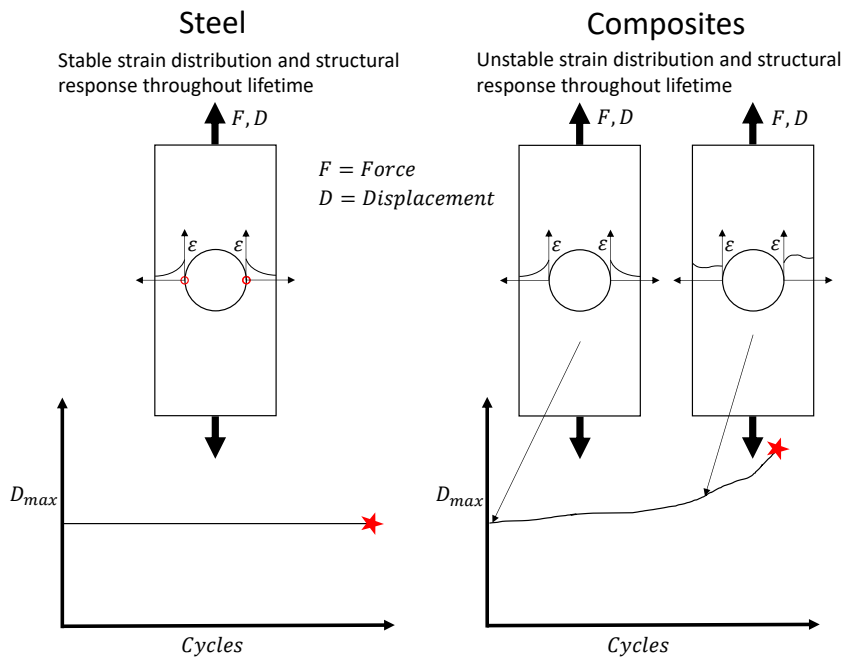

Figure 9 Difference in strain distribution and structural behavior for a steel and a composite.

There are in other words two main issues to consider in fatigue of composite materials, it's progressive nature and it's variation. While a steel component will be subject to a short period of crack growth towards the end of life, a composite component may have crack growth occurring steadily throughout it's lifetime. While a crack in a steel component affects the loadbearing capacity, a crack in a composite may not to the same degree. The reason for the difference is that a crack in a composite will prefer to evolve in the weaker of the two constituents; the matrix, as outlined in section Fatigue and damage mechanisms in composites. Though the matrix is extensively cracked or damaged, the component in question may still have a high residual strength, as the fibers may at large be intact. The strain and stress fields will however change as the matrix cracks. Seeing as the matrix contains a varying amount of imperfections, particularly with the filament winding production method, the damage progression will vary, as outlined in Figure 9.

A damaged matrix may or may not be critical depending on the application. For steels, up until crack initiation, the structural integrity and constitutive behavior of the component in question is stable. Life until crack initiation is taken as the design life. Only in special cases

can crack growth be allowed. Strain and stress state for fatigue calculations can therefore be taken from a static model as the mechanical behavior does not change throughout the lifetime. For a composite component, the same approach may not be valid if matrix cracking is allowed for the application in question. Models of the component, analytical or numerical, have to take into account the change of the strain and stress fields as the matrix accumulates damage. Progressive fatigue damage models are needed when investigating fatigue damage in composites.

Numerical models using the finite element analysis (FEA) is the most used method to model components in industrial and academic work. The FEA method can model explicitly or implicitly formulated problems. The explicit method are used for time dependent events where the mass of the system plays a crucial role, typically impact modelling. Implicit methods are used for quasi static loading where the mass is arbitrary. While fatigue damage is a time dependent mechanism, the mass of the system is commonly not critical to the structural response, it is at large a quasi-static system loaded in a cyclic fashion. Implicit modelling is therefor the preferred analysis method. The key challenge when modelling progressive fatigue damage using FEA is the brittle nature of matrix cracking, making for a negative tangent stiffness locally upon cracking. While the explicit method may handle some negative stiffness locally due to mass damping, the implicit method is not capable of this. The iterative schemes are not capable of finding a solution when the stiffness changes suddenly on the local level [19]. Getting around the issue of modelling brittle failure in implicit models was solved and the method presented in Paper III. The method is, as most modelling, an approximation justified with experimental data.

Paper I explores how fatigue damage evolves in filament wound materials and provides a basic understanding; highlighting how the larger part of the fatigue life is dominated by matrix damage as outlined in Figure 9. It was found that catastrophic fiber failure in fatigue may first occur when the matrix material is sufficiently damaged for fiber rupture to travel through the structure.

In order to properly model fatigue damage, correct and descriptive material properties are needed. Fatigue properties are typically taken from coupon testing, both for metals and for composites. For metals, this approach is sound, the local strain field at the neck is easy to measure and stable up until crack initiation, soon followed by crack propagation and catastrophic failure. For a composite component, the strain field around the neck region may evolve throughout cycling and first point of failure may move as outlined in Figure 9 and Paper I. Paper II addresses this issue and presents a method for finding local fatigue properties that can be used as input in finite element analysis. The paper utilize DIC of split disk fatigue tests to investigate local strains in the material. Paper II focuses at large on the fiber direction, attempting to describe catastrophic failure. Paper II also investigates the inherent variation in static and fatigue properties for filament wound composites. It was concluded that catastrophic failure may be described by higher S-N curves relative to that found by common standards.

Paper III uses the fatigue properties from Paper II and shows the correlation between experiment and model.

There are three main conclusions from the work presented in this thesis:

- Variation in material properties in filament wound components may be extensive.
- The fiber may locally be much stronger than what is found in common coupon tests.
- It is possible to use pragmatic approaches to model damage in composite pressure vessels.

Past work

Past work on fatigue in composites

The larger part of research on fatigue in composites has been done on flat laminates with simple layups and no or simple imperfections. The huge amount of possible combinations of material parameters makes it a difficult topic to study taken the initial complexity of fatigue into account. Most papers try to come up with other ways to formulate the S-N curve other than the log-log or linear log shape or try to improve the Miner fatigue cycle counting. However, thus far both mentioned approaches remain the benchmark in academics and industry. Talreja et. al. [11] give a good introduction explaining the basic principles of composite fatigue. For an overview of the more recent research, Degrieck and Paepegem [20] give an excellent review. Degrieck sums up the research in three major categories; the conventional S-N approach, models for reduction of stiffness and strength and progressive failure models. The first two operate on the global level, giving the fatigue life of the composite component with all its layers as one unit. The progressive failure models differ from the two others in that they take into account material damage mechanisms such as matrix cracking and delamination and how these spread during fatigue loading, much like crack propagation in linear elastic fracture mechanics for metals. The progressive failure models are not limited to a certain layup and as such are more universal and also very well suited for numerical implementation in simulation software. The work in this thesis is based on simple progressive failure models.

The review of Degrieck and Paepegem leaves the reader somewhat baffled by the shear amount of developed models, which has perhaps become a problem of research on fatigue of composites. It is easy to make a model applicable for specific (load) conditions and specific materials; however the field lacks general applicable progressive failure models. For generality, simplifications such as using the Miner rule and S-N curve approach as for metals is more or less the only option for design. However, there is much research indicating that standard models for fatigue as adopted from metals lacks accuracy, sparking research often resulting in too specifically constrained models, as mentioned. More general alternatives to the Miner approach were proposed quite early by Broutman and Sahu [21] and Hashin and Rotem [22], both models along with the Miner approach and a new model proposed by Epaarachchi are compared with general composite materials and relevant load cycling by Epaarachchi and Clausen [23]. Considering the use of classic S-N curves, Mandell et al. [24] carried out a large amount of fatigue tests on composites intended for wind turbines and concluded the findings on a trend basis that gives a good indication of what S-N curve parameters are reasonable to use.

Considering fatigue of damaged composite specimens, particularly relevant for pressure vessels sustaining wear and damage during their lifetime, less research has been carried out as most studies deal with flat nondamaged specimens. However, for a pressure vessel application there are many useful constraints that limit the scope. It is reasonable to assume that all of the fatigue loading will be in tension-tension and that the relevant layups will be close to a cross ply layup (0°/90°). Also, for a damaged specimen it is reasonable to assume that the load will be very high in the area surrounding the damage, albeit with the same load ratio. From an application point of view, the residual burst pressure of the vessel given a damage will be equally relevant as knowing remaining cycles/lifetime, limiting the scope to the residual strength models. As such, if the residual strength at a certain cycle number considering damage is possible to calculate, calculating the residual strength at lifetime will also be possible given a cumulative damage criterion, such as the Miner rule [25]. For numerical modelling purposes, such as in a finite element model, it will be required to not only know when and how the laminate will fail in a given direction, but also know how the mechanical constants will evolve in case of failure. This brings up the relevance of the progressive failure models which describe how the mechanical properties are degraded. Provided a solid understanding of the numerical engine of choice, pragmatic approaches can be applied for degradation of mechanical properties and accumulation of damage.

Regarding already existing residual strength models, Philippidis and Passipoularidis [26] made a review of residual strength models and compared them to experimental data. They interestingly found that despite many models having great complexity, they did not deviate noteworthy from a linear degradation as proposed by Broutman and Sahu [21] in the early days of research on fatigue in composites. Philippidis and Passipoularidis made a short and consise conclusion that describes the state of the art well, cited here.

"The main conclusion is that the use of complicated phenomenological models requiring large experimental data sets for implementation does not necessarily pay back in terms of accurate predictions and consequently simple models requiring limited experimental effort should be preferred." Philippidis and Passipoularidis [26].

Philippidis however noted that it is reasonable to distinguish between residual strength and fatigue performance for high loads/low cycle and low loads/high cycle, which others also have found [27, 28]. A linear degradation will predict fair residual strength for high loads, while it will be on the safe side for lower loads. For this purpose, residual strength models are usually divided into sudden death and wearout models [29]. Sudden death models entail that the initial strength of the laminate is upheld until just before it breaks and are best applicable for low-cycle fatigue. Wearout models suggest a more gradual decrease of the strength and are better suited to describe high-cycle fatigue. While it is of interest that the pressure vessel can sustain a large amount of cycles as damaged, the stress and strain surrounding the damage will still be high, therefore research on low and high cycle fatigue is equally relevant. Harik et al. [30] investigated this and found that the S-N curve steepens at high loads indicating that a damaged specimen will have a quick propagation of damage until it is eventually distributed over a larger area or possibly fails. Bunsell and Thionnet have several publications addressing pressure vessels and their residual life if damaged, such as ref. [31] with Blassiau as main author. However, they are also very specific with fairly elaborate models. Perhaps more pragmatic is the work by Weng et. al. [32]. Weng developed a fatigue model based on micromechanics that seems to predict fatigue life for both filament wound and vacuum infused specimen reasonably well, however, that is provided a stable load ratio and fatigue load. It is important to underline that the model by Weng only works on the micromechanic level and is not capable of modelling anything but simple square specimen.

After a damage criterion has been breached, some way of degrading the constitutive material properties will have to be employed in order to model progressive damage in a numerical model. The simplest method is to degrade by a factor, for example 90 % reduction of longitudinal E modulus in case of fiber failure. Shokrieh and Lessard [33, 34] successfully proved the validity of this pragmatic approach. Shokrieh and Lessard made a numerical model where failure modes were identified and the constitutive material properties degraded by a constant factor upon breaching of the failure envelope defined by residual strength. They compared their model with experimental data and found a satisfying correlation. The failure criteria models employed were reasonably simple, using root squares of relevant stresses in respective directions to define failure. Degradation of residual strengths were done by employing a modification of the fatigue model developed by Adam et. al. [35]. This model is based on a logarithmic degradation and is fairly complex using many parameters. More elaborate models for degradation of mechanical properties have been employed analytically and numerically by others [26, 36, 37, 38, 39, 40, 41, 42]. However, consensus is still split on what approach yields the best results and seems to depend a lot on the loadcase, at least if compressive loads are considered.

Considering theories for accumulation of damage, there are models for both residual fatigue life and residual strength. These are equivalent as proved by Hashin [25]. The most well known theory for accumulation of fatigue damage is the classic Miner rule [43], which is the established standard for metals. The biggest dispute regarding accumulation is how the load block sequence influence fatigue life. The dispute boils down to whether a high load block before a low load block is worse than the opposite. In real life applications of course this debate is somewhat arbitrary as the component likely will experience many different loads

over time. Despite much work on the field and many proposed theories, the Miner rule still remains as the benchmark [29].

Besides the accumulation of damage, the degree of mulitaxiality is a key parameter to study. At large, fatigue damage can either occur in the matrix or in the fiber. However, how the different strain and stress components affect both of these two and how they may interact is a hot topic for research. On the theoretical level this is taken care of by several progressive failure models that take into account the different failure mechanisms. However; to what degree they are able to capture the full effect is questionable as most studies have a limited scope experimentally. Currently there is no standard approach, however many studies attempt to approach the problem by modifying already existing theories for multiaxial loading for static failure and use them in fatigue. One such study exemplifying this approach is that by Liu and Mahadevan [44]. They combined the Tsai-Hill static failure criterion with the Miner damage rule to construct a multiaxial accumulative fatigue damage criterion, which predicted fatigue failure reasonably well. Another is that by Shokrieh and Lessard [45, 46], they conducted a thorough review of the most basic theories of composite fatigue and suggested their own based on a combination of already existing theories. Shokrieh and Lessard pointed out that most existing theories need unreasonably many input parameters, making them inconvenient and hard to apply, at least for the industry.

Perhaps the biggest difference between fatigue and static failure is the importance of the matrix material in fatigue damage. For both fatigue and static loads, fiber failure is most often regarded as the most critical failure. However, the stress and strain concentrations in the fiber will depend on how the matrix distributes the forces between the fibers, for fatigue this may change significantly over the fatigue lifetime, as shown in Figure 9. As the matrix gradually cracks and weakens, the stress and strain concentrations can relocate, allowing for fatigue failure of the fiber in another location than what would be assumed based on the stress and strain distribution in the non-fatigued state [47, 48].

Despite all the available research, little work has been carried out using currently employed failure criteria by industry design engineers. Seeing as there is little consensus as to what other alternatives should be chosen, basing research on currently used standards for fatigue of composite components is highly relevant and a good baseline for further development in the field and in the industry, essentially answering how accurate those are. What is perhaps also lacking is employing fatigue models on datasets that have a high degree of randomness and not tailored to test specific aspects of a model. Most research tests models on carefully chosen load schemes such as two blocks of high and low load in near perfect specimen. It would be a step forward to test non-ideal specimen. Employing methods that generate large datasets from experiments, such as DIC, make this approach possible.

Modelling of damage in composites

Modelling of mechanical problems in the context of the current research front is typically seen as a problem formulated for computation by computers through some framework, typically the finite element analysis framework. The word "modelling" brings up images of complex 3D models with strain and stress fields displayed as a contour map over the analyzed part. This is a somewhat fairytale image of reality. The computational framework needs to deal with material models that look quite a bit more boring than fancy 3D-renderings. Luckily the material models can be formulated in a much simpler manner than what the 3D-rendering looks like. While all of the theories presented by Degrieck and Paepegem [20], mentioned above, are models in that they attempt to model reality using some predefined input, a FEA model is also a model. The two look quite different. The FEA model, despite it's apparent complexity, may be based on any of the models reviewed by Degrieck and Paepegem. The above chapter is as such also about models, this chapter however, will attempt to give an introduction to the computational models that have been made to model mechanical fatigue in composites.

The key problem in computational frameworks when dealing with progressive failure in composites is the brittle nature of the failure mechanisms combined with the time dependent

nature of fatigue damage. Both fiber and matrix typically fail in a brittle manner by cracking in some form, as demonstrated in Figure 7 and Figure 8. There are at large two ways to deal with this behavior. Either by cracking modelled as separation between elements or modelled as changes in the stiffness in the integration points, typically using a user defined material model. Most FEA programs already provide routines and methods to deal with the separation approach, though most commonly only with a force/displacement dependent behavior, not time/fatigue dependent. For the separation approach, the crack direction needs to be known as not all elements can be allowed to separate, this would be very computationally expensive, though not impossible. Recent developments in such models have managed to satisfactorily predict matrix damage dominated fatigue crack propagation in laboratory test specimen having simple geometries and known direction of crack propagation, e.g. Turon [49] and Nixon-Pearson et. al. [50].

While the separation approach essentially splits the structure and is a physical representation of a crack, modelling the cracking as changes to the stiffness in the integration point yields one big challenge, a discontinuous and negative local stiffness curve upon cracking. Attempts of simplifying the matrix crack growth by smearing matrix cracking over a larger region and modeling it by plastic behavior with a user defined material model were reported for the static case by NASA [51], Flatscher et. al. [52] and Gagani et. al. [53]. It is however difficult to tell whether the plasticity approach matches experiments only for the particular geometry of the specimen investigated or whether it is a general way to model the material. This is due to the fact that the material is not plastic on the size of the elements, it is inherently brittle. Perhaps the most promising method to approach the problem in a fatigue context is by using cycle jumping as explored by Koch et. al. [54], also used and explained in Paper III. Koch found that a cycle jump approach with constant properties for each loading cycle had to be applied. Degradation was carried out between the jumps according to the size of the cycle jump. A similar approach is used in this work. Turon [49], perhaps the most extensive work done on composite fatigue FEA models thus far, also had to use the same approach and his PhD gives a good in depth review of the method, a short form which can be found in Paper III.

Recently there have been attempts at combining the two approaches using a user defined element subroutine (UEL) on elements in between the normal elements to allow for separation between all the elements of the model. The UEL acts as glue in between the elements of the model and make them separate when enough energy is supplied to the UEL using classical fracture mechanics theory. This is basically the same approach as when modelling with a predefined crack direction, however, it is a large step forward to have the pre definition apply to the whole model, enabling the crack to grow "freely". For the static case, Rozylo [55] satisfactorily managed to model crack propagation without predefined crack directions using the cohesive zone modelling approach in combination with an UEL with promising results.

Still, all the above mentioned models are relatively academic and not easy for the average design engineer to implement or to get the correct input data for. The models have been developed with lab experiments in mind and not real designs. In this PhD work, the model was developed with the design engineer in mind and then tested on a complex lab experiment. This work therefor has a somewhat different format than most academic publications covering the topic, having a wider scope and less in detail investigations of the experimental results and modelling. This work would however not have been possible without the past academic literature going in depth in DIC and Abaqus in particular.

There are currently some commercially available composite mechanical fatigue numerical frameworks available, most notably FEMFAT [56] and Fe-safe [57]. While the models offer simple and fast fatigue evaluations, they do not include progressive damage and do fatigue analysis based on a static solution. The models are only tested on simple lab coupon specimen and lack experimental comparisons with local strain fields. Recent developments have expanded a modified smearing approach into mechanical fatigue, most notably by Koch et. al. [54]. This takes progressive fatigue damage into account.

Prior application of DIC on composite materials

Monitoring of strain using DIC has been done successfully before and comparable experimental data is readily available. One of the more thorough studies using DIC in a composite fatigue context is that by Broughton et. al. [58]. Broughton investigated fatigue of flat GFRP specimens using DIC and found considerable redistribution of strain in the specimen during cycling. However, due to software limitations, the test had to be stopped for each DIC image and the images were only taken every 10 000 cycle, not capturing the end of life strain development. Employing more powerful software to synchronize the test machine with the image acquisition software was successfully done by Giancane et. al. [59], but lacked further analysis of results. Muc et. al. [60] conducted fatigue tests in the longitudinal direction of pressure vessel cutouts using 3D DIC and found that the results were consistent and easily comparable with FEA. Makeew et. al. conducted short beam shear fatigue testing with DIC [61, 62] and conducted thorough analysis of the results obtaining consistent fatigue data.

Though DIC provides good comparison with numerical models, little work has been done investigating the potential that lies in using the strain output from the DIC directly to evaluate fatigue behavior. This approach is equivalent to running the fatigue damage material model of a numerical model on strain not from the numerical model, but from the DIC. Essentially removing all assumptions related to the material behavior demanded by a numerical model, only focusing on the actual damage model. Employing this approach allows for checking more models than in a numerical model, due to that implementation and runtime is much shorter. The traditional process of comparing strain output with a numerical model is illustrated schematically in Figure 10 on a specimen tested in tension with a hole. As can be seen, the fatigue degradation model is implicated by several assumptions other than those directly in relation with the fatigue model itself. This poses a major challenge. Additionally, the strain distribution is symmetric in the numerical model. If an asymmetric distribution is to be achieved that resembles the DIC, even more assumptions would have to be added, implicating the fatigue model further. With educated guesses, the assumptions can be made just, and the approach as such defended. However, an alternative method that better isolates the degradation model would be advantageous.
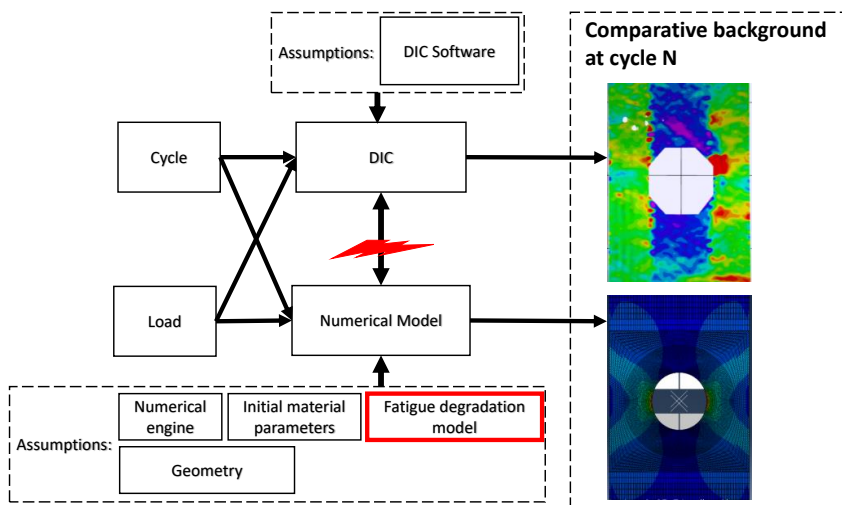

Figure 10 Schematic showcasing the problem encountered when comparing a numerical model with DIC strain data on a specimen with a hole tested in tension.

Paper II and Paper III outline an alternative method that instead of applying the fatigue degradation model to the strains from the numerical model only, applies it also on the strain history from the DIC. The method allows finding S-N curves that apply locally. Provided that the DIC software is set up correctly this eliminates the additional assumptions associated with the numerical model and introduces the asymmetry as it is in the actual specimen. Both standalone and particularly if combined with a numerical model as in Paper III, this approach

validates the fatigue degradation model in a way that leaves little room for educated guesses and arbitrary assumptions. For the more traditionalist researcher this approach may seem ardous and arbitrary as it is impossible to have control of each DIC data point. However, even though it may well be that there are some data points that are false, the shear amount of data is so large that it very much trumps this argument. Another argument for employing this sort of testing is that it's in line with current developments on the cutting edge of data processing and research in general. Taking it one step further, the strain to cycle curves of each individual point can be used to extract multivariable S-N curves. Combined with modern data processing tools, such as machine learning and neural networks, this holds great potential. Vassilopoulos and Bedi [63] used an adaptive neuro-fuzzy inference system (ANFIS) on a big dataset from normal fatigue tests of composites and managed to successfully predict S-N curves for any combination of ply angle and stress ratio, proving that modern data processing tools holds great promise within this field. Further, Golewski et. al. [64], recently managed to estimate the fracture toughness in concrete using DIC by tracing crack propagation and crack tip strain. Expanding the methods used by Golewski and combining it with big data algorithms on DIC data from fatigue testing may one day enable very accurate estimates of progressive fatigue failure mechanisms and S-N curves. The work in this thesis may inspire to taking such approaches into the composite fatigue field.

Materials and Methods

Materials

Composite pressure vessels are commonly made out of CFRP. In the work in this thesis, GFRP has been used instead. In the composite group at NTNU we have one GFRP composite material that has seen extensive work by several PhD candidates and master students through an eight year period. Characterizing a composite material is a time consuming process and not necessarily as straight forward as for a metal. Using already established material data can therefore be very advantageous from a time and work focus perspective. The GFRP material was therefor used instead of CFRP. The material is the HiPerTex W2020 fiber produced by 3B [65] with resin Epikote MGS RIMR 135 mixed with curing agent Epikure RIMH 137, both produced by Momentive [66]. CFRP and GFRP behave fairly similarly mechanically as they are both a strong fibrous material embedded in a weaker matrix. Research on GFRP is therefore equally relevant for CFRP, at least when considering general methods for modelling and monitoring damage in composites.

Split Disk Testing

The split disk test setup is a way of testing tensile properties in the hoop direction of specimen with ring geometry. It consists of two disks that are pulled apart. It is a convenient method of testing cut outs from pressure vessels or other tubular components. Pressure testing of the vessels on the other hand is a cumbersome process as only one vessel can be tested per vessel produced. The split disk setup is simple and may test several specimen from the same vessel. Figure 11 and Figure 12 shows the split disk test setup used in this thesis.

Figure 11 The split disk test setup used in this thesis. White tape is used on the steel tension arms to hinder reflections of light for DIC cameras.
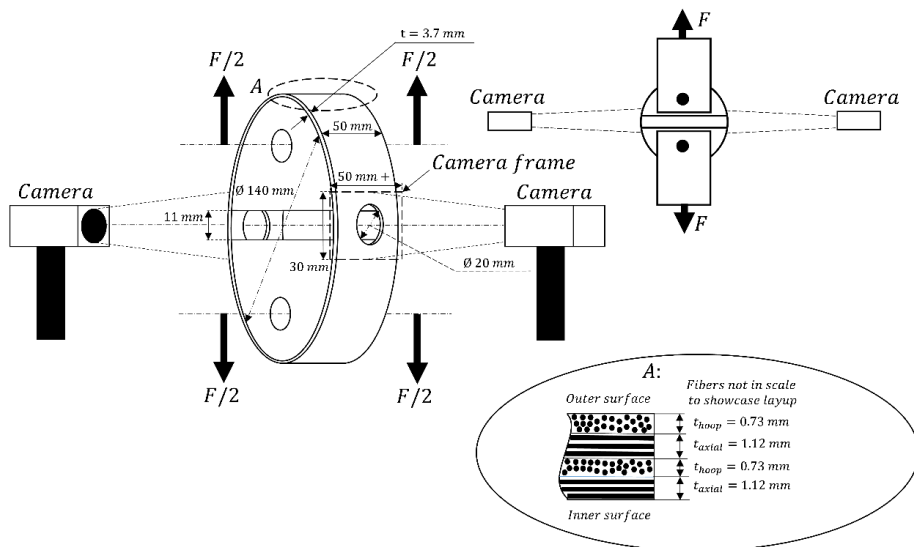

Figure 12 Schematic of the split disk test with DIC camera setup along with dimensions and the layup of the tested ring specimen.

The main challenge with the split disk setup arises from bending occurring in the split, as outlined in Figure 13. The bending is the main weakness of the split disk setup and is what constitutes the main challenge when using the split disk for estimating tensile properties. The bending will affect different layups differently depending on their stiffness and the resulting stress and strain in the material can be difficult to estimate exactly. For monitoring and studying damage development however, the bending effect is convenient as it concentrates the damage development around a relatively small known area. Particularly when combined with an imperfection, such as a hole, as used in this work, the area that will develop damage is very predictable. This is in contrast to classic tab test specimen of flat composites, which traditionally often fail at the grips, making damage monitoring inconvenient.
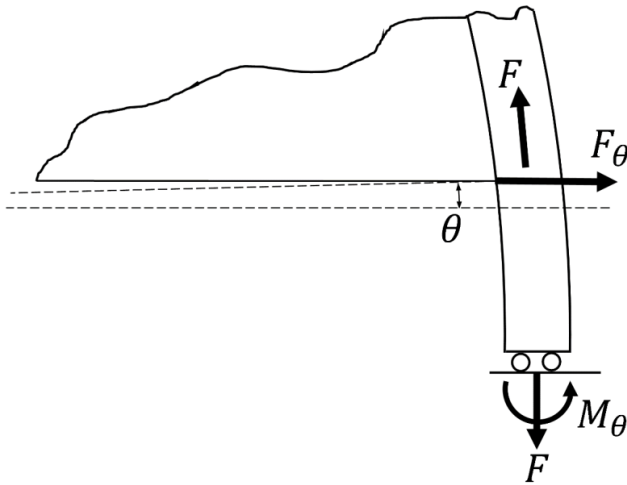
Figure 13 Schematic representation of the mechanical equilibrium in between the splits in the split disk setup.

Despite the apparent simplicity of the split disk setup, many papers are concerned with finding alternatives to the split disk test. These papers mostly investigate ways to obtain direct measure of the hoop strength avoiding the natural stress concentrations caused by the split in the classic split disk test setup. Such test rigs usually require tight tolerances on specimen geometry and are complex compared to the standard split disk test fixture [67, 68, 69].

DIC

DIC (Digital Image Correlation) is a technology for reading full field strain from images of a deformable body. It relies on recognizing patterns in an area of interest (AOI). Th,ese patterns are normally in the form of speckles. Figure 14 outlines the method and will be explained in the following. To the left in the figure is a typical AOI over a speckle pattern over some deformable body. The AOI is divided into squares with a certain size. The squares are called subsets. The subset size is relative to the speckle pattern and should ideally contain three or more speckles of relatively even size [70]. The speckles in the figure vary quite a lot in size and the speckle pattern is as such sub ideal. The step size says how many subsets are put on top of each other, adding vector points without reducing the subset size. There are there for two ways to increase the resolution, smaller subset size or smaller step size. However, it is only the subset size that decides what variations in strain over the body that is recorded, while the step size will give more data points, advantageous for noise cancelling, for example. To the right in the figure is the deformed state of the speckle pattern. The deformation of the subsets are given as vectors in the vector points using classic deformation gradient theory. The method is as such comparable to classic finite element analysis with elements being subsets and integration points steps. For the work in this thesis the Vic-2D software from Correlated Solutions was used to post process the images and give strain data files. Vic-2D is an industry standard DIC software.
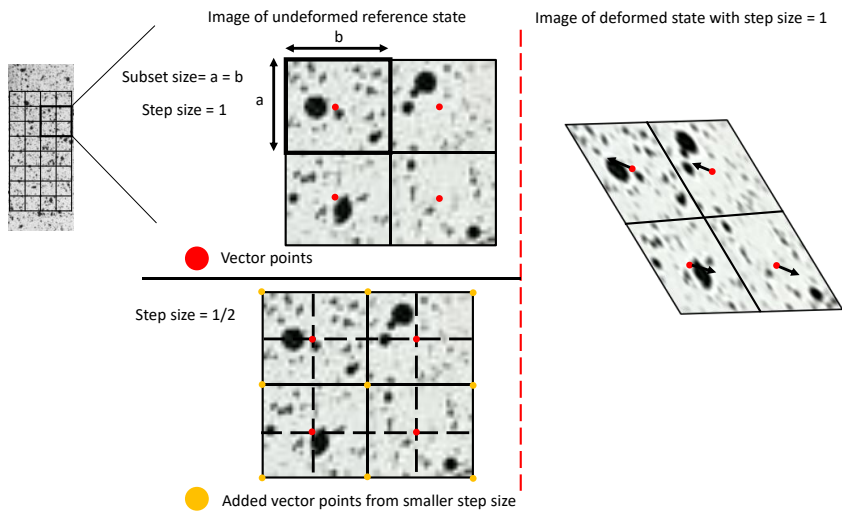
Figure 14 Explanation of the Digital Image Correlation principle.

Post processing DIC

While the strain field data was acquired using Vic-2D, smoothing and further use of the strain data was done using Python scripts developed by the composite group at NTNU.

For the interest of the python competent reader, some details will be provided on how the data was dealt with. As anyone would understand, the files and data were of a big size and the way they were handled greatly influenced runtime of the scripts, which was considerable.

The data was organized in python as nested dictionaries. The dictionaries were organized as follows:

dict[index][load][cycle]=[x,y,exx,eyy,exy]

Index denotes which data point (vector point in Figure 14), load is the load at which the image was taken and cycle at which cycle. x,y is the location in Cartesian coordinates referenced to the undeformed state and is unique for the index. The x,y is referenced to the undeformed state so they do not change. exx, eyy and exy are the in plane strain components. As such, each of the dots/vector points in Figure 14 would be assigned an index, going from 1 to the total amount of datapoints in one image (typically 30 000). The index could have been dropped, but was included as a quality assurance measure.

With such large amounts of data, relatively complex algorithms may be applied, such as those used in the field of computer science. This was however out of scope for the work and the algorithms used were of a simple nature. DIC, python and a lot of data are used. Most conveniently, the large amount of data made it possible to smooth the data without neglecting natural variations in strain and also to interpolate in between voids in the data. Figure 15 shows smoothing on an arbitrarily chosen strain to cycle curve from the data. As seen, the smoothing yields what is arguably a fairly reliable curve, though this can obviously always be discussed. Some parts of the DIC pattern on the samples were difficult for the image recognition software to recognize in every image, making for some occasional blank spots in the data. These were possible to interpolate over, using data from images where the software was able to process the areas, a good example of how the large amount of data was used to estimate missing data with a high degree of certainty. Figure 16 shows the interpolation schematically on a strain to cycle curve with apparent voids. The strain to stress curve ends short of the global failure when there was no data after this point and is thus labelled as a "local failure". The interpolation and the smoothing were the two operations that laid the

foundation for Miner sum calculation and strain curve extraction as presented in the papers. For the research, being able to extract reliable strain curves from any point or region in a fast and convenient way made it possible to get a good and detailed understanding of the damage mechanisms.
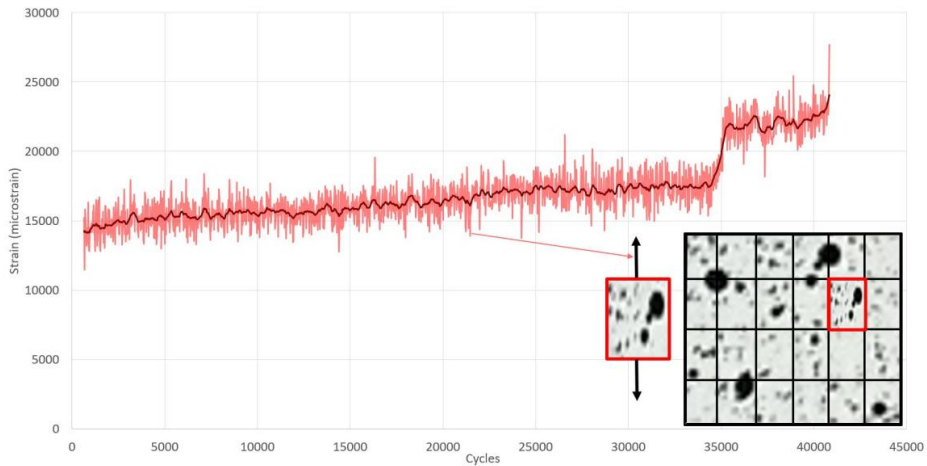

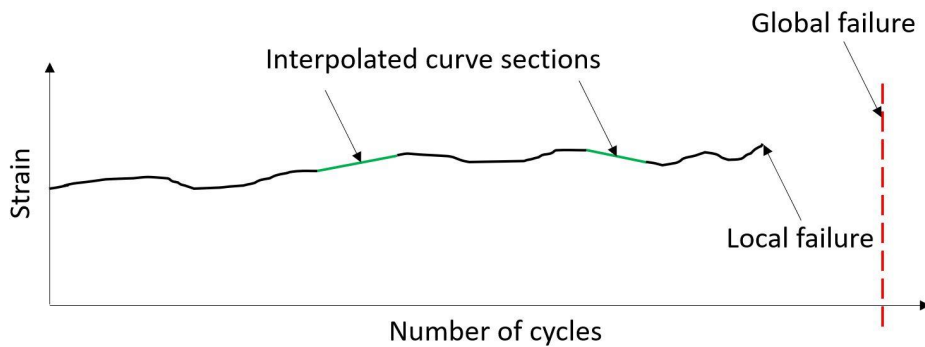*Figure 15 Smoothing on a strain to cycle curve from a DIC datapoint.*

Figure 16 Schematic representation of how missing data points were interpolated over to give a full strain to cycle curve for all data points.

In short, the three following actions were enabled through python scripting:

- Smoothing strain data over the time domain.
- Investigating line slices and areas of interest.
- Miner damage calculation.

A resolution sensitivity study was carried out to confirm that the chosen subset size was sufficiently small to catch the strain at the strain concentrations over the time domain. The resolution was checked for all cycles for all samples. The study was simply done by trying smaller subsets until the strains converged, as for a mesh sensitivity study in a finite element model. Having too small subset sizes gives slow processing and possibly noisy data, therefor it is important to choose a size that is sufficiently small to capture the strain of interest while not being too small to introduce noise.

UMAT and modelling progressive fatigue damage in finite element software

Modelling of damage was done with a Material User Subroutine (UMAT) in Abaqus. UMAT works on the integration points and replace the Abaqus standard constitutive material models. In it's simplest form it takes in the strain increment vector and updates the stress increment vector. It updates the stress increment by defining the Jacobian matrix. This is shown in equation (1) and (2) with the directions being ply-specific as shown in Figure 17. Figure 18 shows the information flow chart of an element and where in the flow the UMAT belongs.

$$
\begin{bmatrix} \Delta\sigma_{11} \\ \Delta\sigma_{22} \\ \Delta\sigma_{33} \\ \Delta\sigma_{12} \\ \Delta\sigma_{13} \\ \Delta\sigma_{23} \end{bmatrix} = \begin{bmatrix} C_{11} & C_{12} & C_{13} & C_{14} & C_{15} & C_{16} \\ C_{21} & C_{22} & C_{23} & C_{24} & C_{25} & C_{26} \\ C_{31} & C_{32} & C_{33} & C_{34} & C_{35} & C_{36} \\ C_{41} & C_{42} & C_{43} & C_{44} & C_{45} & C_{46} \\ C_{51} & C_{52} & C_{\{53} & C_{54} & C_{55} & C_{56} \\ C_{61} & C_{62} & C_{63} & C_{64} & C_{65} & C_{66} \end{bmatrix} * \begin{bmatrix} \Delta\varepsilon_{11} \\ \Delta\varepsilon_{22} \\ \Delta\varepsilon_{33} \\ \Delta\varepsilon_{12} \\ \Delta\varepsilon_{13} \\ \Delta\varepsilon_{23} \end{bmatrix}
\tag{1}
$$

$$C_{nn} \; is \; defined \; by \; the \; user$$

$$
\begin{bmatrix} \sigma_{11} \\ \sigma_{22} \\ \sigma_{33} \\ \sigma_{12} \\ \sigma_{13} \\ \sigma_{23} \end{bmatrix}_{end \; of \; increment} = \begin{bmatrix} \Delta\sigma_{11} \\ \Delta\sigma_{22} \\ \Delta\sigma_{33} \\ \Delta\sigma_{12} \\ \Delta\sigma_{13} \\ \Delta\sigma_{23} \end{bmatrix} + \begin{bmatrix} \sigma_{11} \\ \sigma_{22} \\ \sigma_{33} \\ \sigma_{12} \\ \sigma_{13} \\ \sigma_{23} \end{bmatrix}_{start \; of \; increment}
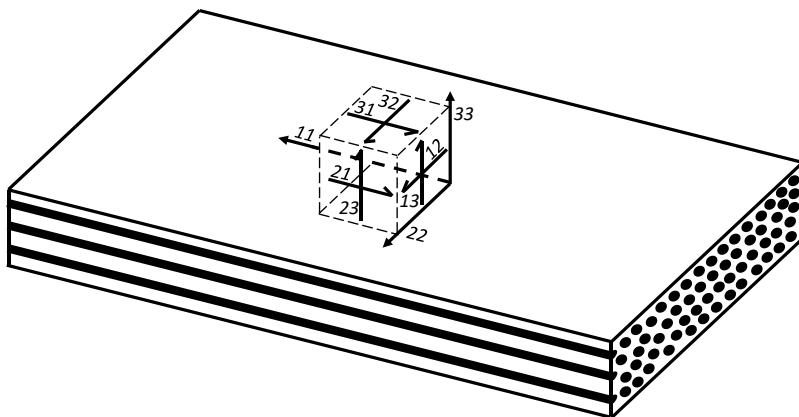\tag{2}
$$

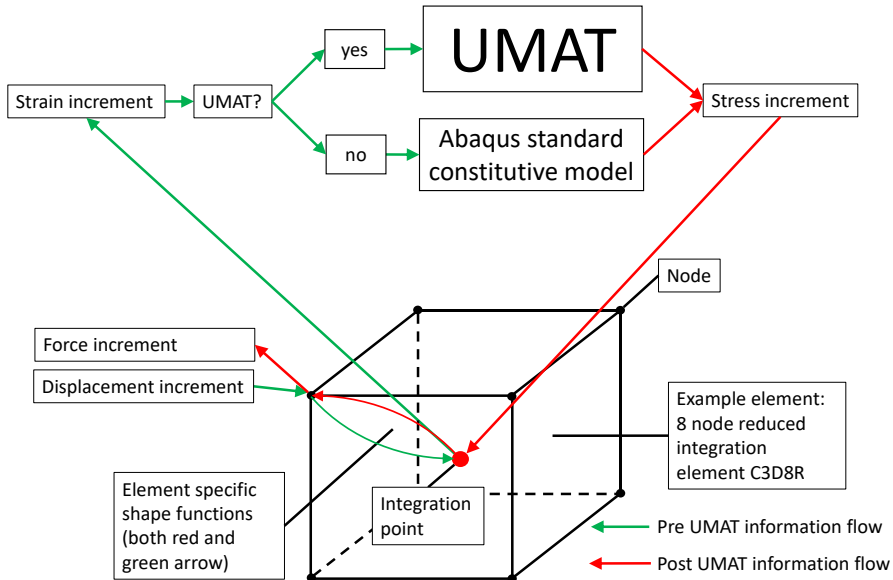*Figure 17 coordinate system of the UMAT.*

Figure 18 Where in the finite element analysis information flow chart the UMAT exists.

UMAT is written in the FORTRAN language (a file may be named Materialmodel.for). The UMAT file is a text file and cannot be executed by itself. For Abaqus to be able to read and use an UMAT file it needs a compiler (Intel Fortran). The Abaqus software needs to be set up to call the compiler upon use of an UMAT file.

Results

Here the key findings from the work will be presented. While the papers in Appendix A, B and C present results on their own, this section aims at showing how the results from all three may be combined to give a more solid foundation for the conclusions. For more detailed results, see the appended papers.

Paper I - Strain field redistribution and matrix damage

In Paper I, basic failure mechanisms of composite fatigue was investigated. A high cycle fatigue split disk test was run and monitored with DIC. In Paper I it was concluded that damage spreading in the matrix material redistributes strain fields. Matrix damage occurred long before initiation of fiber failure and was found to be steadily ongoing throughout the whole fatigue life. Further it was concluded that damage in the matrix material eased travel of progressive fiber failure and that fiber failure preferred to evolve in areas with matrix damage, even if there were areas with higher strain in the fiber direction elsewhere in the structure, but with less extensive matrix damage. The conclusion was drawn based on the graph in Figure 19 with results from the highlighted regions in the DIC strain plot in Figure 20. The graph shows how the peak strain location moved throughout the test inside the four regions while the SCF lowered until catastrophic failure. The only way for the location to move and SCF to lower is by matrix damage, as schematically explained in Figure 21 with how loss of shear transfer may reduce strain concentrations. As seen in Figure 19, the peak strain was 5000 micro strain higher throughout the test in the orange rectangle, it however had less strain redistribution (less matrix damage) and therefor did not fail before the black rectangle, which had extensive strain redistribution/matrix damage.
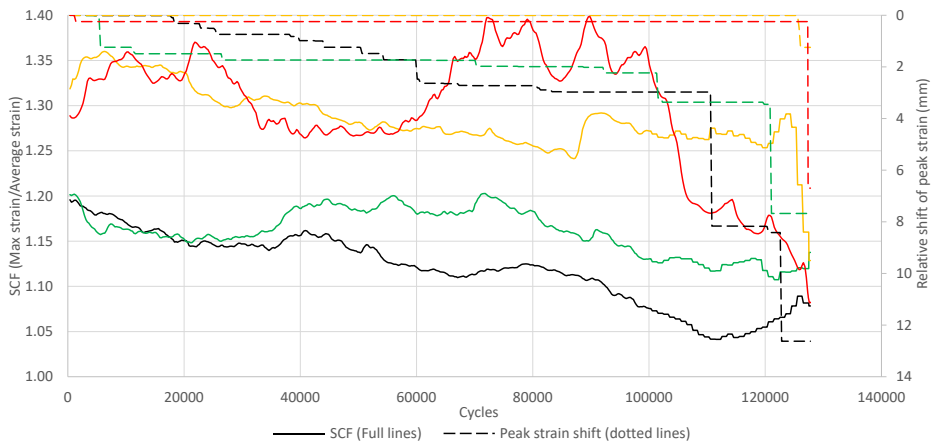
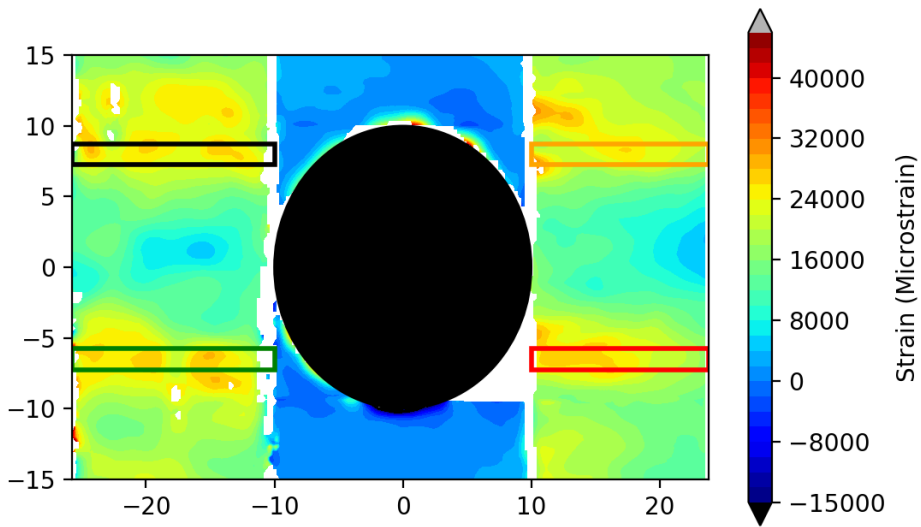*Figure 19 SCF and peak strain shift from the areas/regions in Figure 20.*

Figure 20 Contour plot of strain near end of life for the split disk fatigue test. Early fiber failure can be seen above the black rectangle. The black rectangle developed fiber damage first of all the four outlined regions.
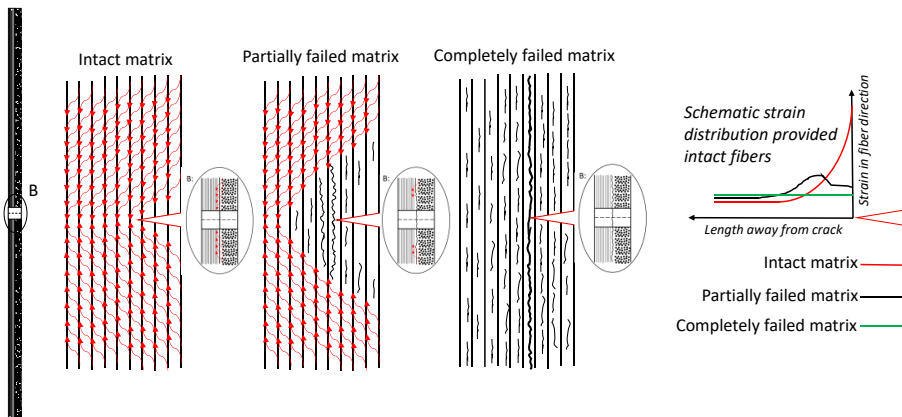

Figure 21 Schematic outlining how matrix damage affects the strain in the fiber direction as the matrix damage spreads through the material.

23

Paper II - Local fiber S-N curve

In paper II an S-N curve for the fiber direction was found through damage calculation on DIC data. There were two main novel methods in this paper: damage calculation on DIC data and definition of local S-N curves.

The damage calculation on DIC data was initially suggested as a method to avoid matching of strain from FE analysis with DIC strain data by changing parameters in the FEA failure criteria to achieve better correlation. The initial idea being to test how coupon test S-N curves predict damage on actual strain to cycle curves as in a FEA model using a Miner damage accumulation rule. It was however found that the coupon test curves predicted very conservative damage predictions, near useless for FEA implementation. A novel method was suggested to find S-N curves for the fiber direction that applied locally and could be used as input in a FEA model for prediction of fiber failure. The method was inspired by, amongst others, He et. al. [61]. He used an iterative algorithm that changed the parameters of a static finite element model of a composite SBS test to match DIC data from a static SBS test. A static FEA model is relatively exactly defined and He's approach is therefor relatively straight forward. A FEA model of a fatigue experiment is less so, as outlined in Paper III that is concerned with modelling. He's approach is there for not possible to copy for a fatigue load case. However, calculating the Miner damage on the peak strain per cycle from the DIC data from the experiment is similar to the way damage is calculated in the numerical model. The two damage calculations should therefor match given that the numerical model is reasonably well defined in geometry and constitutive behavior.

DIC data differ from traditional cycle to strain curves from common fatigue testing in three ways that makes finding local S-N curves different from normal coupon testing:

- There are many more strain to cycle curves in a typical DIC dataset than in an experimental test program of 10 to 100 specimens.
- The DIC curves are not constant.
- The DIC curves have no defined failure cycle.

The first is an obvious strength. The two other represent challenges that need novel methods to overcome. The ideal case would be 30 000 cycle to strain curves with constant strain and defined failure cycles. This would be equivalent to gradual fiber failure occurring over constant strain in the monitored experiment and the possibility to record this failure. This argument would be practically valid had there been gradual fiber failure in the structure and constant strain. Both of these arguments are false, as proven in Paper I. Gradual damage occurs in the matrix and fiber failure occurs only over a short cycle span towards end of life in the investigated specimen. The redistribution of the strain fields combined with loss of stiffness from less stiffness contribution from the matrix gives large changes in the stress and strain distribution throughout the experiment. The Miner damage accumulation rule may be used to overcome variable strain curves. The aim then being failure at a Miner number of 1.0. The issue of a non-defined failure cycle may be overcome by looking at failing areas/regions instead of failure cycles, as all the strain curves last until the global failure cycle. Some areas develop fiber failure while other areas don't. In the areas that do not develop fiber failure, the Miner damage rule should have a value below 1.0 throughout the whole fatigue life. In the areas that do develop fiber failure the Miner damage rule should have a value above 1.0. While the Miner damage accumulation rule has a very defined value for failure; 1.0, it is still subject to the same variation in fatigue properties as an S-N curve, which can be a decade or more for GFRP. A decade scatter is the difference in Miner sum between 0.1 and 1.0 or 1.0 and 10.0. This makes studying failing and non-failing areas more convenient than bothering with the exact value of the Miner sum. In the following a summary of Paper II is given highlighting how the issues discussed above were dealt with in practical terms.

In Paper II, three specimens were fatigue tested at constant load. The specimens failed at 40 820, 65360 and 127 768 cycles and are called A to C respectively. All three specimens had very defined regions that contained failure, three to four in each specimen outlined in Figure

22. The red areas developed fiber failure first and green failed shortly after the red. The remaining part of the specimen showed little fiber damage. It was concluded that any S-N curve should predict damage in the red areas.

To evaluate the S-N curves, exposure factor was used instead of Miner sum. Exposure factor is defined in equation (3) and (4). It is the strain divided by the residual strain in the point of interest. Residual strain is given by the Miner rule following Hashin's residual strain calculation [25].

The found S-N curve predicted damage (exposure factor above 1.0) at close to catastrophic failure as shown in Figure 23 for the three specimen. To evaluate different S-N curves over the time dimension, the width of the failing regions with exposure factor above 1.0 was used as measure. This is outlined in Figure 24 for Specimen C with the damaged width of three S-N curves in Figure 25. The A curve has the origin strain in the log-log S-N curve at 22150, which was the static failure strain found when lab testing at NTNU's lab. Curve B has got the origo strain at 33 000 microstrain, reported as the static max strain by the fiber producer. S-N curve D has got the origo strain at 57500 microstrain, which gave a correct damaged width at the failure cycle. The S-N curves are displayed in Figure 26. Seeing as curve D had the correct damaged width at the failure cycle it was concluded to be the correct curve to use for input in the Finite Element Analysis. It is considerably higher than the other S-N curves, this is due to the local nature of the measuring, using DIC. Locally, strains can be much higher than the mean used in normal tab test, either from the test machine displacement or from traditional strain gauges, explaining the difference. See Paper II for further details.
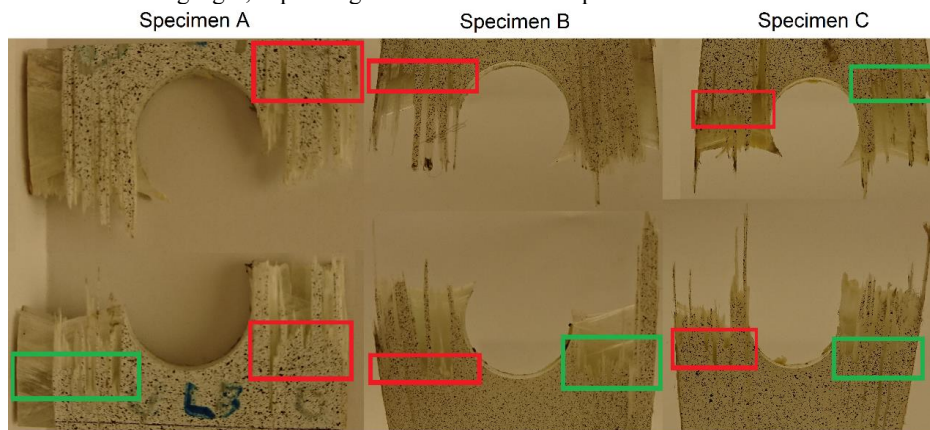

Figure 22 Areas containing failure of the specimens in paper II, red indicates the sections containing first fiber failure.
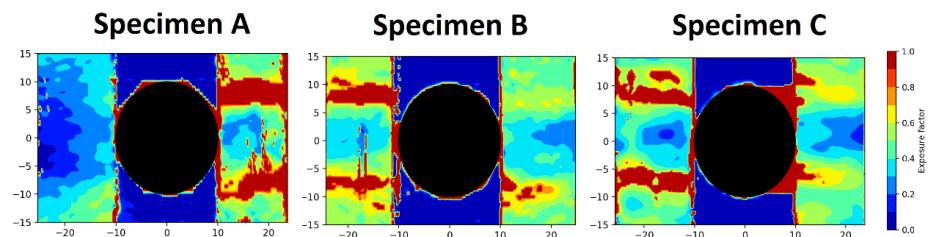

Figure 23 Exposure factor over specimen A-C at close to catastrophic failure for the local S-N curve.
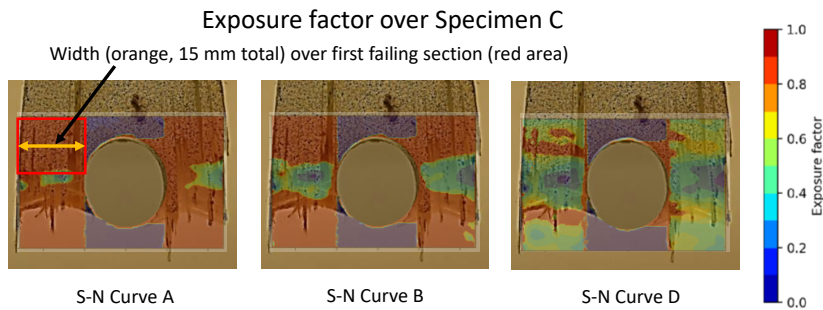
Exposure factor over Specimen C

Width (orange, 15 mm total) over first failing section (red area)

S-N Curve A   S-N Curve B   S-N Curve D

Figure 24 Exposure factor projected over failure of the C specimen.

Width with exposure factor > 1 in the first failing section for selected S-N curves for Specimen C
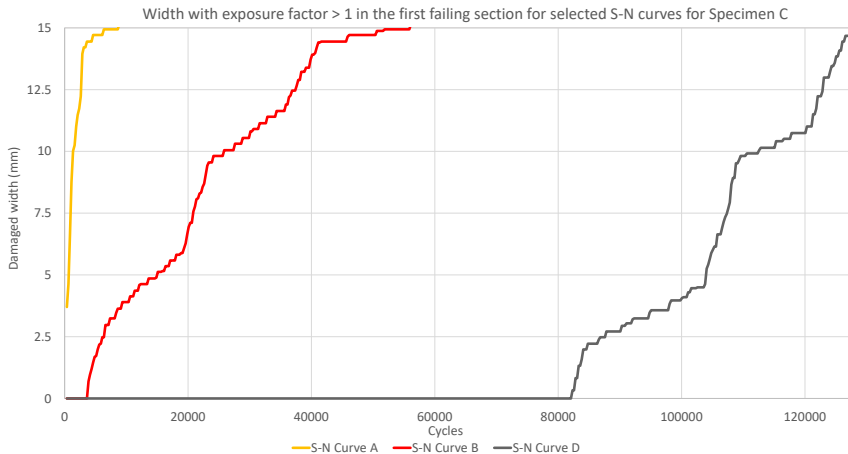
S-N Curve A   S-N Curve B   S-N Curve D

Figure 25 Damaged width of the first failing cross section in Specimen C for various S-N curves. The A and B are using nominal reported coupon test properties from the NTNU lab and the fiber producer, while the black curve is the curve that was found that most correctly predict damage in the DIC images.
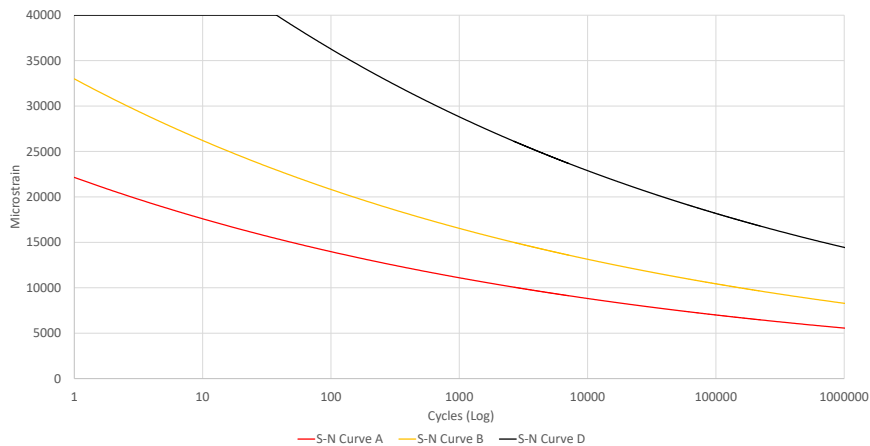

S-N Curve A   S-N Curve B   S-N Curve D

Figure 26 S-N curves for damage calculation.

Paper III - Novel method of modelling progressive fatigue damage

Paper III outlines a novel method for modelling progressive fatigue damage in composites. While almost all past work attempts to match the global constitutive behavior in model and experiment, the presented model both takes in the global and local behavior. The model was compared with Specimen C having a failure cycle of 127 814 cycles. In the past two papers, a failure cycle of 127 768 was reported for Specimen C, however, this was when the last DIC

image was taken and mistakenly taken for the failure cycle. The discrepancy was due to a data bug and the actual failure cycle was found to be 127 814 on a later stage. The failure cycle is however arbitrary to the goal of the work, which is the process leading up to catastrophic failure. This data bug has there for not been put any emphasis on in the papers. However, it comes to light when doing a review of all three papers and in the spirit of research honesty it is therefor commented here.

Fatigue damage was modelled using cohesive surfaces for macro matrix cracking and an UMAT user material subroutine for micro damage. Only selected cycles were simulated using a simplified cycle jump approach. The cohesive surface formulation was not subject to any fatigue degradation rules during the analysis, but had the fracture energy and contact strength globally reduced to take into account fatigue damage. The UMAT reduced the failure strain in the respective directions based on max strain failure criteria and log-log S-N curves. While the matrix properties were taken from standard coupon testing, the fiber S-N curve was as described in Paper II. Though the respective directions were treated individually, reduction of matrix associated properties (all directions apart from the fiber direction) followed peak exposure factor in the matrix associated directions. Fiber failure only followed the exposure factor in the direction of the fiber. Table 2 shows how the stiffness was degraded using stiffness degradation factors S_{ij} after failure for the individual directions based on the value of the exposure factor f_{ij} as defined in equation (3) – (6) M is the Miner sum and α the slope of the log-log S-N curves.

Table 2 How reduction factors are changed depending on failure criterion.

	S_{11}	S_{22}	S_{33}	S_{12}	S_{13}	S_{23}
Fiber failure ($f_{11} > 1.0$)	0.1	0.1	0.1	0.1	0.1	0.1
Matrix failure ($f_{22}, f_{33}, f_{12}, f_{13}$ or $f_{23} > 1.0$)	0.9	0.1	0.1	0.1	0.1	0.1

$$
\begin{bmatrix} f_{11} \\ f_{22} \\ f_{33} \\ f_{12} \\ f_{13} \\ f_{23} \end{bmatrix} = \begin{bmatrix} \frac{1}{\varepsilon_{res,11}} & 0 & 0 & & & \\ \frac{v_{12}}{\varepsilon_{res,22}} & \frac{1}{\varepsilon_{res,22}} & 0 & 0 & 0 & 0 \\ \frac{v_{13}}{\varepsilon_{res,33}} & 0 & \frac{1}{\varepsilon_{res,33}} & 0 & 0 & 0 \\ 0 & 0 & 0 & \frac{1}{\varepsilon_{res,12}} & 0 & 0 \\ 0 & 0 & 0 & 0 & \frac{1}{\varepsilon_{res,13}} & 0 \\ 0 & 0 & 0 & 0 & 0 & \frac{1}{\varepsilon_{res,23}} \end{bmatrix} * \begin{bmatrix} \varepsilon_{11} \\ \varepsilon_{22} \\ \varepsilon_{33} \\ \varepsilon_{12} \\ \varepsilon_{13} \\ \varepsilon_{23} \end{bmatrix} \tag{3}
$$

$$
\varepsilon^N_{res,ij} = \hat{\varepsilon}^N_{ij}[1 - M^N]^\alpha \tag{4}
$$

$$
\begin{bmatrix} E_{11} \\ E_{22} \\ E_{33} \\ G_{12} \\ G_{13} \\ G_{23} \end{bmatrix} = \begin{bmatrix} S_{11} & 0 & 0 & 0. & 0 & 0 \\ 0 & S_{22} & 0 & 0 & 0 & 0 \\ 0 & 0 & S_{33} & 0 & 0 & 0 \\ 0 & 0 & 0 & S_{12} & 0 & 0 \\ 0 & 0 & 0 & 0 & S_{13} & 0 \\ 0 & 0 & 0 & 0 & 0 & S_{23} \end{bmatrix} * \begin{bmatrix} E_{11} \\ E_{22} \\ E_{33} \\ G_{12} \\ G_{13} \\ G_{23} \end{bmatrix} \tag{5}
$$

27

$$\begin{bmatrix} v_{12} \\ v_{13} \\ v_{23} \end{bmatrix} = \begin{bmatrix} S_{12} & 0 & 0 \\ 0 & S_{13} & 0 \\ 0 & 0 & S_{23} \end{bmatrix} * \begin{bmatrix} v_{12} \\ v_{13} \\ v_{23} \end{bmatrix} \qquad (6)$$

Due to variations in matrix properties as outlined in Paper I, the FEA model of the split disk was run with five material cases called A-E. A had original material properties and D had very reduced properties in the matrix direction, with the origin of the matrix S-N curves reduced down to 40% of the original value. E was run without degradation in the fiber direction, as this was found to greatly increase runtime while also not being representative of the experimental fiber failure. Table 3 and Table 4 summarize the reduction factors, see Paper III for more extensive explanation of the factors and modelling method. Figure 27 shows the model, it's 1/8 to reduce analysis time.

Table 3 Material cases for model A – D.

	Factor applied to nominal static values and S-N curve origin ($\hat{\varepsilon}^O_{22T}, \hat{\varepsilon}^O_{33T}, \hat{\varepsilon}^O_{22C}, \hat{\varepsilon}^O_{33C}, \hat{\varepsilon}^O_{12}, \hat{\varepsilon}^O_{13}, \hat{\varepsilon}^O_{23}$)	Factor applied to contact strength (t_n, t_s, t_t)	Factor applied to fracture energy (G_n, G_s, G_t)	Stiffness degradation factor of fiber upon matrix failure, S_{11}, see Table 4.
Model A	1.0	$\hat{\sigma}_{22T} * 0.6$	0.6	0.9
Model B	0.6	$\hat{\sigma}_{22T} * 0.6$	0.6	0.9
Model C	0.6	$\hat{\sigma}_{22T} * 0.36$	0.36	0.6
Model D	0.4	$\hat{\sigma}_{22T} * 0.36$	0.36	0.6
Model E	0.6	$\hat{\sigma}_{22T} * 0.6$	0.6	0.7

Table 4 Stiffness reduction factors for Model C, D and E.

	S_{11}	S_{22}	S_{33}	S_{12}	S_{13}	S_{23}
Fiber failure ($f_{11} > 1.0$)	0.1 (A-D)/1.0 (E)	0.1	0.1	0.1	0.1	0.1
Matrix failure ($f_{22,33,12,13,23} > 1.0$)	0.6 (C and D)/0.7 (E)	0.1	0.1	0.1	0.1	0.1

Figure 27 FEA Model mesh and geometry.

Strain field comparison of the FEA model and the experiment is shown in Figure 28 from cycle 80 000. The matrix damage model D curve approaches the strain curve from the black rectangle (green curve), while Model A with original properties approach the curve from the red rectangle with little matrix damage (orange curve). It can be seen that the reduced matrix property model (Model D) clearly gives an uneven and higher strain curve than the original matrix property model (Model A). After 80 000 cycles, the models were not able to capture the strain fields as the bottom hoop layer failed, see Paper III for further details.
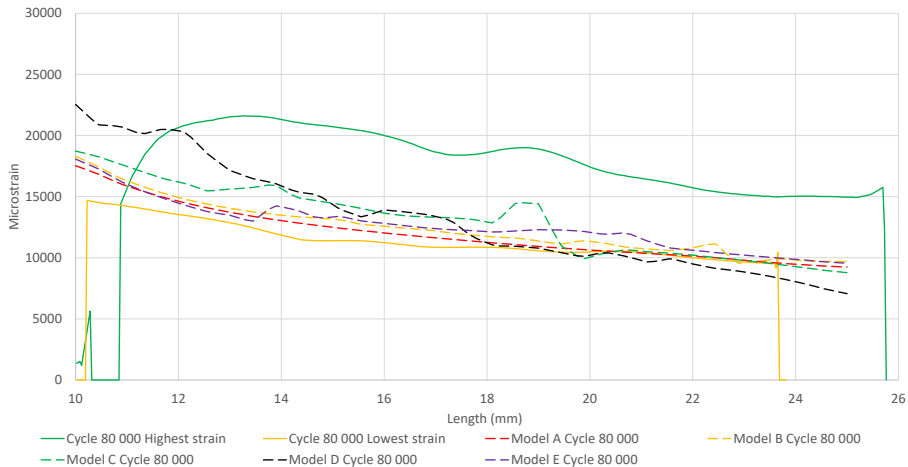

Figure 28 FEA models and strain curves over the most and least strained cross sections in Figure 20, the black and red rectangles.

The global behavior expressed through cross head displacement is shown in Figure 29. The displacement curve does show how the five models all match the displacement from the experiment apart from model D, which shows a markedly more compliant behavior.

Figure 29 Cross head displacement in model and experiment compared.
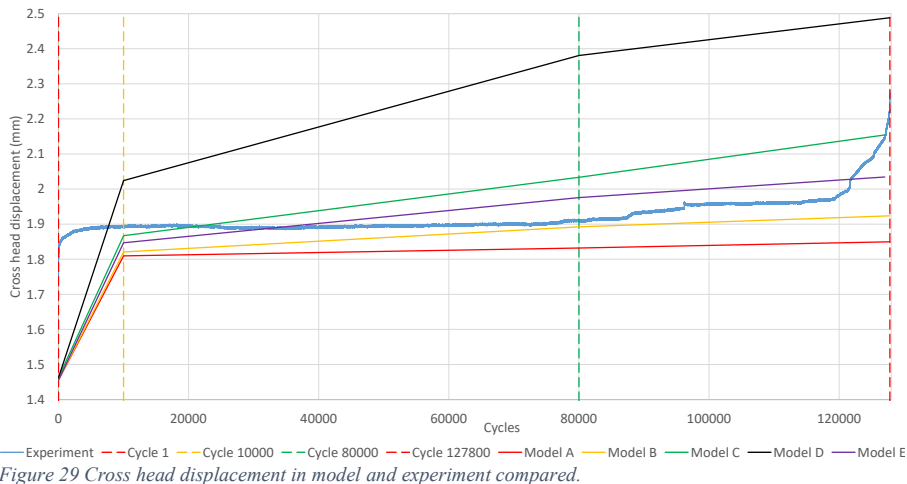
It was concluded that Model E, with the fiber degradation removed, was the most fit for use model. It had low runtime while managing to highlight what regions would later develop matrix damage. From Paper I it was proven that the regions with the most extensive matrix damage would later develop fiber damage, and as such model E could there for be used by design engineers to find regions susceptible to this. Evidently, if there is low loads in the fiber direction and high loads in the matrix direction, this argument will be false. However, for pressure vessels, the fibers are oriented to carry the main bulk of the load and as such Model E would be useful. While not simulating fiber failure directly, Model E could still plot where the exposure factor in the fiber direction exceeded 1.0 and this first happened a decade before catastrophic experimental failure, same as for the other models. Using first integration point with exposure factor above 1.0 as design criteria would yield a sufficient safety factor towards catastrophic failure and would anyway make simulation of the actual catastrophic failure superfluous, further supporting use of Model E.

Conclusions

The work has produced novel methods and results documented in three papers.

The first paper proved how fatigue damage in filament wound materials is largely driven by damage progression in the matrix. It was found that matrix damage eases progressive fiber failure and is the key parameter for predicting likely point of fiber failure in high strain areas. A monitoring method for composite components with particular appliance to pressure vessels was suggested and proven on an experimental specimen, tracing the strain concentration factor and strain field change expressed as shift of strain concentration over time. As matrix damage changes the strain distribution, tracing the strain shift and SCF over time indicates if matrix damage is evolving or not.

The second paper made further use of the DIC results used in Paper I and suggested a novel method for finding S-N curves based on DIC strain data. The method is based on tracing the Miner damage over regions containing fiber failure. An S-N curve was capable of predicting failing regions in three specimens. The S-N curve was considerably higher than what would be expected from conventional tab testing, an attribute of the local scope of the investigation.

To further investigate the S-N curve in Paper II and the damage mechanisms found in Paper I, a finite element analysis was made of the split disk experimental setup and a fatigue degradation method was developed. Paper III describes the model and the results. While the model itself was as equal in geometry as possible to the split disk and used conventional methods for modelling, the degradation method was novel. The degradation method consisted of a micro damage modelling method using a user material subroutine (UMAT) and a macro damage method using conventional cohesive surfaces in Abaqus. The UMAT used the max

strain failure criterion, log-log S-N curves and the Miner fatigue damage accumulation rule to account for fatigue damage. To handle the brittle nature of matrix and fiber failure, a cycle jump approach was used. Variations in matrix properties in the experimental data were handled by running five models with matrix properties ranging from full down to 40% of the original properties. The models matched the strain fields from Paper I with different matrix damage. The good match proved how variations in matrix properties and spreading of matrix damage was the key reason for the strain field redistribution observed in Paper I. Interestingly, fluctuations in the strain fields observed in the first failing regions in the experiment was also present in the FEA model with the poorest matrix properties. The finding further supports that matrix and fiber failure are strongly linked. The S-N curve from Paper II managed to predict fiber failure within a decade of the observed experimental failure using the developed modelling approach and the principle of first fiber failure. The model fell short of correctly modelling catastrophic fiber failure due to the sudden nature of this process. However, being able to model the onset of fiber and matrix damage fairly accurately is already an improvement and probably sufficient for most practical applications.

Suggestions for future work

Numerical and Experimental work

While the tested ring specimen in this work had a fairly complex strain distribution, they had a very defined point of failure, the advantage of using the split disk setup. Ideally, an experimental setup would be developed with the point of failure predictability of the split disk without the complex strain fields arising from through thickness strain fields at the splits. In this way, more specific failure mechanisms could be monitored. Flat coupon specimens are perhaps the most obvious alternative, however, they traditionally fail at the grips when testing with composites and they perform poorly with curved specimen from filament winding.

Regardless of the test method, the most important prospect lies in the way data are handled from the experiments. The more information that can be acquired, the less assumptions have to be made. While recording peak strain throughout cycling may estimate the S-N curve locally and give information on progressive failure, it still gives little information about the evolution of the constitutive properties. If in addition to recording the peak strains, also the strain at intermittent loads were recorded, the stiffness of each point may be correlated to the damage state in the point. The concept is outlined in Figure 30. This will give extensive datasets, but while the peak strain frames may be shot with the same frequency as in this work, the intermittent frames may be done less often, giving a small increase in data with a potentially big gain. If combined with the numerical matching method of He et. al. [61], it is possible to get very exact answers to constitutive behavior and it's degradation over time. The work will be very much of a data handling format, but this is also the nature of modern science. Within the somewhat chaotic field of composite fatigue it has big potential.
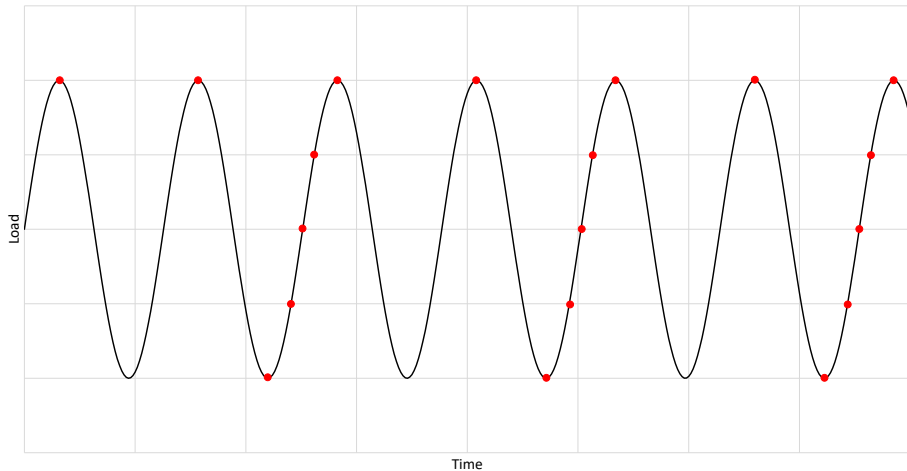
Figure 30 A load vs time curve with red dots indicating when the DIC cameras should fire in a method that may give more information on the damage state's effect on the constitutive behavior.

The perhaps biggest challenge model wise is how to handle the brittle nature of progressive failure in composites. This is hugely challenging and in essence an impossibility using conventional iterative schemes without predefined crack lines. The ideal model would evidently load up once and iterate on time and damage. Progressively reducing stiffness in integration points as damage progressed, not needing the cycle jump approach. The cycle jump approach, despite it's weaknesses, does have some advantages, particularly if combined with data from DIC monitoring as outlined in Figure 30. In essence, the cycle jump approach follows a load vs time curve more or less as in Figure 30. By comparing not only the peak strains per frame, but also the strain in the loading phase, even more accurate comparisons of model and experiments can be made than in Paper III. If combined with numerical methods such as that proposed by He et. al., iterative matching between model and experiment can be done at different cycles.

The goal of numerical and experimental matching and comparison is to reduce the amount of assumptions in between experiment and model. The most basic experimental observation is limited by the human capacity as a monitoring tool, visual inspection and perhaps hearing. By making a model that is equal in geometry and has failure occurring at the same place as the experiment, the human capacity is used to close to it's full potential. The perhaps next step is having a displacement to load or time curve from the test machine that may also be matched. This is so far most experimental and model matching goes in research. By using assumptions on the cross section and stress/strain distribution, a stress/strain or S-N curve may be acquired from the displacement and load data. Using DIC, the point by point surface strain may be acquired and matched with the model leaving fewer assumptions. This is evidently an advantage, but for materials with many imperfections it may also reveal a very chaotic reality that is challenging to apply exact definitions to, necessary for modelling. This is evident in the DIC data from the split disk testing and modelling.

Finding methods to handle the chaotic nature of composites is difficult and to better match model and experiment is the aspect that may yield the biggest challenge. A FEA model demands discretely defined areas of material properties with clear borders in between. An actual component have a chaotic distribution of imperfections and the borders between stiff/soft and strong/weak material may be randomly drawn. However, given material failure in one key area or point, the progression may be dependent on the material properties in the neighboring material and a global reduction of properties may be used instead of discretely defined regions. This is in essence the approach used in Paper III, handling the strain curves' variation by a parameter study. With better matching of model and experiment, the size of the parameter variation may be more exactly defined and also, perhaps equally interesting, the distribution and extent of weak material in a structure may be more exactly defined.

32

Monitoring - NDE

While the experimental and modelling work demands extensive resources and time to improve, Non Destructive Evaluation, NDE, or monitoring of damage in composites with particular focus for pressure vessels may demand less resources to develop. This is largely due to the recent advent of data handling tools such as Python which has enabled the normal engineer to handle data in a way that was left to data scientists before. The DIC data evaluation method outlined in Paper I and II may serve as a basis for further work. Monitoring could be either done over an area with wear or at known weak spots in vessels. A speckle pattern painted over such an area and images taken evenly throughout the use of the vessel may give information on the stability of the strain fields. A graph such as in Figure 19 with measures that was proven to single out the most critical regions outlined in Figure 20 in Paper I may be produced for a monitored vessel. In the advent of a steadily falling SCF and movement of the strain concentration, the monitored area clearly would contain spreading of damage and this would be a warning sign to the integrity. The advantage of the method is that the pressure of the vessel upon monitoring would be arbitrary and a sequence of DIC frames over some time enough to judge the damage state of the area of interest.

Provided images from peak pressure, a Miner sum could be calculated as in Paper II and a plot of theoretical damage produced and updated with each new DIC frame. Figure 31 has got the strain shift from Figure 19 over the black rectangle in Figure 20 plotted along the damaged length from the same area in Paper II. As seen, the two correlate and both may serve as a valuable tool for integrity monitoring. The fact that the two correlate gives the theoretically calculated damage some physical evidence and the two in combination gives a very good view of the severity of damage in the area of interest.
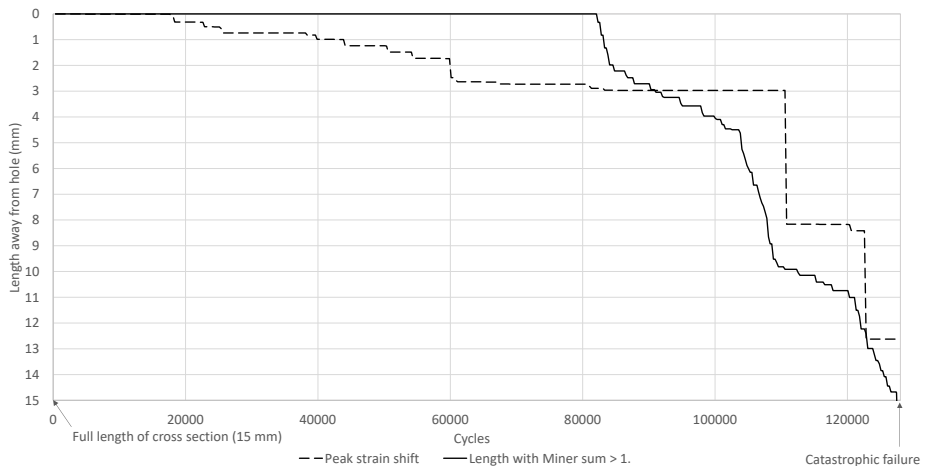

Figure 31 Damaged length from Paper II and peak strain shift from Paper I plotted in the same figure.

References

[1] N. T. Stetson, S. McWhorter and C. C. Ahn, "Introduction to hydrogen storage," in *Compendium of Hydrogen Energy Volume 2: Hydrogen Storage, Distribution and Infrastructure*, Kidlington, Woodhead Publishing, 2016, pp. 3-25.

[2] A. T. Echtermeyer and K. Lasn, "Safety approach for composite pressure vessels for transport of hydrogen. Part 2: Safety factors and test requirements," *International journal of hydrogen energy,* vol. 39, no. 26, pp. 14142-14152, 2014.

[3] S. W. Jorgensen, "Hydrogen storage tanks for vehicles: Recent progress and current status," *Current Opinion in Solid State and Materials Science,* vol. 15, pp. 39-43, 2011.

[4] ISO, ISO 11119-3:2020 Gas cylinders - refillable composite gas cylinders and tubes. Part 3: fully wrapped fibre reinforced composite gas cylinders and tubes up to 450 L with non-load-sharing metallic or non-metallic liners., Geneva: ISO - International Organization for Standardization, 2020.

[5] ISO, ISO 11515:2013(E). Gas cylinders - refillable composite reinforced tubes of water capacity between 450 L and 3000 L - design, construction and testing., Geneva: ISO - International Organization for Standardization, 2019.

[6] ISO, ISO 11439:2013 Gas cylinders — High pressure cylinders for the on-board storage of natural gas as a fuel for automotive vehicles, Geneva: ISO - International Organization for Standardization, 2019.

[7] ISO, ISO 19881:2018 Gaseous hydrogen — Land vehicle fuel containers, Geneva: ISO - International Organization for Standardization, 2018.

[8] S. Satyapal, J. Petrovic, C. Read, G. Thomas and G. Ordaz, "The U.S. Department of Energy's National Hydrogen Storage Project: Progress towards meeting hydrogen-powered vehicle requirements," *Catalysis Today,* vol. 120, no. 3-4, pp. 246-256, 2007.

[9] US Departement of Energy, "Hydrogen, fuel cells and infrastructure technologies program. Multi-Year Research," in *Development and Demonstration Plan*, Washington, US Department of Energy, 2005.

[10] M. Bertin, D. Halm, B. Magneville, J. Renard, P. Saffré and S. Villalonga, "Oneyear OSIRHYS IV project synthesis: mechanical behaviour of 700 bar type iv high pressurevessel code qualification," in *15th European conference on composite materials*, Venise, 2012.

[11] R. Talreja and W. Watt, "Fatigue of composite materials: damage mechanisms and fatigue-life diagrams," *Proceedings of the Royal Society,* vol. 378, no. 1775, 1981.

[12] S. Ochiai, K. Schulte and P. . W. M. Peters, "Strain concentration factors for fibers and matrix in unidirectional composites," *Composites Science and Technology,* vol. 41, no. 3, pp. 237-256, 1991.

[13] L. C. Pardini and L. G. Borzani Manhani, "Influence of the Testing Gage Length on the Strength, Young's Modulus and Weibull Modulus of Carbon Fibres and Glass Fibres," *Materials Research,* vol. 5, no. 4, pp. 411-420, 2002.

[14] J. F. Mandell, F. J. Mcgarry, A. J. Hsieh and C. G. Li, "Tensile Fatigue of Glass Fibers and Composites with Conventional and Surface Compressed Fibers," *Polymer Composites,* vol. 6, no. 3, pp. 168-174, 1985.

[15] A. T. Seyhan, "A Statistical Study of Fatigue Life Prediction of Fibre Reinforced Polymer Composites," *Polymers & Polymer Composites,* vol. 19, no. 9, pp. 717-724, 2011.

[16] A. Plumtrée and L. Shi, "Fatigue damage evolution in off-axis unidirectional CFRP," *International Journal of Fatigue,* vol. 24, no. 2-4, pp. 155-159, 2002.

[17] R. J. Young, "Composite micromechanics: From carbon fibres to graphene, Editor(s): P.W.R. Beaumont, C. Soutis, A. Hodzic," in *Woodhead Publishing Series in Composites Science and Engineering,*, Kidlington, Woodhead Publishing, 2015, pp. 3-23.

[18] DNV GL, DNVGL-RP-C203 Fatigue design of offshore steel structures, Høvik: DNV GL, 2019.

[19] Dassault Systèmes, "2.2.1 Nonlinear solution methods in ABAQUS/Standard," in *Abaqus Theory Guide*, Dassault Systèmes, 2016.

[20] J. Degrieck and W. V. Paepegem, "Fatigue Damage Modelling of Fibre-reinforced Composite Materials: Review," *Applied Mechanics Reviews,* vol. 54, no. 4, pp. 279-300, 2001.

[21] L. J. Broutman and S. A. Sahu, "New theory to predict cumulative fatigue damage," in *Composite Materials: Testing and Design (Second Conference), ed. H. Corten*, vol. 497, West Conshohocken, ASTM International, 1972, pp. 170-188.

[22] Z. Hashin and A. Rotem, "A cumulative damage theory of fatigue failure," *Journal of Material Science,* vol. 34, no. 2, pp. 147-160, 1978.

[23] J. A. Epaarachchi and P. D. Clausen, "A new cumulative damage model for glass fibre reinforced plastic composites under step/discrete loading," *Composites Part A: Applied Science and Manufacturing,* vol. 36, no. 9, pp. 1236-1245, 2005.

[24] J. F. Mandell and D. D. Samborsky, DOE/MSU Composite Material Fatigue Database: Test Methods, Materials and Analysis, Montana: Montana State University, 1998.

[25] Z. Hashin, "Cumulative damage theory for composite materials: Residual life and residual strength methods," *Composite Science and Technology,* vol. 23, no. 1, pp. 1-19, 1985.

[26] T. P. Philippidis and V. A. Passipoularidis, "Residual strength after fatigue in composites: Theory vs. experiment," *International Journal of Fatigue,* vol. 29, no. 12, pp. 2104-2116, 2007.

[27] S. Sarkani, G. Michaelov, D. P. Kihl and J. E. Beach, "Stochastic Fatigue Damage Accumulation of FRP Laminates and Joints," *Journal of Structural Engineering,* vol. 125, no. 12, 1999.

[28] M. Nikforooz, J. Montesano, M. Golzar and M. M. Shokrieh, "Fatigue behavior of laminated glass fiber reinforced polyamide," *Procedia Engineering,* vol. 213, pp. 816-823, 2018.

[29] W. V. Paepegem and J. Degrieck, "Effects of Load Sequence and Block Loading on the Fatigue Response of Fiber-Reinforced Composites," *Mechanics of Advanced Materials and Structures,* vol. 9, no. 1, pp. 19-35, 2002.

[30] V. M. Harik, J. R. Klinger and T. A. Bogetti, "Low-Cycle fatigue of unidirectional composites: Bi-linear S-N curves," *International journal of Fatigue,* vol. 24, no. 2, pp. 455-462, 2002.

[31] S. Blassiau, A. R. Bunsell and A. Thionnet, "Damage accumulation processes and life prediction in unidirectional composites," *Proceedings of the royal society,* vol. 463, no. 2080, pp. 1135-1152, 2007.

[32] J. Weng, W. Wen and H. Zhang, "Multiaxial fatigue life prediction of composite materials," *Chineese Journal of Aeronautics,* vol. 30, no. 3, pp. 1012-1020, 2017.

[33] M. M. Shokrieh and L. B. Lessard, "Progressive Fatigue Damage Modelling of Composite Materials, Part I: Modelling," *Journal of Composite Materials,* vol. 34, no. 13, 2000.

[34] M. M. Shokrieh and L. B. Lessard, "Progressive Fatigue Damage Modelling of Composite Materials, Part II: Material Characterization and Model Verification," *Journal of Composite Materials,* vol. 34, no. 13, 2000.

[35] T. Adam, R. F. Dickson, C. J. Jones, H. Reiter and B. Harris, "A Power Law Fatigue Damage Model for Fiber-Reinforced Plastic Laminates," *Proceedings of the Institution of Mechanical Engineers, Part C: Mechanical Engineering Science,* vol. 200, no. 3, pp. 155-166, 1986.

[36] E. N. Eliopoulos and T. P. Philippidis, "A progressive damage simulation algorithm for GFRP composites under cyclic loading. Part I: Material constitutive model," *Composite Science and Technology,* vol. 71, no. 5, pp. 742-749, 2011.

[37] E. N. Eliopoulos and T. P. Philippidis, "A progressive damage simulation algorithm for GFRP composites under cyclic loading. Part II: FE implementation and model validation," *Composite Science and Technology,* vol. 71, no. 5, pp. 750-757, 2011.

[38] W. V. Paepegem, J. Degrieck and P. De Baets, "Finite element approach for modelling fatigue damage in fibre-reinforced composite materials," *Composites Part B: Engineering,* vol. 32, no. 7, pp. 578-588, 2001.

[39] V. G. Mejlej, D. Osorio and T. Vietor, "An Improved Fatigue Failure Model for Multidirectional Fiber-reinforced Composite Laminates under any Stress Ratios of Cyclic Loading," *Procedia CIRP,* vol. 66, pp. 27-32, 2017.

[40] B. Mohammadi, B. Fazlai and D. Salimi-Majd, "Development of a continuum damage model for fatigue life prediction of laminated composites," *Composites Part A: Applied Science and Manufacturing,* vol. 93, pp. 163-176, 2017.

[41] L. Zhao, M. Shan, H. Hong, D. Qi, J. Zhang and N. Hu, "A residual strain model for progressive fatigue damage analysis of composite structures," *Composite Structures,* vol. 169, pp. 69-78, 2017.

[42] A. Muc, "Design of composite structures under cyclic loads," *Computers & Structures,* vol. 76, no. 1-3, pp. 211-218, 2000.

[43] M. A. Miner, "Cumulative damage in fatigue," *Journal of Applied Mechanics,* vol. 12, no. 3, pp. A159-A164, 1945.

[44] Y. Liu and S. Mahadevan, "Probabilistic fatigue life prediction of multidirectional composite laminates," *Composite Structures,* vol. 69, no. 1, p. 11–19, 2005.

[45] M. M. Shokrieh and L. B. Lessard, "Multiaxial fatigue behaviour of unidirectional plies based on uniaxial fatigue experiments — I. Modelling," *International Journal of Fatigue,* vol. 19, no. 3, pp. 201-207, 1997.

[46] M. M. Shokrieh and L. B. Lessard, "Multiaxial fatigue behaviour of unidirectional plies based on uniaxial fatigue experiments — II. Experimental evaluation," *International Journal of Fatigue,* vol. 19, no. 3, pp. 209-217, 1997.

[47] F. H. Bhuiyan and R. S. Fertig III, "Predicting matrix and delamination fatigue infiber-reinforced polymercomposites using kinetic theory of fracture," *International Journal of Fatigue,* vol. 117, pp. 327-339, 2018.

[48] A. Plumtree and L. Shi, "Fatigue damage evolution in off-axis unidirectional CFRP," *International Journal of Fatigue,* vol. 24, no. 2-4, pp. 155-159, 2002.

[49] A. T. Turon, Simulation of delamination in composites under quasi-static and fatigue loading using cohesive zone models, Girona: University of Girona, 2006.

[50] O. J. Nixon-Pearson, S. R. Hallett, P. W. Harper and L. F. Kawashita, "Damage development in open-hole composite specimens in fatigue. Part 2: Numerical modelling," *Composite Structures,* vol. 106, pp. 890-898, 2013.

[51] "NASA CompDam - Deformation Gradient Decomposition (DGD)," NASA, [Online]. Available: https://github.com/nasa/CompDam_DGD. [Accessed 21 January 2021].

[52] T. Flatscher and H. E. Pettermann, "A constitutive model for fiber-reinforced polymer plies accounting for plasticity and brittle damage including softening – Implementation for implicit FEM," *Composite Structures,* vol. 93, no. 9, pp. 2241-2249, 2011.

[53] A. I. Gagani, A. Kraukalis, E. Sæter, N. P. Vedvik and A. T. Echtermeyer, "A novel method for testing and determining ILSS for marine and offshore composites," *Composite Structures,* vol. 220, pp. 431-440, 2019.

[54] I. Koch, M. Zscheyge, K. Tittmann and M. Gude, "Numerical fatigue analysis of CFRP components," *Composite Structures,* vol. 168, pp. 392-401, 2017.

[55] P. Rozylo, "Experimental-numerical study into the stability and failure of compressed thin-walled composite profiles using progressive failure analysis and cohesive zone model," *Composite Structures,* vol. 257, p. 113303, 1 February 2021.

[56] J. Brunbauer, C. Gaier and G. Pinter, "Computational fatigue life prediction of continuously fibre reinforced multiaxial composites," *Composites Part B,* vol. 80, pp. 269-277, 2015.

[57] Safe Technology Limited, Safe Technology LimiteFe-safe/Composites, Composite Durability Analysis Software for Finite Element Models, Sheffield: Safe Technology Limited, 2010.

[58] W. R. Broughton, M. R. L. Gower, M. J. Lodeiro, G. D. Pilkington and M. R. Shaw, "An experimental assessment of open-hole tension–tension fatigue behaviour of GFRP laminate," *Composites Part A: Applied Science and Manufacturing,* vol. 42, no. 10, pp. 1310-1320, 2011.

[59] S. Giancane, F. W. Panella, R. Nobile and R. Dattoma, "Fatigue damage evolution of fiber reinforced composites with digital image correlation analysis," *Procedia Engineering,* vol. 2, no. 1, pp. 1307-1315, 2010.

[60] A. Muc, M. Barski, M. Chwal, P. Romanowicz and A. Stawiarski, "Fatigue damage growth monitoring for composite structures with holes," *Composite Structures,* vol. 189, pp. 117-126, 2018.

[61] Y. He, A. Makeev and B. Shonkwiler, "Characterization of nonlinear shear properties for composite materials using digital image correlation and finite element analysis," *Composite Science and Technology,* vol. 73, pp. 64-71, 2012.

[62] A. Makeev, "Interlaminar shear fatigue behavior of glass/epoxy and carbon/epoxy composites," *Composite Science and Technology,* vol. 80, pp. 93-100, 2013.

[63] A. P. Vassilopoulos and R. Bedi, "Adaptive neuro-fuzzy inference system in modelling fatigue life ofmultidirectional composite laminates," *Computational Materials Science,* vol. 43, no. 4, pp. 1086-1093, 2008.

[64] G. L. Golewski, "Evaluation of fracture processes under shear with the use of DIC technique in fly ash concrete and accurate measurement of crack path lengths with the use of a new crack tip tracking method," *Measurement,* vol. 181, p. 109632, August 2021.

[65] 3B, "HiPertex W2020 datasheet," 3B, Hoeilaart, 2015.

[66] Momentive, Technical Datasheet Epikote Resin MGS RIMR 135 and Epikure Curing Agent MGS RIMH 134 - RIMH 137, Waterford: Momentive, 2006.

[67] T.-K. Hwang, J.-B. Park and H.-G. Kim, "Evaluation of fiber material properties in filament-wound composite," *Composites: Part A,* vol. 43, no. 9, pp. 1467-1475, 2012.

[68] J. Cain, S. Case and J. Lesko, "Testing of Hygrothermally Aged E-Glass/Epoxy Cylindrical Laminates Using a Novel Fixture for Simulating Internal Pressure," *Journal of Composites for Construction,* vol. 13, no. 4, pp. 325-331, 2009.

[69] M. R. Etemad, E. Pask and C. B. Besant, "Hoop strength characterization of high strength carbon fibre composites," *Composites,* vol. 23, no. 4, pp. 253-259, 1992.

[70] W. LePage, "Digital Image Correlation," Will LePage, [Online]. Available: https://digitalimagecorrelation.org/. [Accessed 21 September 2021].

[71] L. J. Broutman and R. H. Krock, Fracture and Fatigue: Composite Materials, Volume 5, New York: Academic Press, 1974.

Appendices

Paper I

Research Article

Eivind Hugaas* and Andreas T. Echtermeyer

Filament wound composite fatigue mechanisms investigated with full field DIC strain monitoring

Abstract: Fatigue of filament wound materials was investigated using Digital Image Correlation DIC monitoring every 50th cycle of a high cycle fatigue test of a split disk ring sample. The ring was cut from a filament wound glass fiber reinforced polymer pressure vessel and had a hole. The strain field redistributed over time, lowering and moving strain concentrations. The redistributive behavior was most extensive in areas that later developed local fiber failure, which soon led to catastrophic failure. Microscopy was carried out on partially fatigued material. Damage evolved as matrix cracks and matrix splitting of groups of fibers and complete debonding of single fibers. This occurred at borders of voids and matrix cracks, easing progressive fiber failure. It was concluded that fatigue in filament wound composites has an extensive matrix damage phase before final failure. Fibers could locally withstand strains close to and above the static failure strain for considerable number of cycles if little local strain field redistribution was observed. The used method was able to detect changes in the strain fields that preceded catastrophic failure. It was concluded that DIC combined with the post processing methods presented may serve as a valuable tool for structural integrity monitoring of composite pressure vessels over time.

Keywords: Composites; Filament Winding; Fatigue; Digital Image Correlation; Progressive damage; Strain Fields

1 Introduction

Composite pressure vessels are widely used for transporting and storing gas, especially hydrogen. Understanding how fatigue damage initiates and grows is critical for this application and for further development of predictive models. The current design/verification standards demand full scale testing of every new pressure vessel design driving up development cost. Additionally there are very tight tolerances on wear and damage from use, leading to potential premature decommissioning. A better understanding of the long-term properties can optimize the use of composite materials and simplify the testing requirements, giving leaner and cheaper designs [1–6].

Testing of composite pressure vessels can be simplified by testing of curved filament wound samples as an alternative to tedious full scale testing of the vessels. Currently, the split disk method is perhaps the most pragmatic and easy to use. The method does introduce complexities that need addressing. Most critical being the influence of the split on the through thickness strain fields. Prior research suggests that the strain concentration introduced through friction between the split of the disk and the specimen is negligible provided that the friction between sample and disk is low [7, 8]. However, through thickness strain concentrations will arise from bending [9]. These will be located at the outside surface at the split and inside surface at the center, as indicated in green squares and lines in Figure 1. The hole in the specimen was introduced to further concentrate the strain simulating damage in a pressure vessel. The hole concentrates the strain to four known points as indicated by black circles in Figure 1.

The non-homogenous nature of composites, such as variations in the fiber and matrix distribution, makes traditional single point strain monitoring methods insufficient, such as strain gauges. Knowledge of the entire strain field would be needed. This particularly applies when studying damage evolution, where strain fields may change over time due to progressive damage development. With the advent of ever larger processing power of computers it is now possible to use full field strain monitoring technologies with a data acquisition frequency suitable for fatigue testing. One such high-resolution monitoring method is Digital Image Correlation (DIC) strain monitoring.

Matrix voids and layer thickness in particular tend to vary extensively throughout the layup when using filament winding [10]. Layer thickness will naturally affect the local

---
*Corresponding Author: Eivind Hugaas: Norwegian University of Science and Technology, NTNU Trondheim, Norway; Email: eivindh_5@hotmail.com
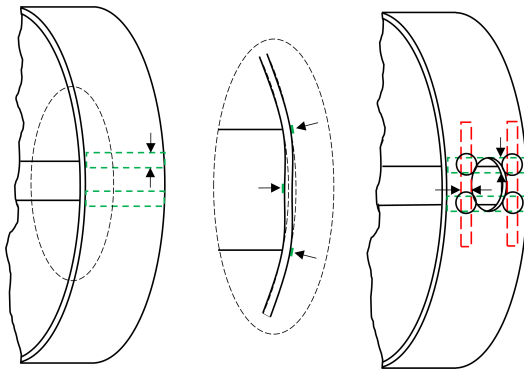**Andreas T. Echtermeyer:** Norwegian University of Science and Technology, NTNU Trondheim, Norway

Figure 1: Schematic illustrating the strain concentration from bending in a split disk sample in green squares and lines and the further concentration introduced with a hole. Arrows and circles further highlight the strain concentrations.

strain fields through varying amounts of loadbearing material. Matrix voids affect the mechanical properties and strength of unidirectional composite materials to a great extent, particularly under cyclic loading, as shown by several recent publications [11–15]. It is therefore to be expected that fatigue damage in a filament wound component will be dominated by matrix damage and also have a considerable scatter and variation in mechanical properties, lifetime and strain fields. The possible spatial variation of properties makes DIC a particularly useful monitoring method, since DIC can monitor the entire surface of the test specimen.

DIC has been shown to be a powerful tool for monitoring composite fatigue. Prior studies utilizing DIC [16–18] have concluded that there is extensive strain field evolution and damage development throughout the fatigue life. Post processing high frequency DIC data is however computationally expensive. Little effort has so far been made to tailor the post processing to better highlight fatigue damage growth of composites besides acknowledging that it can be extensive and progressive. For static properties however, some efforts have been made. He *et al.* [19] used DIC of short beam shear tests combined with a finite element iterative algorithm to find mechanical constants. He's algorithm matched the FEA strain field with the DIC strain field by iteratively changing the mechanical constants and a consistent convergence was found.

DIC is a good candidate for structural integrity monitoring of pressure vessels. A potential alternative is optical fibers embedded in the vessel's laminate. They have recently been tested as an integrity monitoring tool for fatigue and impact damage, most notably by Munzke *et al.* [20] and Saeter *et al.* [21]. Both studies found that while the tech-

nology provided the desired information and gave good indication of the structural integrity, noise and measurement failure from wear on the optical fibers was an issue. In addition, the embedding of the optical fibers into the pressure vessel is an elaborate process. Unlike DIC, optical fibers or strain gauges may only capture the strain in the direction they are mounted, while DIC captures the full field strain in all directions. Post processing signals from optical fibers using the Rayleigh Backscatter method, virtual gauge lengths may be down to 5 mm. The Rayleigh method is the optical fiber post processing method that gives the highest spatial resolution, on par with conventional strain gauges. The virtual gauges may be placed with 1 mm intervals, giving 1.5 mm overlap [21, 22]. The DIC on the other hand have a spatial resolution that is only dependent on the speckle pattern and camera resolution, in theory this may therefor be down to the atomistic level. In practical engineering terms using conventional equipment, the resolution can easily be down to 0.5 mm gauge length, with intervals that can easily be 1/10 of the gauge length, such as used in this study. The only drawback of DIC is that it may not perform measurements at the very high frequency regime which strain gauges may be able to. However, DIC is a rapidly evolving technology and any weaknesses of today may be solved tomorrow. Advanced software is freely available on the net [23–25] and it is seeing a rapid development commercially, such as being embedded in commercial cellphones [26]. It's therefore a technology with a high scientific potential. Identifying its possible appliances, such as for structural health monitoring of pressure vessels and damage development in composites, is the first step on the way to introduce DIC to new fields, where it may give high gains.

This paper investigates mechanical fatigue in a filament wound ring with a hole tested by the split disks method monitored with DIC. The hole was introduced to investigate how fatigue damage evolves around a strain concentrator, simulating damage in a pressure vessel. The study looks into the changes of the surface strain field with increasing number of cycles around several strain concentrators to explain the scatter and evolution of fatigue damage that may be inherent with filament wound materials. This paper also suggests how the DIC post processing methods used may serve as a valuable structural integrity monitoring tool for pressure vessels in use.

2 Experimental setup

2.1 Split disks

The fatigue test was performed on a composite ring cut from a pressure vessel loaded by a split disk in a tension rig. The split disks and the sample had equal dimensions; 50 mm wide and 140 mm in diameter, see schematic in Figure 2. The disks were split by an 11 mm gap, as can be seen in Figure 2. The split disk setup with sample installed can be seen in Figure 3. To minimize the friction between the sample and the disks, industrial grease was used as lubricant. The split disk rig was designed for loads up to 100 kN, roughly twice the testing load.
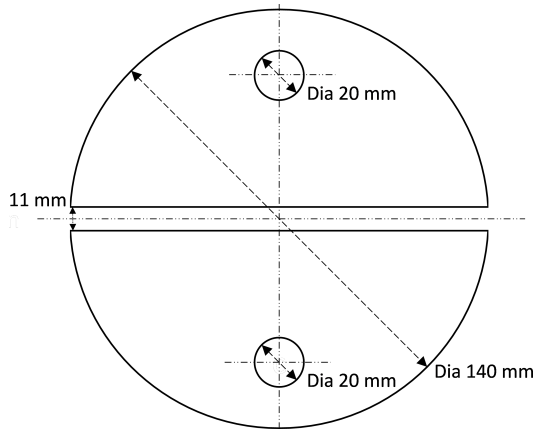
Figure 2: Schematic drawing of the split disks.
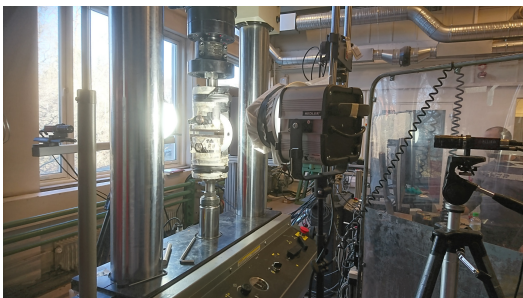
Figure 3: Split disk setup with composite ring installed. Cameras on each side and strong lights to provide enough light for the short shutter speed.

2.2 DIC setup

Figure 3 shows the DIC setup, a system from isi-sys. Two cameras were employed, one on each side of the split disk to be sure to capture damage development on both sides. 2D DIC was used as only the area around the hole was of interest, here the total curvature over the camera frame was deemed too low to necessitate 3D DIC. The shutter speed was set as low as possible without compromising brightness. Strong light sources were used to accommodate the short shutter speed. The cameras where synchronized against the test machine's force output, taking pictures at peak load. The image acquisition period (cycles between each picture) was 50 cycles.

The DIC resolution was checked and peak strain was found to converge for the chosen resolution. When using DIC to capture steep strain gradients in high strain areas, some noise will result [27, 28]. A running average over 1000 cycles was used to smooth the strain data in each point.

2.3 Loading scheme

The test sample was fatigue loaded with a sinusoidal load vs. time sequence. The maximum load was 40 kN and the R-ratio was 0.1. Failure occurred at 127815 cycles. The R-ratio of 0.1 is typically used in testing and is a reasonable R-ratio for a pressure vessel in use, with pressures ranging from almost empty to full. The load frequency was set to 1 Hz. This is quite low, but any higher frequency caused excessive frictional heat and subsequent heat affected epoxy, as investigated during preliminary tests on other rings from the same pressure vessel.

3 Materials and fabrication

3.1 Samples

The split disk test sample was cut from a filament wound pressure vessel wound with a layup of [$\pm 89^{\circ}_2$, $\pm 15^{\circ}_1$, $\pm 89^{\circ}_2$, $\pm 15^{\circ}_1$]. Using the filament winding production method, it is not possible using conventional approaches to manufacture laminates with exactly straight angles in the hoop direction and particularly the axial direction; which has to be helically wound. 89° (nearly hoop) and 15° (nearly axial) were the highest/lowest angles that were possible to produce without compromising on quality given the filament winding machine and mandrel used. The layup was chosen based on the following requirements.

- Base the layup on a $[\sim90°,\sim0°]_n$ layup as this is a commonly used layup in pressure vessels.
- Avoid extensive matrix splitting along the fibers in the loadbearing layers.
- No more than four hoop layers to avoid exceeding the maximum force limit of the test machine.
- Have the inner layer as a non-loadbearing layer to hinder any friction between the splits of the disk and the inner layer affecting the loadbearing layers.
- No more than two helical layers to keep production time within the pot life of the epoxy. (Winding helical layers is time consuming.)
- Keep overall thickness low to hinder too big variation in through thickness strains.

Experience suggests that having only hoop layers in the layup induces extensive matrix splitting along the fibers when testing with the split disk method. Essentially splitting the sample into several smaller samples. This is particularly true for samples with a natural strain concentration inducing shear strains, such as the hole used in this study. Axial layers hinder this behavior as they can transfer some of the shear, particularly if distributed evenly across the layup. With the epoxy, filament winding machine and fiber used in this study the $[\pm89°_2, \pm15°_1, \pm89°_2, \pm15°_1]$ was judged as being the best compromise given the mentioned constraints.

The geometry of the sample can be seen in Figure 4, θ indicates winding angle. The 20 mm hole was machined with a 20 mm milling tool, 40200-HEMI produced by Seco Tools, which assured minimal fiber and matrix damage around the circumference. To ensure a smooth exit of the tool at the inside of the sample, the holes were machined with a polyethylene liner tightened against the composite ring.

The fiber in the vessel was HiPerTex W2020 produced by 3B [29] with resin Epikote MGS RIMR 135 mixed with curing agent Epikure RIMH 137, both produced by Momentive [30]. The winding mandrel, a 140 mm outer diameter polyethylene pipe with steel domes was cut and extracted after winding. The epoxy does not bond to polyethylene and the coefficient of thermal expansion is higher for the PE than the epoxy, making for easy extraction of the liner when cooled to or below freezing. Curing was done for 15 hours at 80°C.
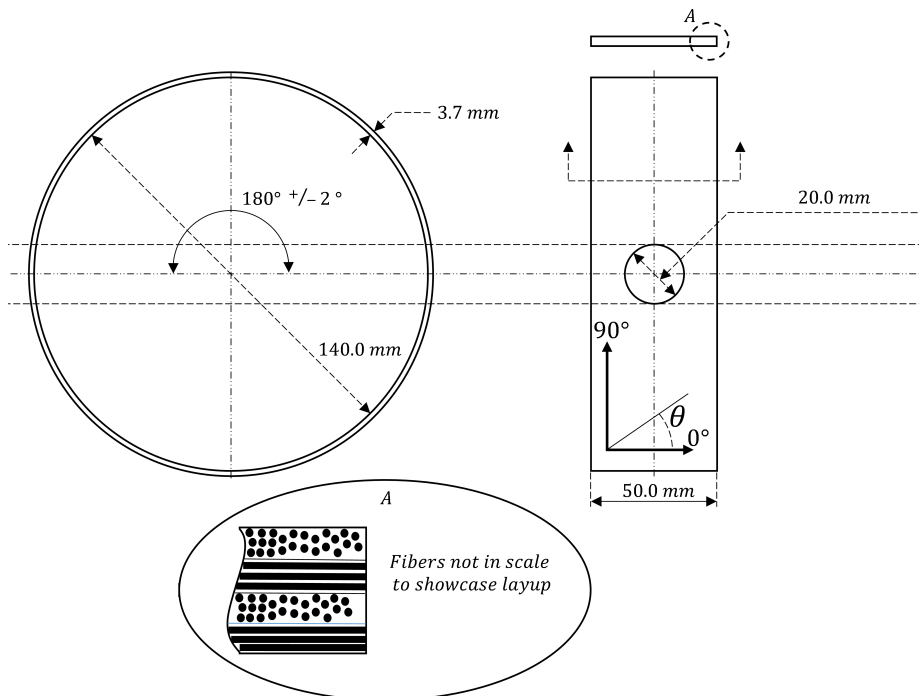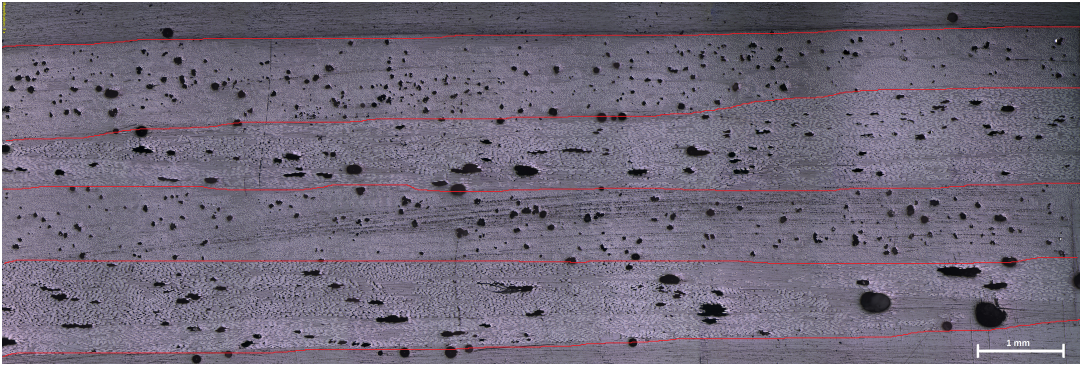

Figure 4: Composite ring sample geometry.

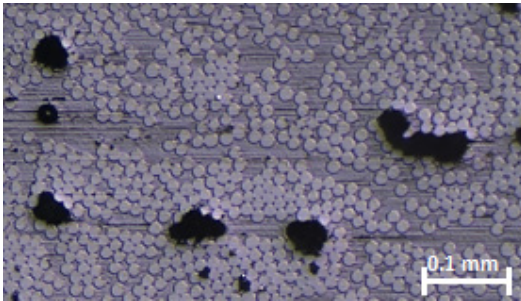**Figure 5:** Microscopy of the pressure vessel.

Figure 6: Detailed microscopy showing individual fibers.

3.2 Material characterization

A material characterization was carried out using burn-off testing and microscopy to assess the fiber volume fraction, void content and typical variation in layer thickness. The burn-off test gave a fiber volume fraction of 0.52 using the procedure described in ASTM D3171 – 15 [31]. However, as noted by E. Hugaas [32], when using burn-off testing, any voids will give an artificially high fiber volume fraction. Looking at the microscopy picture in Figure 5 it is evident that the void content is considerable and the actual volume fraction of fibers is consequently lower. Figure 6 shows detailed microscopy down on the individual fiber level. Consequently the actual volume fraction of matrix is also low, while the volume fraction of free space is relatively high. The fiber volume fraction measured here is typical for many structures made by filament winding while it would be high for typical flat panels made by vacuum assisted resin infusion or pre-preg consolidation.

Also evident in the microscopy is a considerable variation in layer thickness. As strain rather than stress is the property of interest for the work in this paper, the volume

Table 1: Material properties.

Material parameter	Value Perillo [10]	Value 3B [29]	Unit
E_1	33.06 (38.6)	-	GPa
X_t	732 (855)	-	MPa
$\hat{\epsilon}_{1t}$	22150 (X_t/E_1)	31000-33000	Microstrain

fraction matters less as the failure strain of the fiber is not affected. However, it will influence the fatigue properties through faster matrix crack growth with more voids [14]. Table 1 shows properties of the used material previously measured by Perillo [10], along with the maximum strain for the fiber from the fiber supplier, 3B [29]. The maximum stress in fiber direction for the data from Perillo was linearly converted to maximum strain by equation (1). Only the maximum fiber strain was available from the fiber supplier as they do not have test data for this particular combination of constituents. As can be seen, there is a big difference between 3B's and Perillo's maximum strain. The deviation is likely due to a more idealized test setup for the supplier's data and more careful handling of the fibers than in the filament winding machine.

$$\hat{\epsilon}_{1t} = \frac{X_t}{E_1} \qquad (1)$$

4 Results

4.1 DIC

Line slices were used to investigate strain development over the highest strained cross sections. Figure 7 shows schemat-
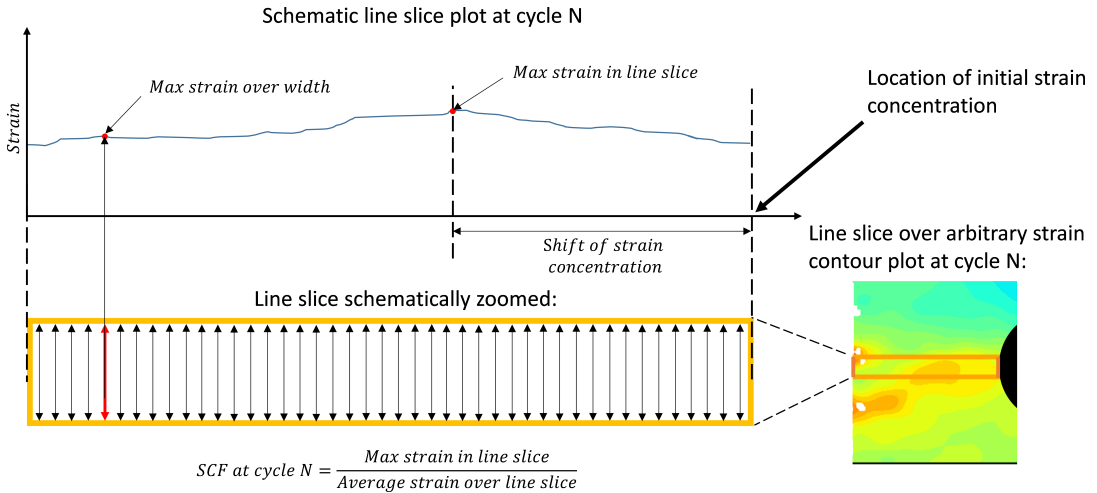
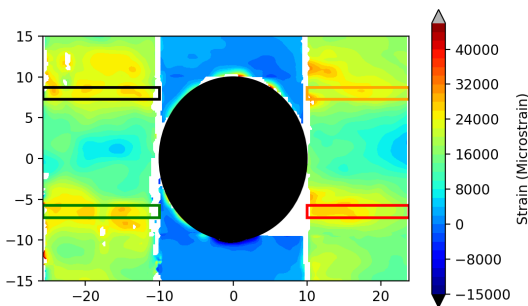**Figure 7:** Schematic description of a line slice.

Figure 8: Line slices over hoop strain contour plot at failure. First point of failure in the surface material is indicated by the voids inside the black line slice. Notice also the shear splitting along the tangent to the hole, leaving the center with little load bearing material.

ically how line slices were defined and how the shift of peak strain was defined on the line slices. The peak strain shift was used as a measure of strain field redistribution. Due to the inherent non-uniform strain distribution, line slices had to be defined over a width as well as a length to capture all relevant strain fields that would otherwise be located at the intended line slice provided a perfect material.

The line slices were located at the interesting areas with strain concentrations shown in the contour plot given in Figure 8 for hoop strain within 50 cycles from the failure cycle. Shift of peak strain and Strain Concentration Factor (SCF) plots for the slices can be seen in Figure 9. The peak strain shift zero value is relative to where the peak strain was in the first cycle recorded by the DIC (therefor all strain

shifts starts at 0 mm). Catastrophic failure was initiated as fiber failure inside the black line slice indicated by the voids in the left side of the slice. Fiber failures developed over the last 400 cycles before catastrophic failure. Extensive shear splitting along the tangents to the hole can be seen as tangential white voids. The shear splits were initiated already during the first cycle and grew progressively throughout cycling. Note: Bending lowers the strain in the center as depicted in Figure 1.

The strains along the cross section in the line slices with most and least strain redistribution are shown in Figure 10 and Figure 11 for different fatigue cycles. The line slices are the black and orange line slices shown in Figure 8.

4.2 Microscopy

At ultimate failure the ring specimen broke into two parts on only one side near the hole. All strain evaluations presented above were done for the side that failed. The other side had similar partial damage developing near the second hole. This side was used for investigating partial damage by microscopy. Small samples could be cut out and polished for the investigation having internal damage from fatigue that is not affected by the final catastrophic failure happening on the other side of the ring specimen.

Figure 12 shows microscopy from the bottom hoop layer close to the split of the intact side of the ring, a cross section with high strains where it was deemed likely to also find damage. As can be seen there is extensive matrix cracking (red lines) running between voids in the matrix and along
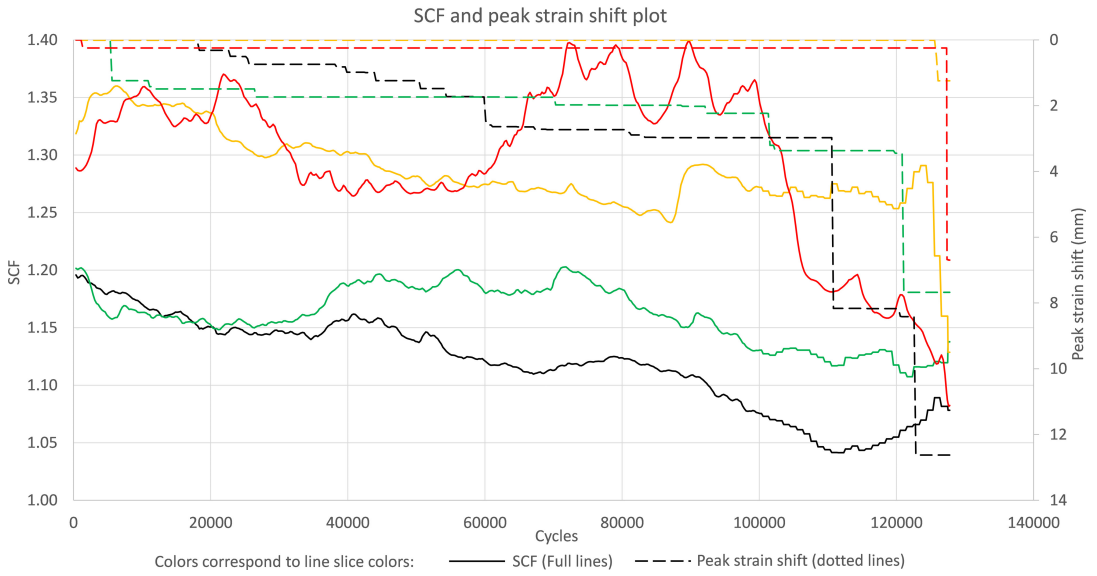
Figure 9: SCF (Maximum strain/average strain) over line slices with the peak strain shift. As can be seen, the SCF is proportional to the redistribution and is steadily falling and lower for the areas with the most redistribution, black and green.
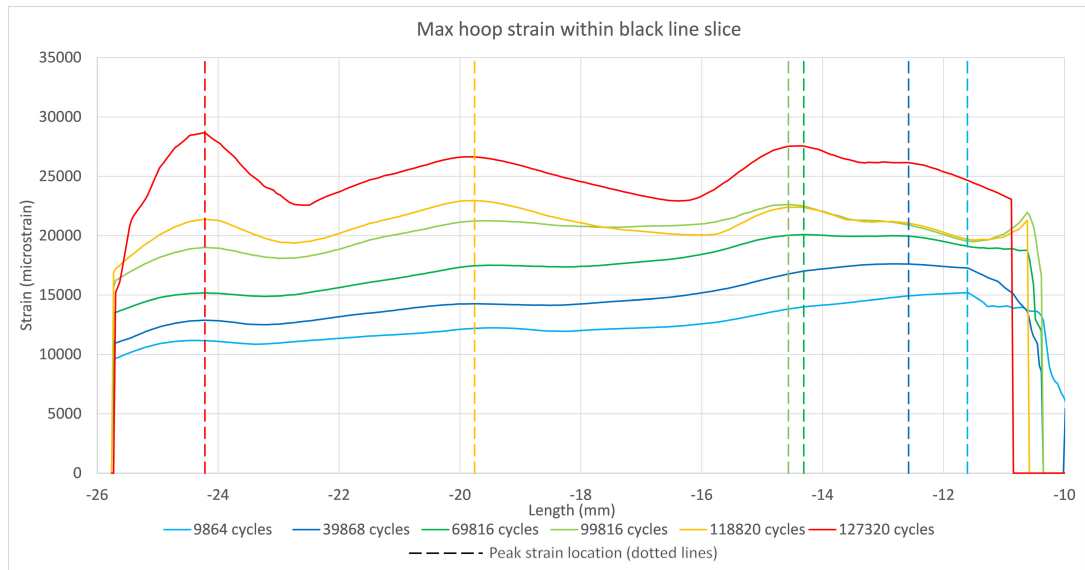

Figure 10: Maximum hoop strain over the black line slice with location of peak strain over the line slice thickness plotted. As can be seen there is extensive redistribution occurring.
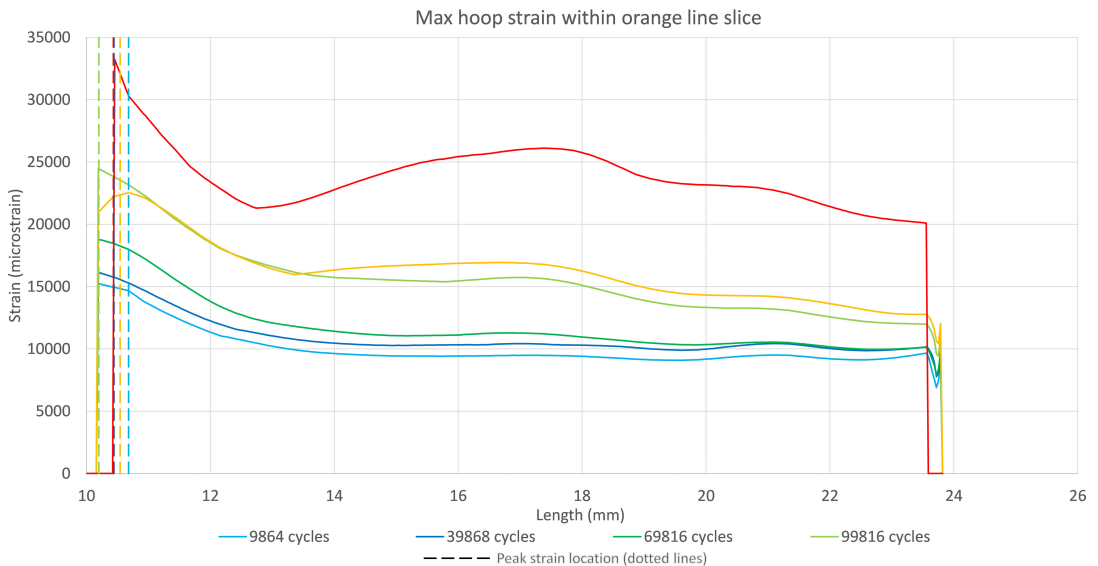
Figure 11: Maximum hoop strain over the orange line slice with location of peak strain plotted, despite high local strains, there is little redistribution due to low strains in the area surrounding peak strain at 10 mm.
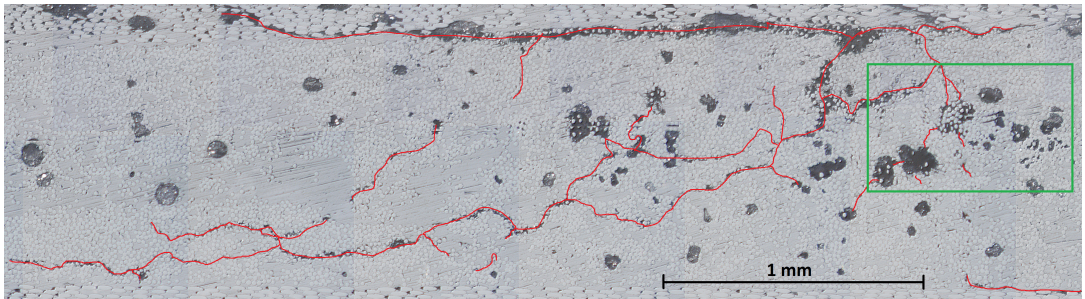

Figure 12: Microscopy of the most strained intact side of the ring with matrix cracks indicated. The green square refers to Figure 13.

the layer interfaces as delamination. This supports the work by Plumtree and Shi [33] and Maragoni *et al.* [12, 14] who found that matrix voids ease matrix cracking in fatigue and that matrix cracks prefer to propagate in between voids.

Figure 13 shows the green area outlined in Figure 12. The areas highlighted in red can be seen to contain debonded fibers and some split of groups of fibers. What may be fractured material can also be seen to be spread as "dust". The matrix splitting and debonding can be seen to have nucleated from the walls of matrix voids and cracks.

Figure 14 shows the fracture, where the DIC results are from. Due to the evidently chaotic nature of the fracture, SEM or microscopy of the fracture was impractical. The microscopy of the damaged material in Figure 12 and Figure 13

was found sufficient to give support to the findings from the strain graphs. The image of the fracture does however highlight where and how catastrophic failure progressed. As can be seen, fiber failure follow the high strain areas in the DIC images outlined with the same colors as in Figure 8. The fiber failures can be seen to "jump" from side to side across the center, likely as an effect of where matrix damage extended across the sample. Inside the black rectangle in Figure 14 it is possible to identify the first fiber failure observed as voids inside the black rectangle in Figure 8, the fiber failure is outlined with red arrows in the figure.
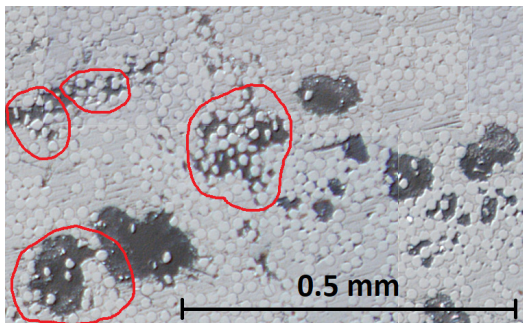
Figure 13: Zoomed area from Figure 12. As can be seen, fiber groups have split from the bulk material and some fibers have completely debonded; here fiber failures can easily interconnect. Red circles highlight the most damaged areas.
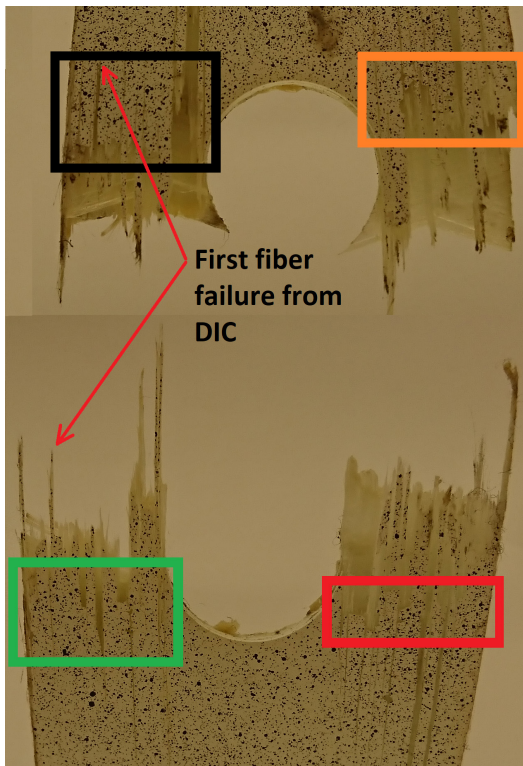

Figure 14: Image of the failed specimen with fiber failure origins outlined in colored squares. The final fracture line runs along both upper and lower side of the specimen and the fiber failures "jump" across the center of the specimen. First fiber failure from the DIC contour plot in Figure 8 is outlined.

4.3 Discussion

There is a varying redistribution of strain near the hole for the different line slices and a marked lowering of the Strain Concentration Factor (SCF), as presented in Figure 9. The largest shift of the position of the peak strain was 12.5 mm happening in the black line slice. The change of SCF was only from 1.2 to 1.05. The highest change in SCF was from about 1.35 to 1.1 for the red and yellow line slices. In both cases the peak strain position remained constant through most of the fatigue life and changed by 6 to 10 mm over the last few hundred cycles. Somewhat surprisingly the first fiber failure happened in the black line slice. This slice has the lowest SCF and lowest peak strain, evident by comparing Figure 10 and Figure 11. The black line slice did however have the highest average strain over the cross section, also evident by comparing Figure 10 and Figure 11.

For fiber failure to progress through the layup and cause loss of structural integrity (catastrophic failure), the matrix has to be sufficiently damaged for fiber failures to coalesce [34, 35]. Considering the fact that fiber failure in this test is sudden, the redistribution of strain is likely an attribute of matrix damage. Supporting this is also the fact that any fiber failure would likely increase the SCF, not lower it, such as for a propagating crack tip. Matrix damage on the other hand reduces the shear stiffness, hindering forces to be transferred between fibers and thus lowering the effect of geometric strain concentrators. The effect is schematically explained in Figure 15. Matrix damage also includes delamination, as indicated in the figure, but which is difficult to measure directly by DIC. The reason why the orange line slice can sustain higher point wise strains than the black is likely due to less matrix damage development, as evident by the smaller strain shift and higher SCF for this area.

For both the orange and the black line slice, peak strain is at or above the ultimate static strain to failure of 22150 microstrain (obtained from standard coupon testing) for a considerable span of cycles, almost 9000 cycles. The orange line slice has strains in the vicinity of the strain to failure reported by the fiber's producer when approaching the last cycles before failure, about 30000-35000 microstrain. This is around 5000 microstrain higher than the black line slice for the same cycle. Again, the orange line slice can likely sustain such high strains due to it having a relatively small amount of matrix damage locally so that any fiber failure may not progress. For both the black and the orange line slices, the high strain relative to the average coupon test strain is an attribute of that the actual strains are measured locally. The strains are not averaged over a larger area or es-
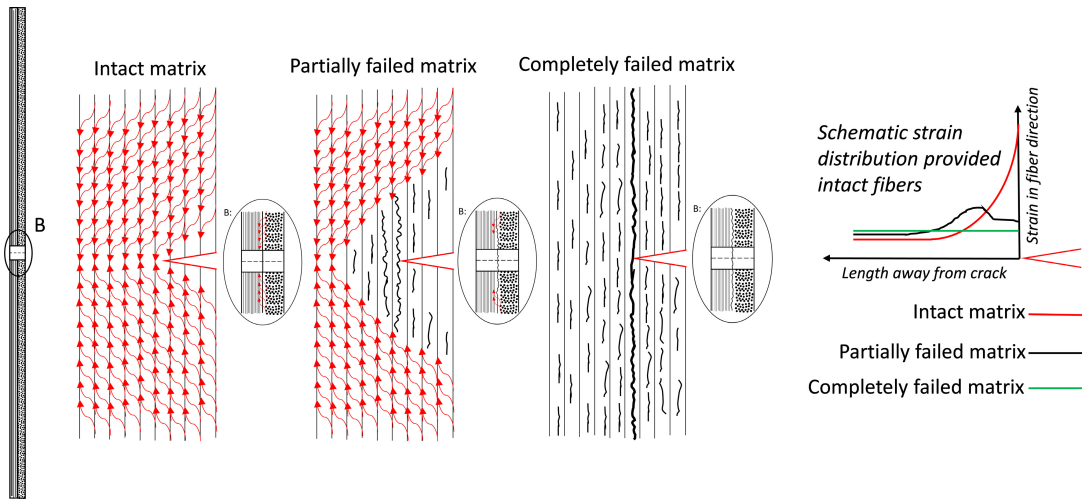
Figure 15: Effect of loss of shear stiffness through matrix damage on the strain distribution around a notch.

timated based on global displacement from a test machine, as in a coupon test.

Looking at the microscopy in Figure 5 the void content is extensive (but typical for many filament wound structures), which is also apparent in the damaged cross section in Figure 12. As evident in Figure 13 fibers and groups of fibers have debonded at matrix cracks and voids, where they are initially free at one side. Compared to the non-fatigued microscopy in Figure 5 and Figure 6 the difference is evident, it contains no cracks and debonding. Debonding is a known failure mechanism in fatigue of composites [33, 36]. The fact that debonding prefers to occur inside voids and along matrix cracks however explains why voids are detrimental to fatigue performance, as concluded by several past studies [11–15]. Not only do voids facilitate faster propagation of matrix cracks, they also serve as nucleus for fiber debonding. The extent of voids in the microscopy further explains why the strain redistribution is extensive and damage apparently matrix driven. Further, the apparent variation in void content, fiber density and layer thickness explains why damage development varies to such a great extent over the specimen. The variation is another attribute of the filament winding production method.

Composites are often used as replacement for steel in design. Fatigue life in design of steel components is usually calculated as life until crack initiation. This is done at hotspots, which are highly stressed points with a geometric strain concentrator [37], such as the hole in this study. Upon crack initiation, damage progression is rapid and the structural integrity is soon lost. Fatigue damage in composites

is different, as demonstrated in this study. Fatigue damage initiates in the matrix. Matrix damage does not necessarily evolve at points with a high strain concentration factor, it will prefer to evolve in areas with high overall strain, because this increases the likelihood of a locally weakened matrix (*e.g.* by a void) being exposed to a high strain creating local damage. When the matrix is sufficiently damaged, fiber failure may rapidly progress through the material, comparable to the crack growth phase for steels. While the strain distribution changes little for steel components under fatigue loading before crack initiation, composites may undergo major strain field changes as fatigue matrix damage redistributes strain. Fatigue in composites therefor has an additional phase before the crack initiation phase, the matrix damage phase. This phase has been suggested before [38], but not measured directly on the strain field evolution as here. Depending on the component's shape, laminate buildup and loading condition, this phase may be critical or not. For components designed to withstand shear, matrix cracking is critical. Matrix cracking is not critical in the main cylindrical part of pressure vessels, because the inner liner keeps the vessel tight. The fibers are the load-bearing constituents, especially in a cross ply layup in an even stress/strain field without stress concentration points. In such a layup, matrix damage will lessen the effect of geometric strain concentrators as the strain field redistributes and will be positive in this respect.

An aspect of the presented work that is not taken into account is the size and shape of the introduced defect, and how this may affect the strain fields and damage develop-

ment. While damage progression naturally will vary with the imperfections' geometry it is unlikely that it will deviate on the basic principles outlined here; matrix damage and redistribution. Therefor the aspect of the defect shape and size has not been subject for investigation, finding the failure mechanisms and how they may be monitored is the focus of this work.

Due to the inherent big local variation in void content of filament wound composites and not knowing where the regions with high void content are, matrix damage growth will always be difficult to analytically estimate. Conservative worst-case situations may be modeled, but they may predict quite wrong damage development. Statistical methods may be used to model different distributions of voids, but such models will be complicated. This work has shown that monitoring strains by DIC may be a good alternative to modelling in some cases. As laid out in the introduction it may serve as a good in-service health monitoring tool of composite pressure vessels. Any change in the strain field would be a warning of damage having developed. If the new strain field remains constant with time (increasing number of cycles) it would indicate a somewhat weakened but stable structural integrity. If the strain field changes, the peak strains shift, more severe fiber dominated damage may eventually develop.

Strain monitoring with DIC will always depend on the speckle pattern and resolution of the cameras. The two are the main assumptions for the method's functionality. In this work, the DIC resolution was as fine as possible given the used speckle pattern. Provided a finer speckle pattern, the resolution could naturally have been finer and more detailed strain data acquired. A resolution sensitivity study was however carried out and strain field convergence was found for the chosen resolution. When working in the fine resolution regime of any speckle pattern noise may result [28]. The strength of the used method when working in the fine resolution regime is it's noise reduction over the time dimension, the alternative being smoothing over the space dimension in each frame. When smoothing over the space dimension, strain is compared to the neighboring strain, which will be different from the strain in the data point of interest to start with. When smoothing over time, the strain in the same point should remain reasonably stable over the averaged cycles (here 1000). Any noise reduction will make the strain in the datapoint converge towards the actual value and not the neighboring average strain, as for smoothing over the space dimension. The smoothing over time is only possible due to the high frequency of the data. The necessary resolution when dealing with composites will depend on the material and geometry. For other constituents and geometries the damage development may

happen at a smaller scale than for the GFRP material in this work and a higher resolution necessary to find the same mechanisms as here. The question is however at what scale it is necessary to observe damage mechanisms in a material or in a geometry. Damage may occur that is non critical to the strain fields and the structural integrity. In this study, the fact that the strain redistribution clearly develops most extensively for the material sustaining damage first suggests that the resolution is sufficiently fine. Studying strains in the matrix associated directions may also open up for a clearer picture of how the material behave. For this study this was not done out of a scope consideration, but is a good suggestion for further work.

Either standalone or in combination with other health monitoring technologies DIC may serve as a valuable structural integrity tool for pressure vessels. Compared to the optical fiber structural health monitoring method suggested by Munzke *et al.* [20] the presented method has much less noise and is able to give more detailed information on why and how damage develops, at least on the experimental stage. In order for optical fibers or single point strain gauges to catch the same mechanisms, they have to be placed where damage develops and in relatively big numbers. A strain gauge or optical fiber placed where damage was initially thought to develop may therefore not properly catch the strain field development in case the strain field changes with damage. Optical fibers would not be able to give curves with this little noise and this resolution. The fluctuations in the DIC strain would not be possible to catch using 5 mm gauge length, very easily concluded by simply imagining 5 mm strain gauges placed over the x axis in the strain curves in Figures 10–11. Optical fibers with the Rayleigh backscatter method would also not be able to capture strain in anything but a static loadcase. The acquisition time is far longer than the shutter speed of the used cameras for DIC, giving noise if the load is changed during the acquisition. Additionally, for such high strains, the running reference method would have to be used and still then strains in the 30 000 microstrain range would be close to the failure strain of the optical fiber itself [21]. The running reference method would demand stepwise static loading and make fatigue testing extremely time consuming. Strain gauges would be the only practical alternative for monitoring. DIC and strain gauges are hardly comparable as one gauge may give one datapoint out of a thousand or more for the DIC and in only one out of three directions (fiber, matrix and shear). Additionally, the durability issues with the optical fiber reported by Munzke and also Saeter [21] is evidently not a problem with DIC, being much more convenient to implement. On top of all this, the amount of data available when using DIC compared to any other method allows the data processing

competent user to play with the data and find trends that is not possible to discover with other methods, such as the redistribution found in this study. The authors do however recognize that full scale testing may give different results and that strain field development may not be as easy to catch in an industrial vessel as in experiments or in different experimental geometries for that matter. More work is needed testing the methods and technology on actual pressure vessels, also using through thickness methods for comparison.

The DIC system used here is already outdated compared to the cutting edge technological development on the DIC front. It is a technology with big industrial and consumer interest, with algorithms and methods available as open source [23–25] or embedded in commercial hardware such as cell phones, for example for facial recognition [26]. Besides investing more work in quantifying acceptable strain changes, the principles outlined here may serve as a basis for developing a damage detection system relying on an emerging technology with high scientific, industrial and consumer interest. Provided an area of interest in a pressure vessel with known high strains (valve, small damage from use etc.), the post processing concepts outlined in this work may be sufficient information to judge the integrity and potential damage development provided a high resolution image.

5 Conclusion

A split disk fatigue test of a ring with a circular hole cut from a filament wound glass fiber reinforced pressure vessel was carried out. The strain field around the hole was measured by Digital Image Correlation (DIC) at peak load for every 50th cycle. The test lasted 127 000 cycles. It was found that progressive damage in the matrix redistributed strain in the fiber direction throughout the test until catastrophic failure. The redistribution was observed through monitoring Strain Concentration Factors (SCFs) and shift of peak strain location over critical cross sections, both of which lowered and moved with increasing number of fatigue cycles.

While matrix damage redistributed and lowered strain in the direction of the fiber it also eased travel of progressive fiber failure. The area showing most strain redistribution was the area to develop fiber failure first. Other areas with less strain redistribution did not develop fiber failure despite having a higher SCF and strain in the fiber direction in single material points.

Strains could be close to the ultimate strain over considerable cycle spans provided little matrix damage developed locally.

Through microscopy it was found that fatigue damage of the matrix material progressed as debonding of single fibers along borders of matrix cracks and voids. Fatigue of composites occurs in three phases: a stable phase, a matrix damage phase and a sudden fiber failure phase; which marks the end of fatigue life. The strain redistributive behavior of the matrix damage phase may be advantageous in fatigue sensitive applications creating a stable and evenly distributed strain field. Matrix damage may lower strain around any damaged area and make it converge to the far field strain over time, removing the initial strain concentration. Better control of the structural integrity and higher confidence in lifetime evaluations may result from monitoring damaged areas and weak spots in commercial pressure vessels with DIC combined with the post processing methods presented in this study. Considering the rapid growth of image recognition technology, research on such technology for structural integrity monitoring may yield high scientific and commercial gains.

References

[1]   IEA Hydrogen, Global trends and outlook for hydrogen, IEA Hydrogen, 2017.

[2]   J. Degrieck and W. V. Paepegem, "Fatigue Damage Modelling of Fibre-reinforced Composite Materials: Review," *Applied Mechanics Reviews*, vol. 54, no. 4, pp. 279-300, 2001.

[3]   ISO, ISO 11515:2013 (Confirmed in 2019), ISO – International Organization for Standardization, 2019.

[4]   ISO, ISO 11119-3:2013 (Confirmed in 2018), ISO – International Organization for Standardization, 2018.

[5]   J.-P. Antoniotti, "Impact of high capacity CGH2-trailers," *Deliverable 6.4 in EU research project DeliverHy*, 2013.

[6]   J. P. Berro Ramirez, D. Halm, J.-C. Grandidier, S. Villalonga and F. Nony, "700 bar type IV high pressure hydrogen storage vessel burst – Simulation and experimental validation," *International Journal of Hydrogen Energy*, vol. 40, no. 38, 2015.

[7]   I. A. Jones, V. Middleton and M. J. Owen, "Roller-assisted variant of the split disc test for filament-wound composites," *Composites Part A: Applied Science and Manufacturing*, vol. 27, no. 4, pp. 287-294, 1996.

[8]   C. Kaynak, E. S. Erdiller, L. Parnas and F. Senel, "Use of split-disk tests for the process parameters of filament wound epoxy

composite tubes," *Polymer Testing*, vol. 24, no. 5, p. 648–655, 2005.

[9] J. F. Chen, S. Q. Li, L. A. Bisby and J. Ai, "FRP rupture strains in the split-disk test," *Composites Part B: Engineering*, vol. 42, no. 4, pp. 962-972, 2011.

[10] G. Perillo, Numerical and Experimental Investigation of Impact Behaviour of GFRP Composiites (PhD thesis)., Trondheim: NTNU – Norwegian University of Science and Technology, 2014.

[11] S. M. Sisodia, E. K. Gamstedt, F. Edgren and J. Varna, "Effects of voids on quasi-static and tension fatigue behaviour of carbon-fibre composite laminates," *Journal of Composite Materials*, vol. 49, no. 17, pp. 2137-2148, 2015.

[12] L. Maragoni, P. A. Carraro, M. Peron and M. Quaresimin, "Fatigue behaviour of glass/epoxy laminates in the presence of voids," *International Journal of Fatigue*, vol. 95, pp. 18-28, 2017.

[13] J. Lambert, A. R. Chambers, I. Sinclair and S. M. Spearing, "3D damage characterisation and the role of voids in the fatigue of wind turbine blade materials," *Composite Science and Technology*, vol. 72, no. 2, pp. 337-343, 2012.

[14] L. Maragoni, P. A. Carraro and M. Quaresimin, "Effect of voids on the crack formation in a [45/−45/0]s laminate under cyclic axial tension," *Composites Part A: Applied Science and Manufacturing*, Vols. 91, Part 2, pp. 493-500, 2016.

[15] M. Mehdikhani, L. Gorbatikh, I. Veerpost and S. V. Lomov, "Voids in fiber-reinforced polymer composites: A review on their formation, characteristics, and effects on mechanical performance," *Journal of Composite Materials*, vol. 53, no. 12, pp. 1579-1669, 2018.

[16] W. R. Broughton, M. R. L. Gower, M. J. Lodeiro, G. D. Pilkington and M. R. Shaw, "An experimental assessment of open-hole tension–tension fatigue behaviour of GFRP laminate," *Composites Part A: Applied Science and Manufacturing*, vol. 42, no. 10, pp. 1310-1320, 2011.

[17] A. Muc, "Design of composite structures under cyclic loads," *Computers & Structures*, vol. 76, no. 1-3, pp. 211-218, 2000.

[18] S. Giancane, F. W. Panella, R. Nobile and R. Dattoma, "Fatigue damage evolution of fiber reinforced composites with digital image correlation analysis," *Procedia Engineering 2*, vol. 2, no. 1, pp. 1307-1315, 2010.

[19] T. He, L. Liu and A. Makeev, "Uncertainty analysis in composite material properties characterization using digital image correlation and finite element model updating," *Composite Structures*, vol. 184, pp. 337-351, 2018.

[20] D. Munzke, E. Duffner, R. Eisermann, M. Schukar, A. Schoppa, M. Szczepaniak, J. Strohhäcker and G. Mair, "Monitoring of type IV composite pressure vessels with multilayer fully integrated optical fiber based distributed strain sensing," *Materials Today: Proceedings*, 2020.

[21] E. Saeter, K. Lasn, F. Nony and A. T. Echtermeyer, "Embedded optical fibres for monitoring pressurization and impact of filament wound cylinders," *Composite Structures*, vol. 210, pp. 608-617, 2019.

[22] E. Hugaas, A. T. Echtermeyer and N. P. Vedvik, "Buckling due to external pressure of a composite tube measured by Rayleigh optical backscatter reflectometry and analyzed by finite elements," *Structural Control and Health Monitoring: The Bulletin of ACS*, vol. 25, no. 8, 2018.

[23] S. Nordmark Olufsen, M. E. Andersen and E. Fagerholt, "(mu)DIC: An open-source toolkit for digital image correlation," *SoftwareX*, vol. 11, p. 100391, 2020.

[24] J. Blaber, B. Adair and A. Antoniou, "Ncorr: Open-Source 2D Digital Image Correlation Matlab Software," *Society for Experimental Mechanics*, vol. 55, pp. 1105-1122, 2015.

[25] D. Solav, K. M. Moerman, A. M. Jaeger, K. Genovese and H. M. Herr, "MultiDIC: An Open-Source Toolbox for Multi-View 3D Digital Image Correlation," *IEEE Access*, vol. 6, pp. 30520-30535, 2018.

[26] D. Guillaume, X. Chao and K. Sriadibhatla, "Face Recognition in Mobile Phones," Department of Electrical Engineering, Stanford University, 2010.

[27] "Digital Image Correlation," Will LePage, [Online]. Available: https://digitalimagecorrelation.org/. [Accessed 12 May 2019].

[28] N. McCormick and J. Lord, "Digital Image Correlation," *Materials today*, vol. 13, no. 12, pp. 52-54, 2010.

[29] 3B, "HiPertex W2020 datasheet," 3B, 2015.

[30] Momentive, Technical Datasheet Epikote Resin MGS RIMR 135 and Epikure Curing Agent MGS RIMH 134 – RIMH 137, Momentive, 2006.

[31] ASTM, ASTM Standard D3171 – 15 Standard Test Methods for Constituent Content of Composite Materials, ASTM, 2015.

[32] E. Hugaas, Optimize resistance to buckling under external hydrostatic pressure of thin walled composite tubes. (Master thesis), Trondheim: NTNU, 2014.

[33] A. Plumtrée and L. Shi, "Fatigue damage evolution in off-axis unidirectional CFRP," *International Journal of Fatigue*, vol. 24, no. 2-4, pp. 155-159, 2002.

[34] H. Y. Chou, A. R. Bunsell and A. Thionnet, "Visual indicator for the detection of end-of-life criterion for composite high pressure vessels for hydrogen storage," *International Journal of Hydrogen Energy*, vol. 37, no. 21, pp. 16247-16255, 2012.

[35] R. Talreja and W. Watt, "Fatigue of composite materials: damage mechanisms and fatigue-life diagrams," *Proceedings of the Royal Society A*, vol. 378, no. 1775, pp. 461-475, 1981.

[36] A. T. Seyhan, "A Statistical Study of Fatigue Life Prediction of Fibre Reinforced Polymer Composites," *Polymers & Polymer Composites*, vol. 19, no. 9, pp. 717-723, 2011.

[37] DNV GL, DNVGL-RP-C203 Fatigue design of offshore steel structures, Høvik: DNV GL, 2019.

[38] C. Colombo, F. Libonati and L. Vergani, "Fatigue damage in GFRP," *International Journal of Structural Integrity*, vol. 3, no. 4, pp. 424-440, 2012.

Paper II

Estimating S-N curves for local fiber dominated fatigue failure in ring specimens representing filament wound pressure vessels with damage

Eivind Hugaas*, Andreas T. Echtermeyer

Norwegian University of Science and Technology, NTNU, Trondheim, Norway

A B S T R A C T

Modeling the effect of fatigue is important for predicting remaining life of damaged filament wound composite pressure vessels. This study shows how S-N curves can be measured that describe local fiber dominated fatigue failure on the scale of 0.25 mm near stress concentrations caused by a hole representing damage.

High frequency Digital Image Correlation DIC was applied to measure strain fields in rings tested by the split disk method. The rings were cut from a glass fiber reinforced polymer pressure vessel. A hole was cut into the rings to simulate damage in the laminate of the pressure vessel.

The Miner sum cumulative damage is calculated based on strain histories measured by DIC and several assumed S-N curves. The S-N curve giving Miner sum damage closest to the experimentally observed local failures in several samples is taken as the S-N curve describing the material´s behavior best. The local S-N curve was considerably less conservative than nominal S-N curves obtained from standard coupon testing. Its origin was a factor 2.5 higher.

1. Introduction

While local failure progression due to fatigue at large occurs in the matrix material, modeling local fiber dominated failure is important for knowing when and how catastrophic failure occurs [1–3]. This work is part of a larger program to better understand the long-term behavior of damaged composite pressure vessels and concentrates on filament wound composites. If composite pressure vessels are found to have damage in their load bearing laminate they are basically discarded and replaced by new ones. A better understanding of the remaining life with damage would help to make better decisions on the severity of damage. This study describes how S-N curves for local fiber dominated failure obtained from split ring specimens with a hole can be obtained and used to evaluate damage around strain concentrators in pressure vessels and as input for numerical analysis tools. The approach to obtain the S-N curves is unusual, deviating from common test procedures.

Typically S-N curves are measured from coupon samples cut out from flat plates tested in tension [4]. Samples are typically made from fabrics not representing the filament winding process well, but they tend have fairly homogenous characteristics throughout the specimen. One fatigue result is obtained per test with an ideally even (but cyclic) stress/strain level throughout the test volume. Strain gauges may be applied, but give only point-wise strains. Giancane et. al. [5] showed that strains in

a coupon test may vary extensively over the surface and may be much higher towards the grips than in the neck section, where strain gauges are typically placed [4,5]. This indicates that typical coupon testing gives conservative strain to failure curves. This is beneficial for design purposes, but hinders use of the materials full potential.

Fatigue testing samples with a stress raiser, such as a hole, change the situation. The strain field is not even anymore but shows a significant strain concentration. The strain field also changes with increasing number of fatigue cycles due to damage development (matrix cracking, splitting, undulation and delamination and progressive fiber failure) ([6]; Shen & Han, 2018). This occurs even in layers where the fibers are unidirectional and in the loading direction, as this paper shows. Fiber failure in the loadbearing layers will occur somewhere in small designated regions given by an unfavorable combination of high local strains and a statistically weak part of the material, as opposed to a coupon test, where failure may occur anywhere in the area between the grips just at a statistically weak spot [7]. In other words there will be a more direct correlation between the local strain and point of failure. The challenge with introducing a hole is the behavior of composites redistributing strain with increasing number of cycles. Since the fatigue strain at a point varies due to damage development it is not possible to relate the number of cycles of failure at that point to one fatigue strain and to build an S-N curve.
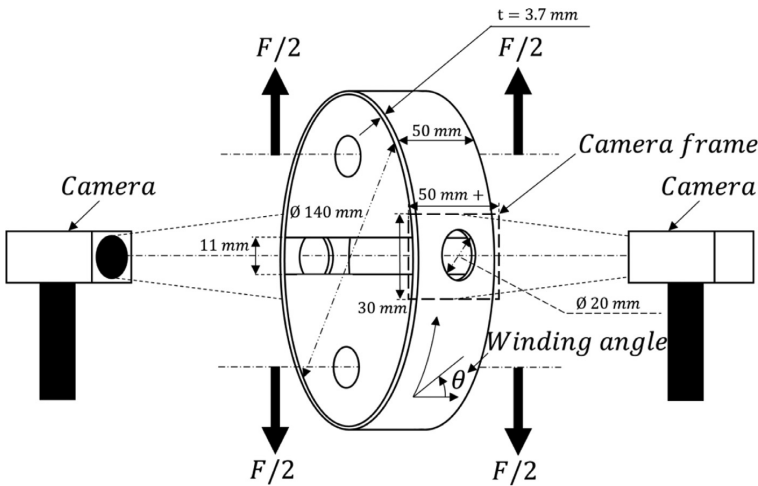
Fig. 1. Schematic of the DIC setup. Note that only the data from the camera monitoring the side that finally failed was used in this work.

This study presents a method that is capable of building an S-N curve from tests with a hole using high frequency DIC data. The high frequency DIC is capable of identifying local fiber failure and find local strain to cycle curves for the failing material points. Utilizing a back calculation method based on Miner sum calculations on the individual strain to cycle curves a best fit S-N curve is found. For a material with no statistical variation of properties each point of local fiber failure should show the same Miner sum value. The initially guessed S-N curve needs to be now changed until all failing points give a Miner sum value of 1. This fatigue curve describes local fiber failure. It is different from the S-N curve obtained by coupon tests that describes the catastrophic failure. In reality the scatter of material properties must be taken into account.

Other damage accumulation rules do exist, however, the Miner damage rule is the currently used rule in standards and industry [8]. Choosing the Miner sum approach is therefore a good starting point. But the presented method has good promise for comparisons of different damage rules. More sophisticated machine learning methods have been used to estimate and predict fatigue behavior, such as that by Wang [9], Rodriguez [10] and Mohanty [11] et al.. These methods do, however, use much less data than in this study and the results are fairly application specific. Combining machine learning and AI methods with DIC and other full field monitoring methods holds great promise for advanced fatigue lifetime modeling. This paper could provide data for that work.

Composite materials exhibit statistical variation in their properties like any material. Local variations related to the production process, such as void content, fiber density and fiber alignment also contribute to the scatter of properties. The number of cycles to failure for local fiber failure will, therefore, also vary. The ideal S-N curve mentioned above describing all local fiber failures does not exist. But it is possible to find an S-N curve that describes the local fiber failures on average and in a conservative way. The method presented here highlights how typical coupon test S-N curves are highly conservative for predicting local damage.

In this study it is not necessary to predict how the strain field changes during fatigue due to damage development as in a numerical model, because the strain field is measured directly by DIC. The aim is to obtain an S-N curve that can predict local fiber failure and subsequent catastrophic failure when enough local fiber failures have accumulated. The S-N curve for local fiber failure can be used in the future for modeling progressive failure under fatigue with finite element analysis. The S-N curve is found by a parameter study approach.

2. Materials and methods

2.1. Experimental setup

Four ring specimen with a hole cut from a filament wound pressure vessel were tested with a split disk setup. The hole was introduced to simulate damage. The split disk method was used as a simple and pragmatic alternative to costly pressure testing of the actual vessels. The ring specimen reflect well the material properties of the filament winding process. Flat coupon specimens, as typically used for fatigue testing, are difficult to produce with the filament winding process, since the fiber tension and alignment is hard to control [12]. Such specimens are often seen as not properly representing the properties of the filament wound component [12].

The tests were monitored with a system from Isi-Sys. Stingray F504B ASG cameras from Allied Vision Technologies (5 MP resolution) were placed on each side of the split disk setup. The cameras focused on the area around the hole, measuring 50*30 mm. Vic-2D, Digital Image Correlation (DIC) software, was used to analyze the images giving strain components. Fig. 1 shows the geometry of the setup and ring.

The split disks were manufactured from steel with a diameter of 140 mm and a width of 50 mm, the same as the ring specimen. The gap between the disks was 11 mm. Two cameras were employed, one on each side of the split disk setup as shown in Fig. 1. Both sides of the setup were monitored as it was not known which side would fail. Only the data from the camera on the failing side was used in the work presented in this article. Note, it is not known at the start of the experiment on which side of the ring failure will happen. The cameras were set to cover an area of roughly 50 mm by 30 mm on each side. As shown by M. A. Sutton et. al. [13] in plane 2D DIC strain errors are proportional to the out of plane motion relative to the distance from the camera to the specimen. Meaning that if the camera is placed far away from the specimen the error is less if there is any out of plane motion. For the ring specimen, the out of plane motion was small and the cameras placed far away (1.5 meter) relative to the potential out of plane motion. Also, the area in the camera frame was in good focus with only one camera. This allowed using a 2D system with sufficient measurement accuracy instead of a stereo system, simplifying the image processing. Using more than two cameras would have been beyond the capabilities of the image processing system. The cameras were timed to the load signal of the test machine taking pictures at peak load. The timing was checked using an external camera.
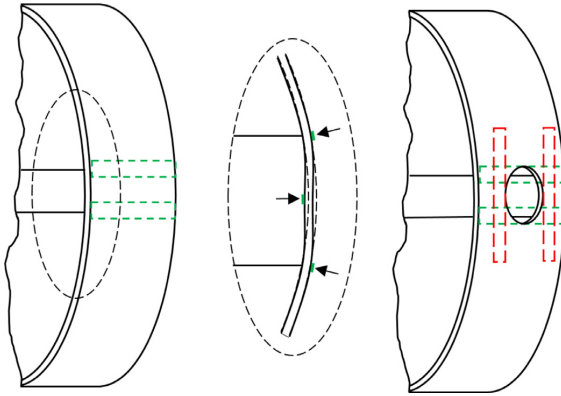
Fig. 2. Schematic of typical strain concentrations in a split disk test with a hole in the sample. Strain concentrations from bending are highlighted in green and the concentrations from the hole are highlighted in red. Arrows are used to further highlight the strain concentrations.

Table 1
Constituents and details on materials and production.

Constituent	Name/Type	Producer
Glass Fiber	HiPerTex W2020	3B [15]
Resin	Epikote MGS RIMR 135	Momentive [16]
Curing agent	Epikure RIMH 137	Momentive [16]
Curing time	15 hours at 80°C.	-
Mandrel	140 mm (outer) diameter polyethylene pipe	In house
Domes	Steel	In house

The split disk setup concentrates strain at the edges of the slit-disk on the outer surface and in the center inner surface due to bending [14], indicated in green in Fig. 2. The hole further concentrates the strain along the red squares. The setup therefor renders defined areas of expected failure.

2.2. Materials and pressure vessel fabrication

The pressure vessel was manufactured on a Mikrosan filament winding machine at NTNU. A polyethylene liner was used as a mandrel for winding. The layup was $[\pm89^\circ_2, \pm15^\circ_1, \pm89^\circ_2, \pm15^\circ_1]$ (Hoop/Axial/Hoop/Axial) from the outside to the inside of the ring ($\pm89^\circ_2$ fibers are on the outside), similar to a cross ply layup as found in most pressure vessels. Emphasis was put on having a hoop layer on the surface, enabling monitoring of a loadbearing layer with the DIC. No transition layers were used, the winding process was started anew for each layer. Also, the hoop layers had no woven pattern as for the axial layers. The hoop layers were as such wound with no filament running over the domes. The non woven nature of the hoop layers minimized any undulation of the fiber and made the fiber angle as close to the loading direction as possible. Fig. 3 shows the winding of the first axial layer of white glass fibers onto the black liner. Table 1 outlines the constituent materials. The ring cut outs were 50 mm wide. The liner was easily extracted from the cut outs as polyethylene does not bond to the epoxy. The holes were cut into the rings with a milling tool for composites (Seco Tools 40200-HEMI). They had a diameter of 20 mm. The geometry of the disks and the split disks can be seen in Fig. 1.

The strain to failure in fiber direction was measured previously in our laboratory for coupons made from the same fibers as used here. It varied between 22000 and 27000 microstrain for six test specimens, with the mean at 22150 microstrain. The fiber producer reports a strain to failure of 33000 mocrostrain [15]. The producer´s strain to failure is

considerably higher than the properties measured in our laboratory. The discrepancy is likely due to the manufacturer testing a more perfectly made material. Static and fatigue properties of the matrix were reported by A. Kraukalis et. al. in [17].

A microscopy study was carried out to assess variations in layer thickness and void content, properties that affect strain distributions. Looking at the microscopy image in Fig. 4 it can be seen that there is a considerable amount of voids in both winding directions and a considerable variation in layer thickness. The void content was not intentionally made high, despite the evidently high void content, standard procedures for filament winding production was followed. Similar imperfections have been observed in other filament wound structures [12]. Due to the high void content, no burn-off test was carried out to estimate fiber volume fraction as this would be artificially high with that much air/voids in the material. Also, the fiber volume fraction does not affect the results, which are strain based and not stress based.

2.3. DIC post processing

Digital Image Correlation, DIC, was used to measure the hoop strain (strain in the loading direction) on the surface of the outer layer. The test samples were painted with a speckle pattern and images (photos) taken with a 50 cycles period at maximum load. The cameras were triggered with the Fulcrum capture mode of Vic-2D using the load signal from the test machine as input. Vic-2D from Correlated Solutions was also used to analyze the images. A resolution sensitivity was run and a subset of 27 with a step size of 4 was found sufficient to capture the strain fields. The data was further exported from the software for post processing, where a resolution of 4 points per mm^2 was used which was found sufficient to match the original resolution of the step and subset size.

Some noise reduction was used on the data, employing a running average over 1000 cycles as shown on a representative strain vs cycle curve from a single data point in Fig. 5. Due to using a high resolution on the DIC images and variations in light over the testing time, some noise was present in the raw data.

2.4. Residual strain and Miner sum damage calculation

The DIC data contained strain at about 6000 points per frame (per measurement). In the following, frame is denoted i and strain as ε. Looking at only one point, the strain at frame 116 is then ε^{116}. It was assumed that the strain ε stayed near constant between two measurements. For each point and each measurement i the Miner sum was calculated using a strain based S-N curve, see Eq. 1.

$$M = \sum_{i=1}^{i} \frac{N(\varepsilon^i)}{N_{fail}(\varepsilon^i)} \tag{1}$$

$N(\varepsilon^i)$ is the number of cycles at strain ε^i; that is cycles between two measurements $i - 1$ and i at the strain ε^i measured by the DIC. $N_{fail}(\varepsilon^i)$ is the number of cycles to failure for the strain ε^i. $N_{fail}(\varepsilon^i)$ is obtained from the S-N curve describing local fiber dominated fatigue failure. How this S-N curve is obtained is described in the results section. When the Miner sum reaches 1, theoretical failure happens.

All S-N curves are given by the general double logarithmic form in Eq. 2, alternatively formulated as Eq. 2.1.

$$\log\left(N_{fail}\right) = \frac{\log\left(\hat{\varepsilon}^O\right)}{\alpha} - \frac{\log(\varepsilon)}{\alpha} \tag{2}$$

$$N_{fail} = \left(\frac{\hat{\varepsilon}^O}{\varepsilon}\right)^{\frac{1}{\alpha}} \tag{2.1}$$

In case the S-N curve has a cutoff at the static strain, typical for glass fiber reinforced composites [3,7,18,19], Eq. 3 applies.

$$\log\left(N_{fail}\right) = \begin{cases} \frac{\log\left(\hat{\varepsilon}^O\right)}{\alpha} - \frac{\log(\varepsilon)}{\alpha} & for\ \varepsilon < \hat{\varepsilon} \\ \log(1) & for\ \varepsilon \geq \hat{\varepsilon} \end{cases} \tag{3}$$

Fig. 3. Winding of the first axial layer of the pressure vessel. Rings for testing were cut from the cylindrical part.
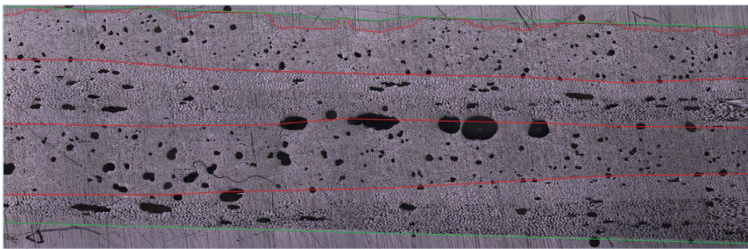

Fig. 4. Microscopy with layer borders shown in red and the bottom and top of the laminate shown in green. Many voids (black) are in the material. The outside of the vessel is in the top of picture. (Outside the green lines is potting resin holding the sample in place for polishing).
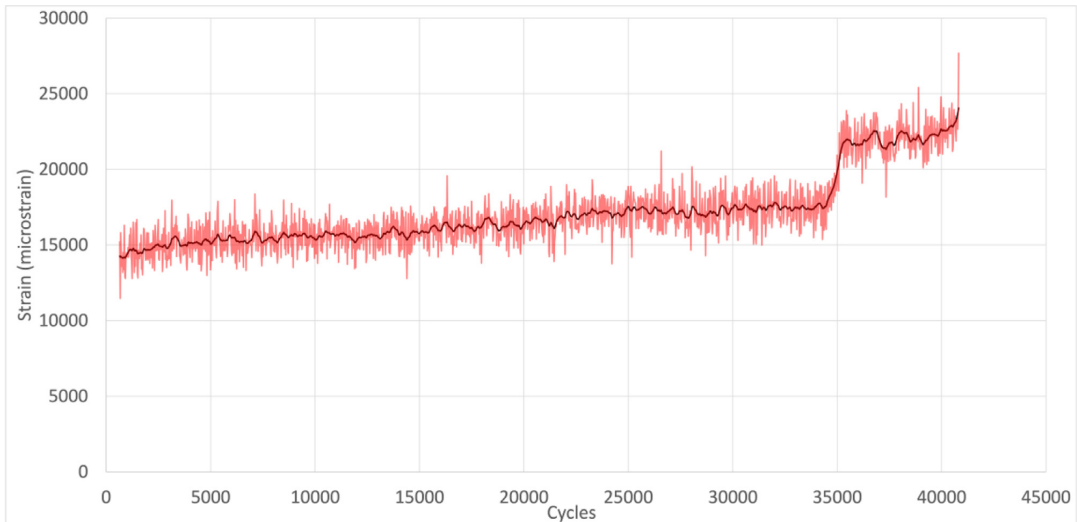

Fig. 5. Noise reduction example from a representative strain vs cycle curve of a single data point.

α describes the slope of the S-N curve, $\hat{\varepsilon}^O$ is the origin of the curve at cycle 1 and $\hat{\varepsilon}$ is the maximum static strain. If there is a cutoff, the failure cycle falls to 1 cycle as expressed by log (1) in Eq. 3.

Many studies have attempted to find composite material specific damage accumulation rules and S-N curves. Despite the effort, the same approach as for steel is still the preferred method in industry [8]. That is using the Miner damage accumulation rule and log log S-N curves. T.

P. Philippidis and V.A. Passipoularidis [20] made a review of residual strength models and compared them to experimental data. They made a short and concise conclusion that describes the state of the art well, cited here.

"The main conclusion is that the use of complicated phenomenological models requiring large experimental data sets for implementation does not necessarily pay back in terms of accurate predictions and con-
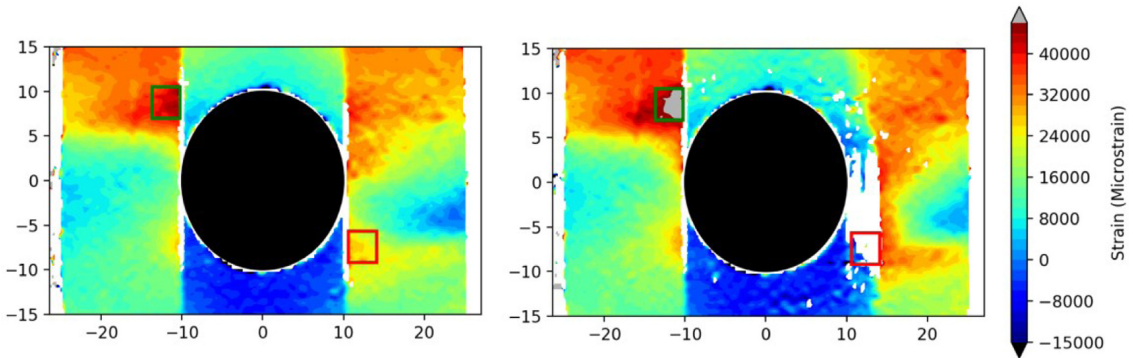
Fig. 6. Contour plots of hoop strains (vertical direction) of a static test measured by DIC in the ring specimen near the hole (black) at catastrophic failure (right) and just before (left). Failed material is shown as white. Failure initiated at the red square. The highest strain was observed in the green square.

sequently simple models requiring limited experimental effort should be preferred." Phillipidis [20].

The value of the Miner sum is often referred to as fatigue damage. However, this damage parameter has no direct physical meaning. It also does not reflect the remaining number of fatigue cycles to failure or remaining strength, because they will depend on the magnitude of the fatigue strain applied in the future. A Miner sum value of 1.0 is per definition the value for failure, however, the Miner sum may be bigger or smaller at failure depending on the scatter in fatigue properties inherent with the material. A more useful parameter is Hashin´s residual strength [21]. It calculates at which strain $\varepsilon_{residual}$ the material would fail if only one more cycle would be applied, expressed in Eq. 4.

$$\varepsilon_{residual}^i = \hat{\varepsilon}^O \left[1 - M^i\right]^\alpha = \hat{\varepsilon}^O \left[1 - \sum_{i=1}^{i} \frac{N\left(\varepsilon^i\right)}{N_{fail}\left(\varepsilon^i\right)}\right]^\alpha \qquad (4)$$

Further an exposure factor f is defined in Eq. 5 as:

$$f^i = \frac{\varepsilon^i}{\varepsilon_{residual}^i} \qquad (5)$$

If a strain ε^i is applied to a point in the sample, the exposure factor f^i describes how close the point is to failing. If f^i should exceed 1, local fiber failure would happen provided a perfect material without scatter.

3. Results

3.1. Static test results

A quasi static test was performed to obtain the static strain to failure. The contour plot of strain in the hoop direction when the ring failed and at the frame before is shown in Fig. 6. Initially the strain concentrations are at the two points described by the equator of the hole. Damage develops at these locations already at small loads as splits in the matrix along the fibers tangent to the hole. The splits are observable as white streaks tangential to the hole in the DIC contour plots in Fig. 6. Delamination and transverse matrix cracks also develop with increasing load and contribute to redistributing the initial strain field. Individual delaminations and transverse matrix cracking are, however, difficult to observe experimentally from the DIC data, as they develop inside the laminate and are only indirectly affecting the strain field. After splitting initiates, the peak strain concentration moves to the edges of the split disks from bending, indicated in green in Fig. 2. The shear splits may propagate further into the material, but due to the bending of the area between the disks, the strain concentrations do not follow the shear crack tip further. This is beneficial, keeping the peak strain within the DIC frame. It is contrary to coupon testing, where the shear split may travel with the peak strain

concentration all the way to the grips and give an invalid test. The details of the damage development are not scope of this paper, since the effect of the damage on the strain concentration is measured directly by the DIC.

A surprising result is that the highest strain of 40 000 microstrain is found near the upper left split, while failure initiated at about half that strain of 22150 microstrain at the lower right split in Fig. 2. These two areas of interest (AOI) are marked by a green and red square respectively. The load vs. strain curves for these two areas are plotted in Fig. 7, the two small circles indicate the two DIC frames in Fig. 6. The strain difference is big and is likely due to a varying distribution of imperfections, voids in particular as evident from the microscopy picture in Fig. 4. Variations in laminate thickness and delamination development are also important. Undulation of the fibers below the hoop layer may also contribute to strain changes. The strain to failure at the point where catastrophic failure initiated matches the strain to failure of 22000 to 27000 microstrain obtained from coupon tests in our laboratory The coupons were cut from flat plates made with the same constituent materials by filament winding. The measurements from conventional coupon specimen represent the lower bound of the material´s strain to failure obtained over a fairly large measurement volume (the gauge section of the coupon test). The scatter of the strength obtained from different coupon tests describes the variation of the lower bound of the material´s strain to failure. However, the strain at the other strain concentrations of the ring specimen tested here was nearly a factor two higher without causing any failure. This shows that the material can be locally much stronger than would be expected from a conventional test. Failure happens at the point where the material is locally weakened (due to voids etc.) Note: The DIC measures local strain with a resolution of about 0.5 × 0.5 mm². The strains on a microscale, e.g. around voids, may be higher, but are not detected.

3.2. S-N curve methodology

The aim of the test program was to find S-N curves that describe local fatigue failure of the fibers in the laminate. Three fatigue tests of rings with a hole were carried out. Strain fields at maximum load were measured frequently with DIC, as shown in Table 2.

While the static S specimen was analyzed in the above section, this section focuses on the fatigue specimens A – C. Contour plots of the maximum strain in hoop direction shortly before catastrophic failure are shown in Fig. 8. Regions where local fiber damage developed and accumulated are indicated by the black boxes. The black boxes are called here line slices and will be explained further down. White spots inside the line slices indicate local fiber failure. Similar to the static tests, the highest strain concentrations at failure are located at the edges of the
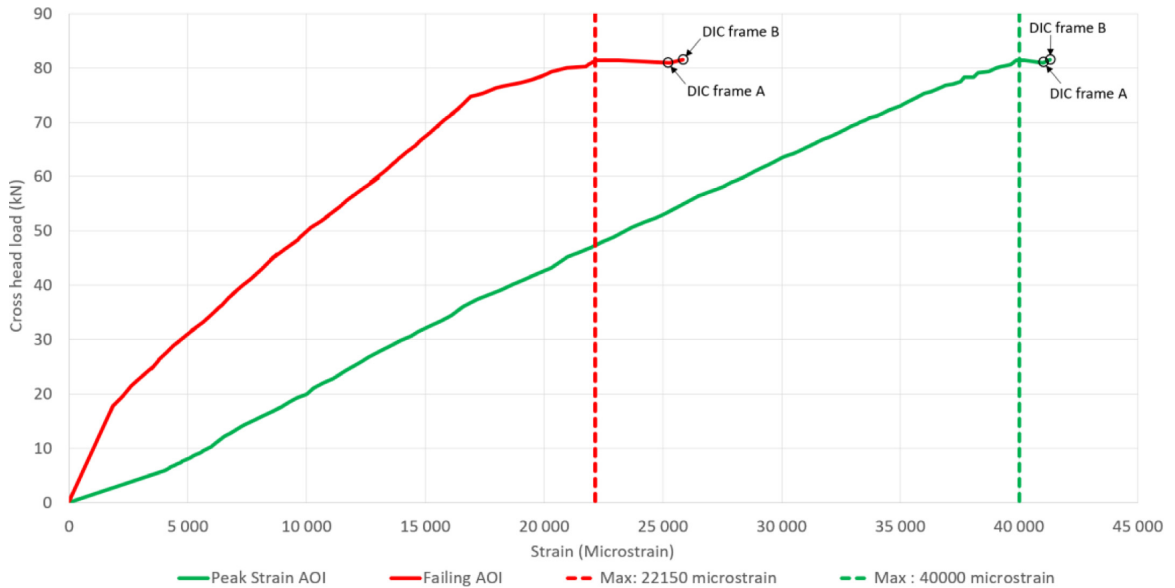
Fig. 7. Cross head load plotted against local strain curves of the ring specimen. The red and green curves represent where the specimen failed and where it had its highest strain, as indicated by the red and green squares in Fig. 6. DIC frame A and B indicate the left and right contour plot in Fig. 6.

Table 2
Failure cycle, loads and DIC frequency.

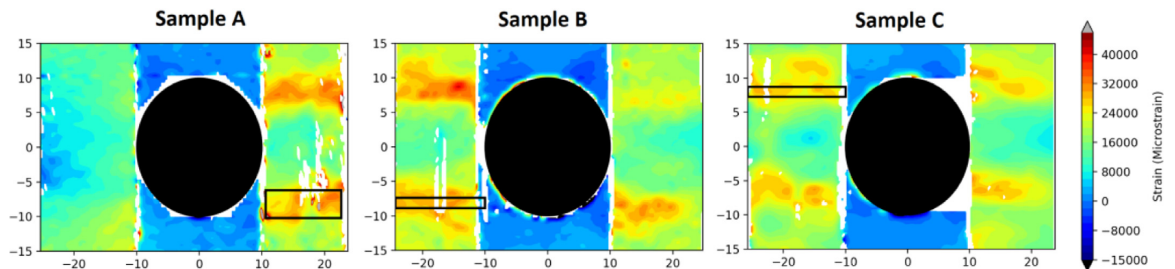| Sample	Load (kN)	Load ratio	Frequency	Failure cycle	DIC frequency
S	80.0	Started at 0.0 kN load	1 mm displacement/min	1 (Static)	1 per sec after 10 kN
A	45.0	0.1 (min load = 4.5 kN)	1 Hz	40820	1 image per 25 cycles
B	43.0	0.1 (min load = 4.3 kN)	1 Hz	65360	1 image per 25 cycles
C	40.0	0.1 (min load = 4.0 kN)	1 Hz	127768	1 image per 50 cycles

Fig. 8. Contour plot of hoop strains (vertical direction) measured by DIC in the ring specimen near the hole (black) close to fatigue failure. Failed material is shown as white. Catastrophic fiber failure initiated in the line slices (black boxes) after accumulation of local fiber failure in the line slices. Failure is shown for three specimens A, B and C failing after 40820, 65360 and 127768 cycles respectively.

split disks. There are also prominent shear cracks extending along the tangent to the hole for all specimens. Contrary to the static test however, the strain is more spread out, and the strain concentrating effect of the hole is non-existent upon failure. Fig. 9 shows the strain across the line slice in Specimen C for different numbers of cycles and shows how the strain concentration lessens and moves over time. Fig. 10 shows the contour plots at the corresponding cycles. At 364 cycles the highest strain is located close to the split that grew vertically (in load direction) out of the hole. This strain concentration moves progressively towards the edge of the specimen while also gradually lowering relative to the average strain over the line slice. Finally it ends up close to the edge of the specimen where a separate strain concentration develops and final

failure occurs. This shows that local damage developing under fatigue (matrix cracking, delamination, fiber-matrix debonding) is beneficial for reducing the strain concentrations and can cause fiber failure away from the expected point of failure. As seen in the contour plots however, the strain concentration along the equator of the hole stays close to the hole throughout the cycling. Here the mean strain is too low for matrix cracking to occur and the strain field stays relatively stable. It further highlights how matrix damage changes the load distribution between the fibers.

The aim of this paper is to find S-N curves that describe local fiber failure on the scale of about 0.25 * 0.25 mm, as typically used in modeling. Local fiber failure happens very shortly before catastrophic failure.
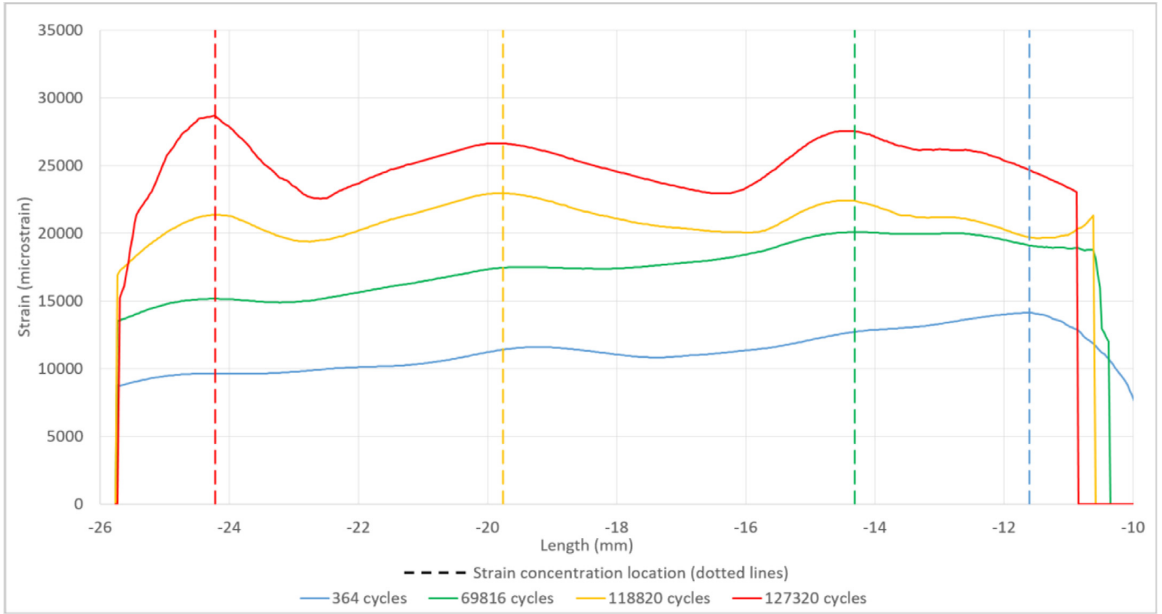
Fig. 9. Strain across the line slice on the upper left in specimen C (see Fig. 8). The edge of the hole is located at -10 on the x-axis. The highest strain moves from the edge of the hole towards the outer edge of the specimen.
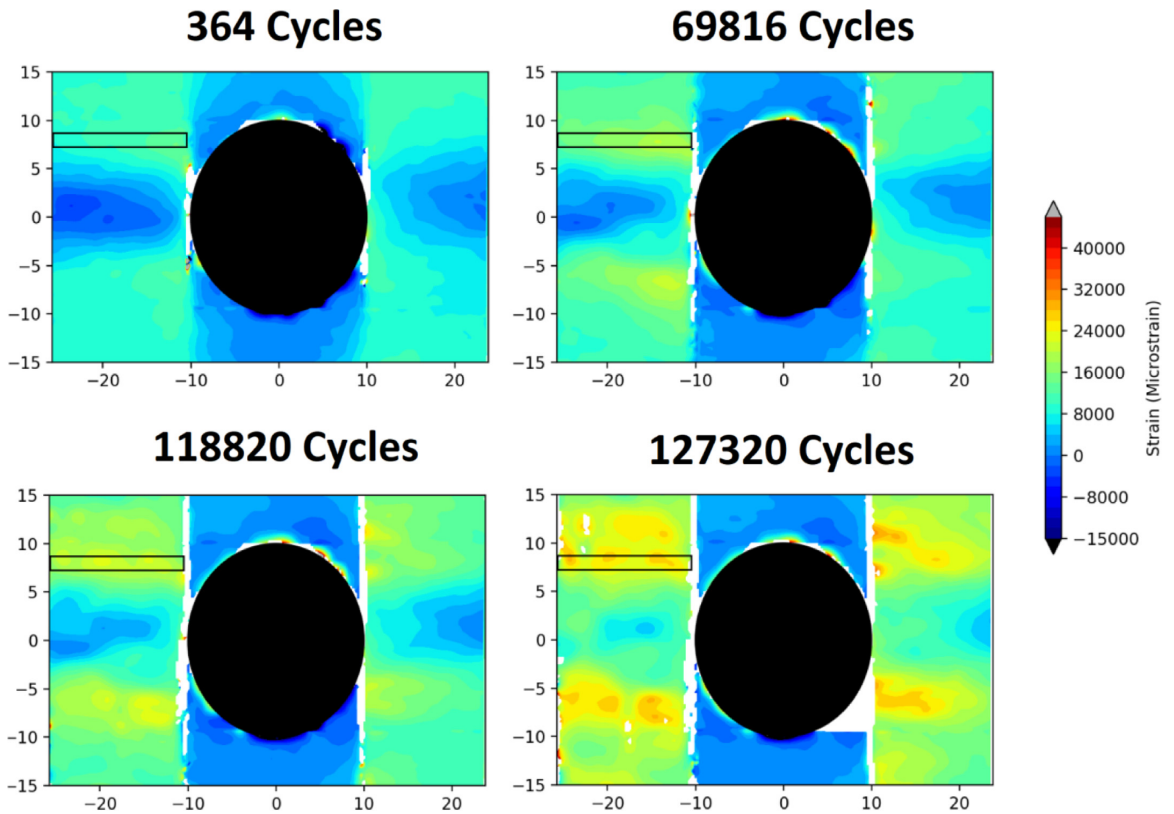

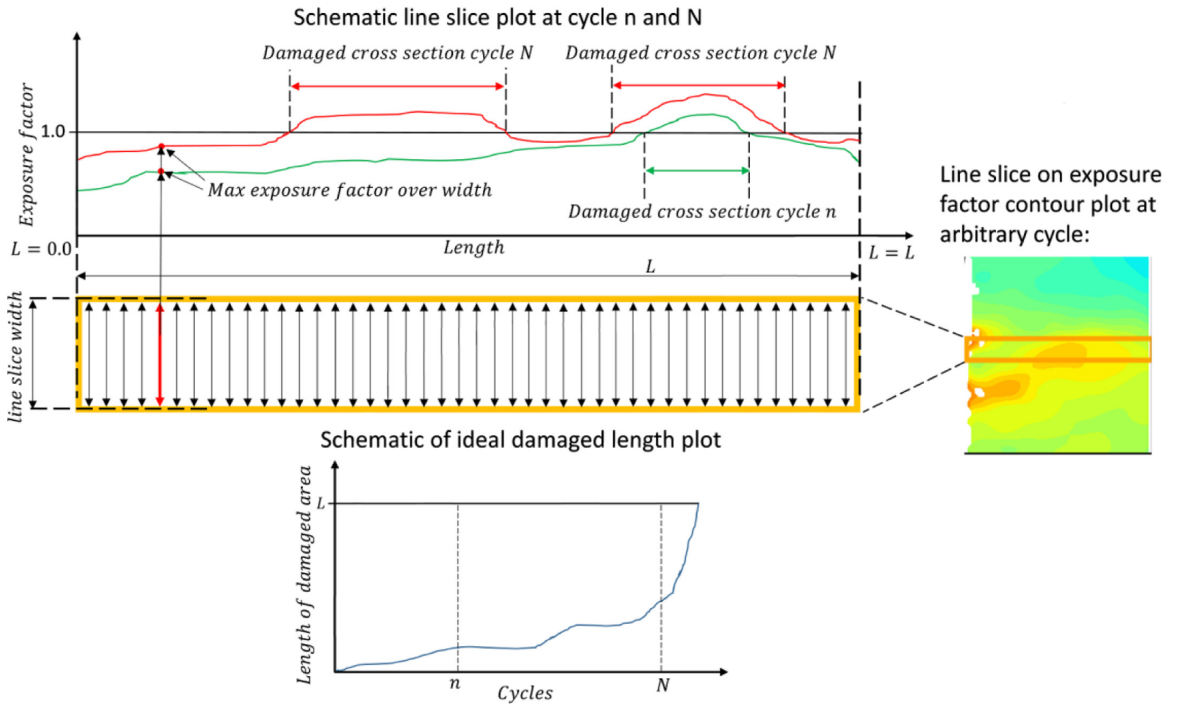**Fig. 10.** Contour plots for the four strain curves in Fig. 9.

Fig. 11. Schematic showing how damaged cross section was defined over the line slice length and how an ideal S-N curve should predict damage.
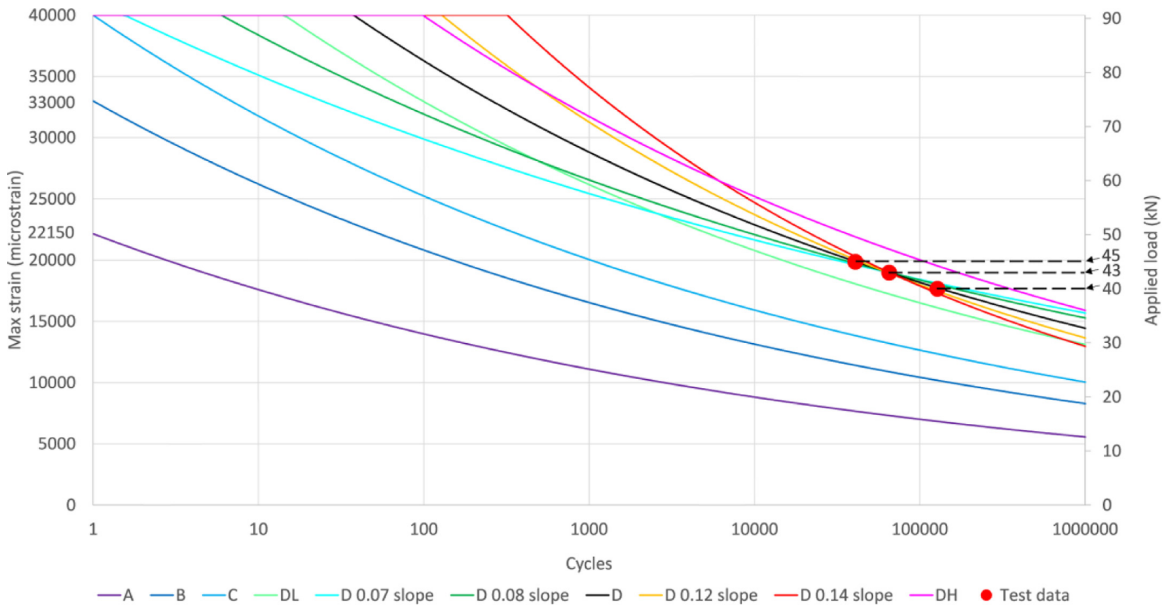

Fig. 12. Comparison of predicted catastrophic fatigue failure based on S-N curves from Table 3 and experimental results.
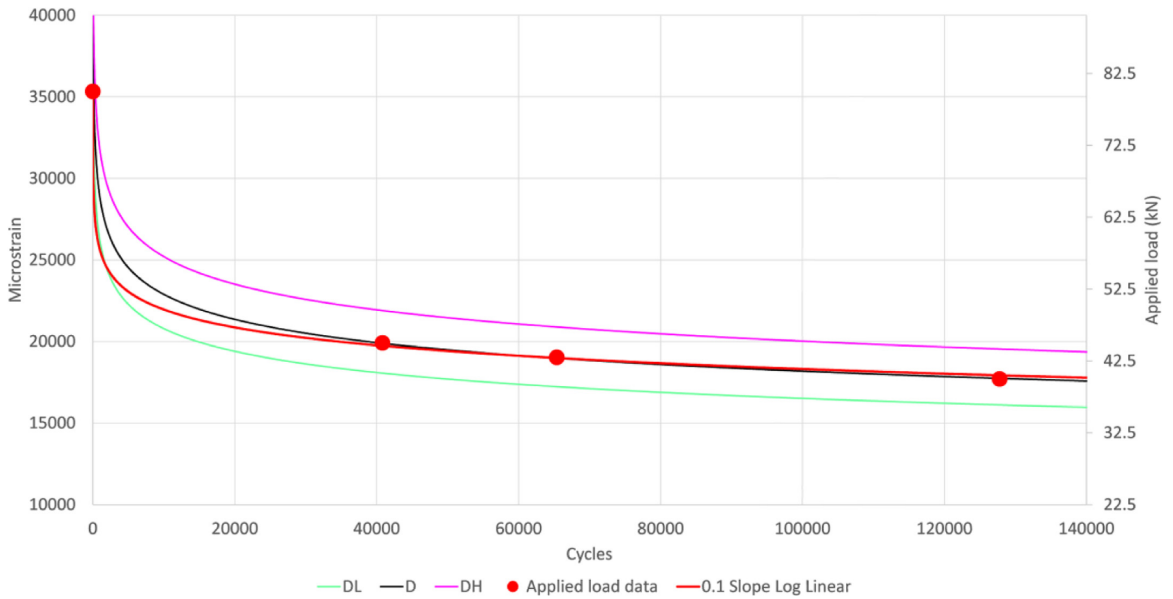
Fig. 13. Log Log plotted against Log Linear curve showing little difference at the same slope of 0.1.
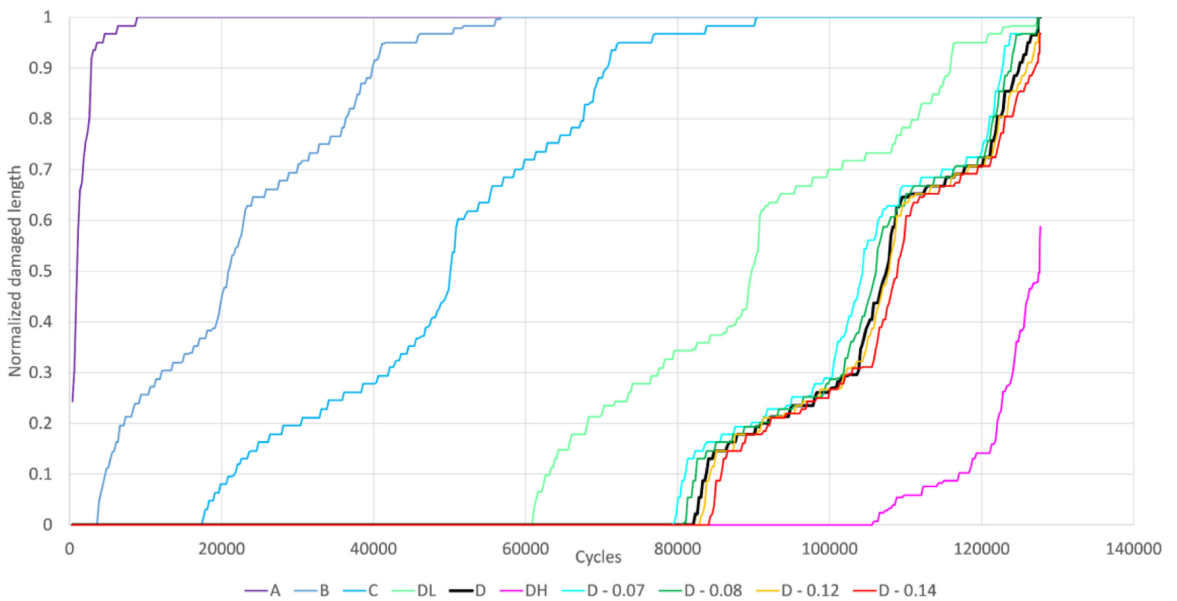

Fig. 14. Normalized damaged length for specimen C for the SN curves given in Table 3.

By measuring strains directly by DIC over the entire lifetime of the specimen the proper strains experienced by the fibers at every point (within the resolution of the DIC system) throughout the specimen are measured directly. The reasons for the changes of the strain do not need to be known, which is an advantage of using DIC.

S-N curves are normally found by regression of stress or strain vs. cycles to failure data from coupon testing. The standard coupon sample has an even strain field and will fail at the weakest point, as described for the static results. This approach is sound for conservative design es-

timates in the industry, but it falls short of giving the full picture of the material´s behavior in the presence of strain concentrations as needed in numerical models for describing damage development. Understanding the behavior of components with strain concentrations requires knowledge of the local properties throughout the specimen, not just the weakest spot in a larger volume obtained from coupon tests.

Fatigue testing a specimen with a hole and using DIC measurements allows measuring the local strains vs. number of cycles at many points of the test specimen. If the strain field would not change, local S-N curves
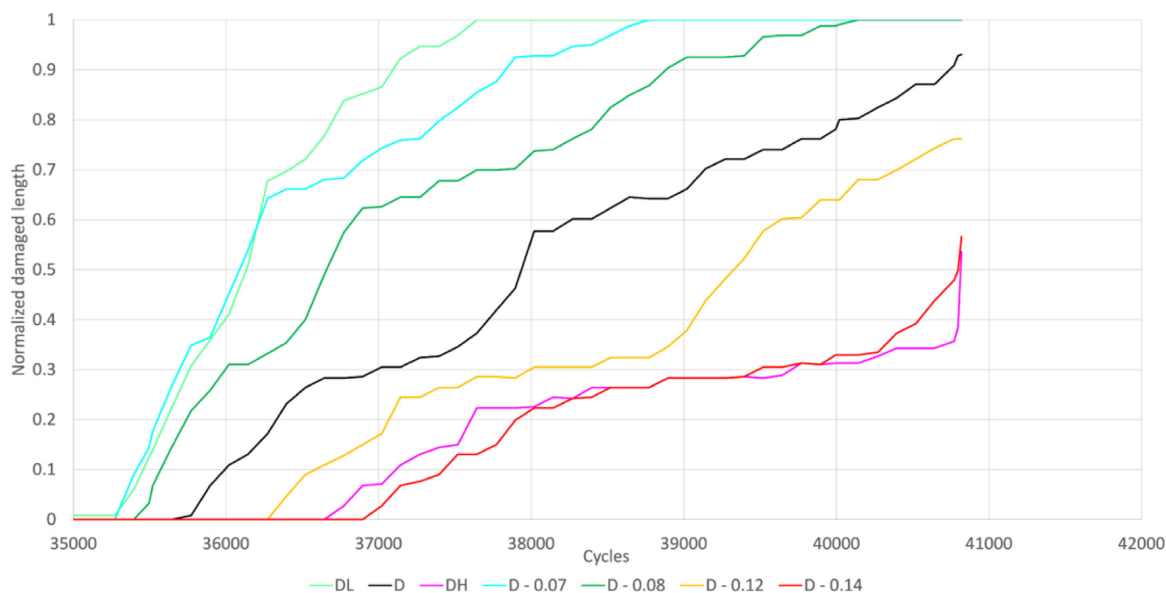
Fig. 15. Normalized damaged length for sample A for the SN curves given in Table 3.

could be obtained by just measuring local strains vs. number of cycles to local failure. However, as shown in Fig. 9 and Fig. 10, local strains change with increasing number of cycles, prohibiting the direct measurement of S-N curves at local points. This necessitates an approach for obtaining S-N curves that can take into account varying strains over time.

In this study the varying strains are handled by calculating the Miner sum from the local cyclic strains measured by DIC and an assumed S-N curve. The Miner sum is calculated and updated after every DIC measurement interval. It is assumed that the strain is constant within a measurement interval, which should be a reasonable assumption considering the large number of measurements. This approach is equivalent to how fatigue damage may be handled in existing models, numerical and analytical. However, numerical models have to adopt a cycle jump approach that assumes and estimates damage over a large range of cycles [22]; simulating each cycle is too numerically expensive. By instead calculating the Miner damage on the actual strains in the specimen from high frequency DIC, a more accurate evaluation of the S-N curve and damage rule emerges with a lot less assumptions than in an equivalent numerical model.

Since first local fiber failure and catastrophic failure happened within a short cycle span, around 500 cycles for all tests, the proper S-N curve should also predict catastrophic failure. Catastrophic failure is here assumed to happen when the whole length of the line slices have a Miner sum/exposure factor over 1.0. Looking at where the line slices are located, this means that the whole cross section on one side of the hole has theoretically failed. This choice is further supported by the even strain fields in Fig. 9 and the fact that fiber failure occurred away from the hole.

To evaluate the choice of different S-N curves for properly describing fatigue damage and catastrophic failure with the Miner sum approach, the length of local theoretical fiber damage along a line slice was determined, as explained in Fig. 11. For each point along the length of the line slice at each cycle, the algorithm searches over the width of the line slice for an exposure factor above 1.0. If it finds this, the length point along the line slice is set as damaged. For the ideal S-N curve, the damaged length should be equal to the line slice length upon catastrophic

Table 3
S-N curve parameters.

Name	Parameters		
	Origin (microstrain)	Slope	Cut-off (microstrain)
A	22150	0.1	22150
B	33000	0.1	33000
C	40000	0.1	40000
DL	52222	0.1	40000
D	57500	0.1	40000
D – 0.07	41254	0.07	40000
D – 0.08	46141	0.08	40000
D – 0.12	71643	0.12	40000
D – 0.14	89719	0.14	40000
DH	63312	0.1	40000

failure. Any curve that predicts a damaged length over the whole line slice before failure is conservative.

The presented method assumes that once a local point has a miner sum/exposure factor over 1.0, local fiber failure may happen at this point. When a whole cross section has a Miner sum/exposure factor over 1.0 fiber failure may progress over the cross section and initiate catastrophic failure.

3.3. Evaluating different S-N curves

In order to find a suitable S-N curve that can predict failure of the test specimen, the S-N curves listed in Table 3 were investigated. Note, cyclic fatigue strains are given as maximum strains, not amplitude strain. A traditional S-N curve has two variables; origin and slope. In case the origin is higher than the static strain to failure, a cutoff at the failure strain is necessary, as described in Eq. 3. Cutoffs are common for glass fiber composite material systems [7]. The S-N curves are also shown in Fig. 12.

The S-N curve "A" represents a typical S-N curve obtained from coupon testing. The static strain to failure of 22150 microstrain from coupon lab testing is used as the origin and the slope of the curve is 0.1, as typically found for glass fiber laminates [3,18,23–28]. The slope of
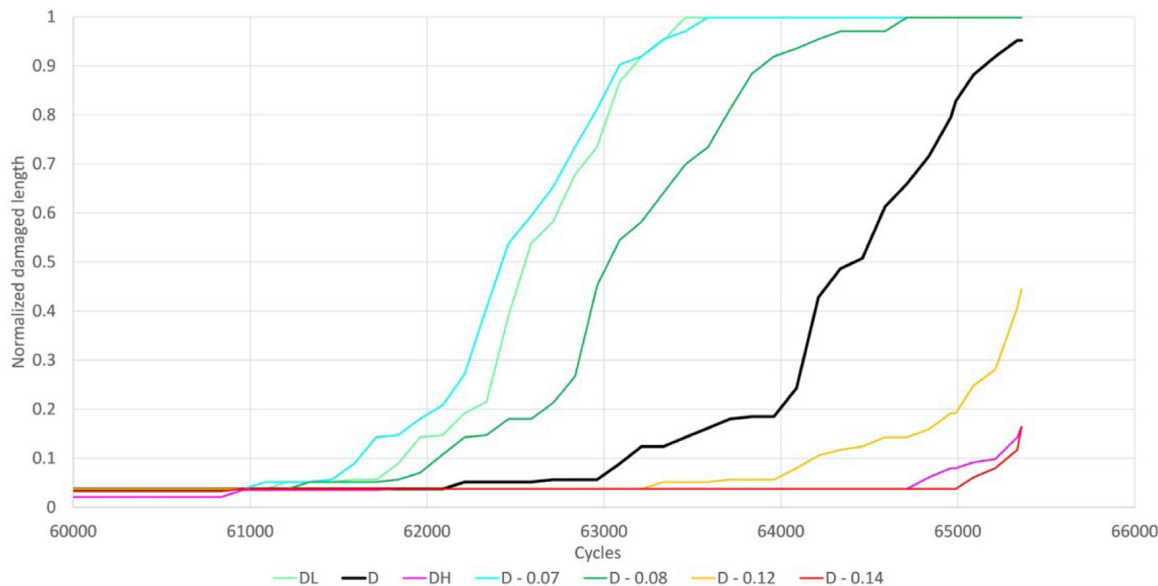
Fig. 16. Normalized damaged length for sample B for the SN curves given in Table 3.

Table 4
Summary of the different S-N curves damage prediction at the failure cycle.

S-N Curve	Specimen A		Specimen B		Specimen C	
	Damaged length	At cycle fraction	Damaged length	At cycle fraction	Damaged length	At cycle fraction
A	1.00	0.02	1.00	0.56	1.00	0.07
B	1.00	0.21	1.00	0.93	1.00	0.44
C	1.00	0.60	1.00	0.94	1.00	0.71
DL	1.00	0.92	1.00	0.97	1.00	0.99
D	0.93	-	0.95	-	1.00	0.99
D −0.07	1.00	0.95	1.00	0.97	1.00	0.99
D − 0.08	1.00	0.98	1.00	0.99	1.00	0.99
D − 0.12	0.76	-	0.44	-	0.97	-
D − 0.14	0.57	-	0.16	-	0.97	-
DH	0.54	-	0.16	-	0.59	-

the S-N curve for local failure should arguably be the same as for failure in larger volumes from a coupon test. This approach has also been applied by other studies investigating local properties (Eliopoulos & P. Philippidis, 2011). This investigation tested only three fatigue samples, which is not enough to establish the slope of the global S-N curve reliably, but it is sufficient to show the concept of obtaining S-N curves for local fiber failure. However, for the three tests, the typically used slope of 0.1 was found as the best regression fit based on the load vs. cycle data, as plotted on the second axis in Fig. 12. Most studies ([3,18,23–27]; Eliopoulos & P. Philippidis, 2011; [29]) use a log linear formulation for the S-N curves with a slope of 0.1, but the difference compared to a log-log S-N curve is small as shown in Fig. 13. A log linear formulation could have been used, but the best experimental fit was found with the log-log presentation in this study.

Fig. 14 shows the damaged length vs. number of cycles in the line slice for specimen C. The S-N curve "A" predicts that the entire length has failed after about 1000 cycles, while the real catastrophic failure happened at 127768 cycles. The traditional S-N curve as typically measured from coupon tests would predict a far too short lifetime. Predictions of the lifetime for samples A and B were also much too short. Fig. 15 and Fig. 16 shows the damaged length for samples A and B and Table 4 summarize the results.

The same analysis was done for the other S-N curves. These curves were shifted up relative to the "A" curve with the origin at 33000, 40000 and 52222, 57500 and 63312 microstrain respectively. All curves with an intercept higher than 40000 microstrain have the designation "D". DL and DH represents a low and high S-N curve while "D" curves with a designated number have a slope variation. The slope variation curve were scaled according to best fit around the applied load data assuming the D curve and the applied load data coalesced. This can be seen in Fig. 12 as the D curve and the best fit to the applied load data coalesce at all cycles after the cutoff cycle of the applied load curve. The cutoff is different for the applied load curve and the D curve and therefore the axis for the applied load data is shifted to above the maximum static load. Note, a cutoff was applied as given in Eq. 3, because the static strain to failure for the strongest part of the material cannot be exceeded.

It can be seen from Table 5 and Fig. 14 - Fig. 16 that S-N curves "B", "C" and "DL" gave too extensive damage predictions for all specimen. Curve "D" (with a slope of 0.1) gave damage predictions very close to the entire cross section and DH gave a damaged length short of the cross section. The "At cycle fraction" column tells at what fraction of the catastrophic failure cycle in Table 2 the S-N curve predicted failure across the whole line slice.
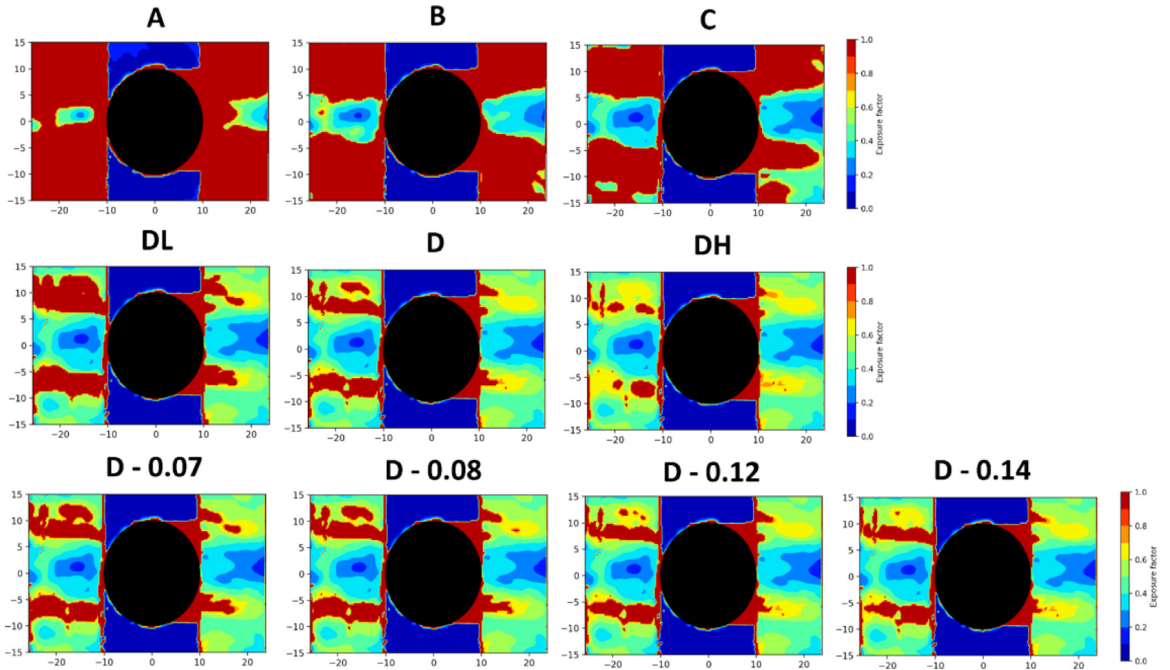
Fig. 17. Contour plots of exposure factor at catastrophic failure over sample C for all tested S-N curves.
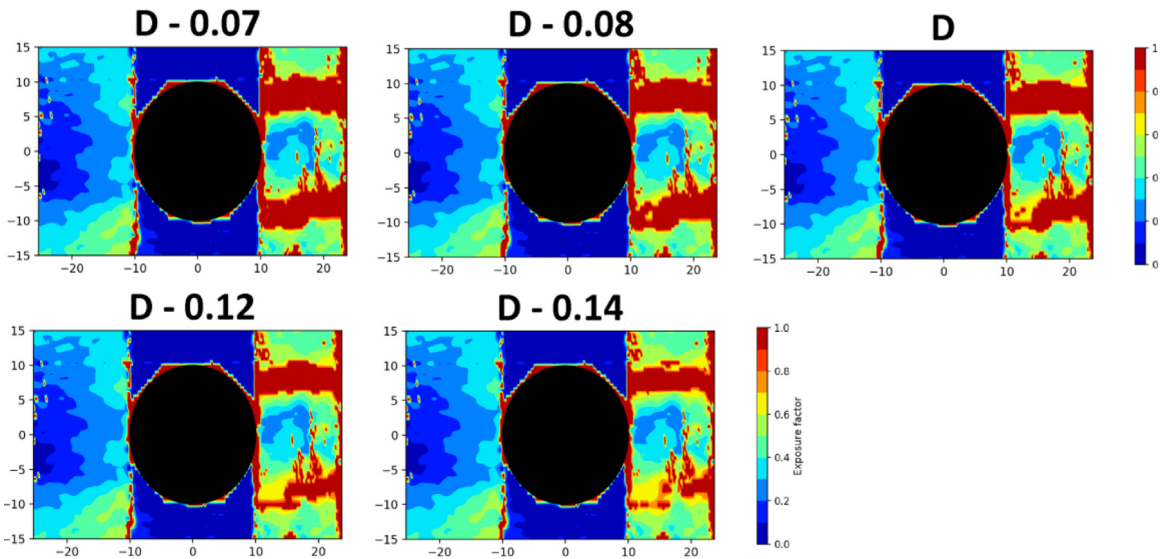

Fig. 18. Contour plots of exposure factor at catastrophic failure for slope sensitivity S-N curves for sample A.

To check the sensitivity of the results to the slope, the slope of the "D" curve was changed from 0.07 to 0.14 as shown in Table 4. It can be seen that the C specimen´s damage is not affected by the slope sensitivity, while A and B is to a great extent. This is due to that A and B have higher strains and a shorter cycle span where fatigue damage occurs. Looking at the S-N curves in Fig. 12 it can be seen that it is particularly for the low cycle regime where the slope variation shows the biggest

differences. It is however remarkable that the D-curve's slope of 0.1 gives the most consistent damage prediction, in line with the slope found from literature and from the global load test data.

The difference in damage development between specimen A, B and C is due to a less sudden failure of the bottom hoop layer for Specimen C, giving a slower transfer of force from the bottom to the top hoop layer compared to A and B. It is evidently not possible to monitor the bottom
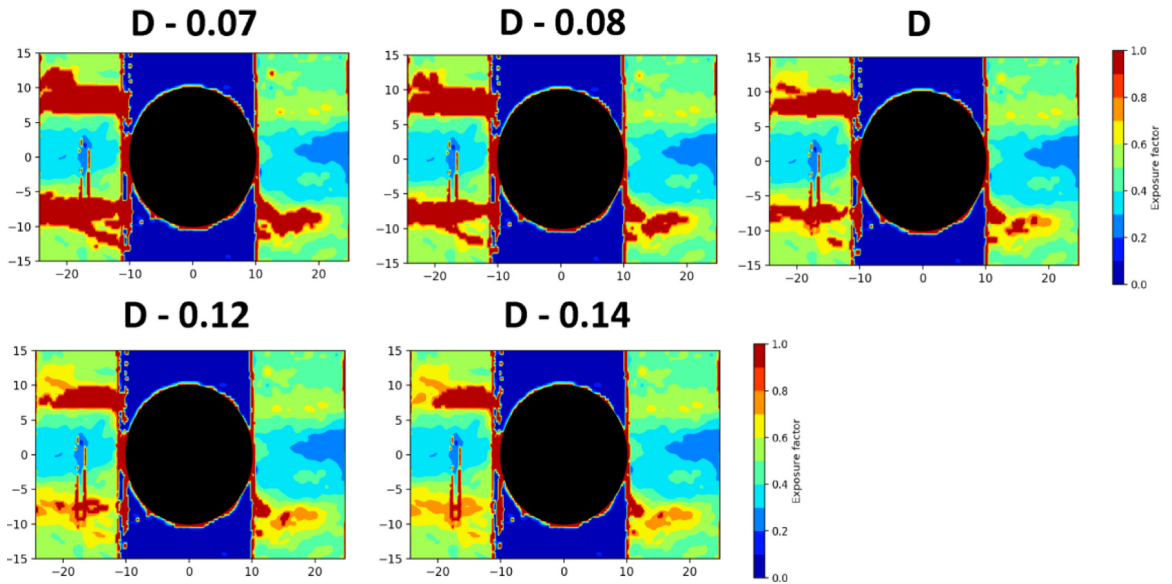
Fig. 19. Contour plots of exposure factor at catastrophic failure for slope sensitivity S-N curves for sample B.
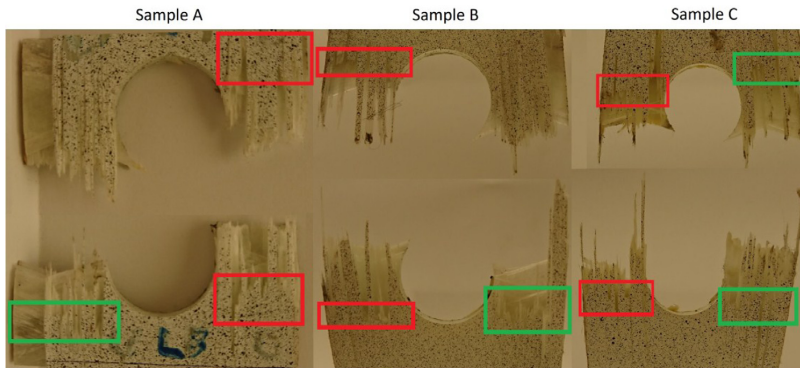

Fig. 20. Photos of the catastrophic fracture of the three samples. The main initial fracture surfaces are outlined in red squares. Further damage resulted from pulling the specimen apart and are highlighted in green.

hoop layer by any practical means, but it was observed visually that this layer failed more gradually for Specimen C.

Applying the exposure factor from Eq. 5.0 it can be shown how close the fibers are to failure theoretically. The exposure factor will change depending on the S-N curve used for calculating the Miner sum. Fig. 17, Fig. 18 and Fig. 19 show the contour plots of exposure factors for samples C, A and B respectively just before catastrophic failure. Exposure factors for specimen C are given for all S-N curves. Specimens A and B show only exposure factors for the slope sensitivity S-N curves.

Comparing the results with Fig. 19, where the experimental catastrophic failure is shown allows evaluation whether the predicted accumulated local fiber damage from the chosen S-N curves corresponds to the experimental failure.

Using the S-N curves "A", "B" and "C" in the exposure factor calculations overestimates damage; almost the whole sample is red, also reflected in the failed length graph in Fig. 14 - Fig. 16. This is further confirmation that these S-N curves are not suitable to predict local fiber failure. The damage calculated for the D curves are all reasonable. All show local fracture across the width on one side of the hole and most damage where the sample actually failed. Evident by looking at the time

history expressed in the failed length graphs, the D curve (with a slope of 0.1) gives the most consistent damage prediction across specimens. Variations of the slope around 0.1 can be seen to give less consistent damaged length prediction. The ability of predicting the progression of fiber failure is as important as identifying initial location of damage. The D curve can be seen to predict red areas in the contour plots also where the green squares are located in Fig. 20 for the C and B samples. For the A sample, the exposure factor is highest on the side of the hole where the damage progressed (bottom left).

Since the "A" curve is representative for an S-N curve obtained from coupon data for the material, it can be seen that such a curve would largely overestimate the local fiber damage development in the sample. When attempting to model fatigue damage growth numerically, using the right local fatigue properties will be critical for the success of such models. The method described here allow obtaining such local S-N curves for fiber failure in a still conservative way and highlights how standard coupon test S-N curves may be insufficient for describing local damage development.

Knowing the local S-N curves for fiber failure may also allow using the DIC measurements as a Non Destructive Evaluation NDE method.

If the strain field under a known load can be measured periodically, the fatigue lifetime calculations can be made as described here. Which areas are most likely to develop fiber failure can be predicted in a real component. This would also allow estimating the remaining number of cycles to failure.

4. Conclusions

Ring specimens cut from the cylindrical part of GFRP filament wound pressure vessels worked well for characterizing local fiber dominated fatigue failure around a strain concentration created by a hole. The split disk setup offers a simple alternative to pressure testing of the vessels. Changes of the strain concentrations were measured with Digital Image Correlation (DIC), allowing measurement of the entire strain field around the hole for increasing number of fatigue cycles. Production defects such as voids and thickness variation and possible undulation of fibers caused considerable local variations in the strain field that could be identified by the DIC method. However, the reasons for the changes of the strain do not need to be known. The DIC always measures the proper actual strain that causes local fatigue failure on the surface.

The maximum local static strain to failure found through DIC monitoring of static tests was found to be about two times larger than the weakest spot, a much larger variation in properties than would be expected from traditional coupon testing.

The DIC measurements showed that the strain concentrations get significantly reduced compared to the static strain field with increasing number of cycles. The reduction in strain concentrations was attributed to various forms of matrix damage developing during cycling of the specimen.

S-N curves describing local fiber damage could be found by comparing predicted Miner sum fatigue damage based on the DIC strain data and experimentally found failures. Accumulation of local fiber damage across the width of the specimen between hole and edge could be identified as the condition for catastrophic failure, i.e. the specimen breaking into two parts.

The slope of the S-N curve describing local fiber damage was the same as typical slopes for glass fiber laminates obtained from coupon specimens. However, more experimental ring test results would be needed to confirm this.

The origin of the S-N curve describing local fiber damage is significantly higher (more than a factor 2) than would be expected from standard coupon data used to characterize catastrophic failure. This means that local fatigue properties need to be properly accounted for in any characterization of the development of fatigue damage in the presence of strain concentrations.

Declaration of Competing Interest

We have no conflicts of interest to disclose.

Acknowledgements

References

[1] J.P. Berro Ramirez, D. Halm, J.-C. Grandidier, S. Villalonga, A fixed directions damage model for composite materials dedicated to hyperbaric type IV hydrogen storage vessel – Part I: Model formulation and identification, Int. J. Hydrogen Energy 40 (38) (2015) 13165–13173.

[2] T. Flatscher, H.E. Pettermann, A constitutive model for fiber-reinforced polymer plies accounting for plasticity and brittle damage including softening – Implementation for implicit FEM, Compos. Struct. 93 (9) (2011) 2241–2249.

[3] T. Ramesh, Fatigue of Composite Materials, in: H. Altenbach, W. Becker (Eds.), Modern Trends in Composite Laminates Mechanics Modern Trends in Composite Laminates Mechanics, Vienna, International Centre for Mechanical Sciences (Courses and Lectures)Springer, 2003 vol 448.

[4] ASTMASTM Standard D3039/D3039M - 17 Standard Test Method for Tensile Properties of Polymer Matrix Composite Materials, ASTM, 2017.

[5] S. Giancane, F.W. Panella, R. Nobile, R. Dattoma, Fatigue damage evolution of fiber reinforced composites with digital image correlation analysis, Procedia Eng. 2 (1) (2010) 1307–1315.

[6] W.R. Broughton, M.R.L. Gower, M.J. Lodeiro, G.D. Pilkington, M.R. Shaw, An experimental assessment of open-hole tension–tension fatigue behaviour of GFRP laminate, Compos. Part A: Appl. Sci. Manuf. 42 (10) (2011) 1310–1320.

[7] R. Talreja, W. Watt, Fatigue of composite materials: damage mechanisms and fatigue-life diagrams, Proc. R. Soc. A 378 (1981) 461–475.

[8] DNV GL, DNVGL-ST-C501 Composite Components, DNV GL, Høvik, 2017.

[9] H. Wang, W. Zhang, F. Sun, W. Zhang, A comparison study of machine learning based algorithms for fatigue crack growth calculation, Materials 10 (5) (2017).

[10] J.A. Rodriguez, Y. El-Hamzaoui, J.A. Hernandez, J.C. Garcia, J.E. Flores, A.L. Tejeda, The use of artificial neural network (ANN) for modeling the useful life of the failure assessment in blades of steam turbines, Eng. Fail. Anal. 35 (2013) 562–575.

[11] J. Mohanty, B. Verma, D. Parhi, P. Ray, Application of artificial neural network for predicting fatigue crack propagation life of aluminum alloys, Arch. Comput. Mater. Sci. Surf. Eng. 1 (3) (2009) 133–138.

[12] P. Giovanni, Numerical and Experimental Investigation of Impact Behaviour of GFRP Composiites, NTNU - Norwegian University of Science and Technology, Trondheim, 2014 (PhD thesis).

[13] M.A. Sutton, J.H. Yan, V. Tiwari, H.W. Schreier, J.J. Orteu, The effect of out-of-plane motion on 2D and 3D digital image correlation measurements, Opt. Lasers Eng. 46 (10) (2008) 746–757.

[14] S.H. Yoon, W.M. Cho, C.G. Kim, Measuremet of modulus in filament wound ring specimen using split disk test, Exp. Techn. 21 (1) (1997) 25–28.

[15] Binani and 3B, HiPertex W2020 datasheet, Binani and 3B (2015).

[16] Momentive, Technical Datasheet Epikote Resin MGS RIMR 135 and Epikure Curing Agent MGS RIMH 134 - RIMH, 2006 137, Momentive.

[17] A.E. Kraukalis, A.I. Gagani, A.T. Echtermeyer, Hygrothermal aging of amine epoxy: reversible static and fatigue properties, Open Eng. 8 (2018) 447–454.

[18] J.F. Mandell, D.D. Huang, F.J. McGarry, Fatigue of glass and carbon fiber reinforced engineering thermoplastics, Polymer Compos. 2 (3) (1981) 137–144.

[19] J.F. Mandell, D.D. Samborsky, DOE/MSU Composite Material Fatigue Database: Test Methods, Materials and Analysis, Montana State University, Montana, 1998.

[20] T.P. Philippidis, V.A. Passipoularidis, Residual strength after fatigue in composites: Theory vs. experiment, Int. J. Fatigue 29 (12) (2007) 2104–2116.

[21] Z. Hashin, Cumulative damage theory for composite materials: Residual life and residual strength methods, Compos. Sci. Technol. 23 (1) (1985) 1–19.

[22] A.T. Travesa, Simulation of Delamination in Composites Under Quasi-Static and Fatigue Loading Using Cohesive Zone Models, University of Girona, Girona, 2006.

[23] Z. Zhang, G. Hartwig, Relation of damping and fatigue damage of unidirectional fibre composites, Int. J. Fatigue 24 (2002) 713–718.

[24] P.T. Curtis, Tensile fatigue mechanisms in unidirectional polymer matrix composite materials, Int. J. Fatigue 13 (5) (1991) 377–382.

[25] V.M. Harik, J.R. Klinger, T.A. Bogetti, Low-cycle fatigue of unidirectional composites, Int. J. Fatigue 24 (2002) 455–462.

[26] L.J. Broutman, S. Sahu, A new theory to predict cumulative fatigue damage in fiberglass reinforced plastics, Compos. Mater. Test. Des. (Second Conference) (1972) 170–188 vol. ASTM STP 497.

[27] M.J. Owen, P.T. Bishop, Fatigue properties of glass-reinforced plastics containing a stress concentrator, J. Phys. D: Appl. Phys. 6 (1973) 2057–2069.

[28] E.N. Eliopoulos, T.P. Philippidis, A progressive damage simulation algorithm for GFRP composites under cyclic loading. Part I: Material constitutive model, Compos. Sci. Technol. 71 (5) (2011) 742–749.

[29] Z. Fawaz, F. Ellyin, Fatigue failure model for fibre-reinforced materials under general loading conditions, J. Compos. Mater. 28 (15) (1994) 1432–1451.

Paper III

Article

Progressive Fatigue Failure Analysis of a Filament Wound Ring Specimen with a Hole

Eivind Hugaas *, Nils Petter Vedvik and Andreas T. Echtermeyer (ORCID)

Department of Mechanical and Industrial Engineering, Norwegian University of Science and Technology, 7034 Trondheim, Norway; nils.p.vedvik@ntnu.no (N.P.V.); andreas.echtermeyer@ntnu.no (A.T.E.)
* Correspondence: eivind.hugaas@ntnu.no

Abstract: A progressive FEA mechanical fatigue degradation model for composites was developed and implemented using a UMAT user material subroutine in Abaqus. Numerical results were compared to experimental strain field data from high frequency digital image correlation (DIC) of split disk fatigue testing of pressure vessel cut outs with holes. The model correctly predicted the onset and evolution of damage in the matrix as well as the onset of fiber failure. The model uses progressive failure analysis based on the maximum strain failure criterion, the cycle jump method, and Miner's sum damage accumulation rule. A parameter study on matrix properties was needed to capture the scatter in strain fields observed experimentally by DIC. S-N curve for the matrix material had to be lowered by 0% to 60% to capture the experimental scatter. The onset of local fiber failure had to be described by local S-N curves measured by DIC having 2.5 times greater strain than that of S-N curves found from standard coupon testing.

Keywords: finite element analysis; material models; fatigue; filament winding; digital image correlation

1. Introduction

There is an urgent need for composite pressure vessels that can safely and economically transport hydrogen at 700 bar [1,2]. The technology and design standards exist; however, cost is high due to very strict testing and acceptance requirements [3–5] even at lower pressures. For the acceptance tests, a perfect structure is assumed. However, during a vessel's lifetime, small damages such as a minor impact damage may occur from use. It is currently an unknown how much damage can be tolerated in the vessels due to unknown mechanical fatigue resistance. Damaged vessels are replaced by new ones, which is very costly, especially for large vessels.

Today's pressure vessels have a static strength exceeding the design pressure of 700 bar by a factor of about 2.5 or more as required by the design standards. The factor was also identified by Berro et al. in the OSIRHYS IV project [6]. Uncertainties of the effect of the presence of damage are largely related to mechanical fatigue. Numerical analysis in combination with well-chosen experimental data are the key to better understand how damage and fatigue may affect the mechanical performance and strength [6]. In turn, better numerical models may answer how much wear and damage can be tolerated on in use vessels, avoiding early and costly decommissioning as well as reducing costly testing requirements of new designs

Mechanical fatigue in composites causes complex progressive damage development that sets it apart from more conventional materials such as steel. Progressive failure or damage is defined as damage in the material that occurs over a defined time span. In a tensile test the time span is the loading time and progressive failure in the material typically occurs towards the end of that time span just before the specimen fails. In a fatigue test of a metal, the progressive damage will typically occur towards the very last few cycles as a crack is initiated and propagates. In a composite, however, progressive fatigue damage

looks rather different from a metal. Instead of damage and crack propagation occurring over a very short cycle span towards end of life, mechanical fatigue damage in composites occurs steadily over the whole lifetime, gradually changing the structural behavior and redistributing loads [7]. The dominating mechanism for changing strain fields under fatigue is the development of matrix cracking over time [8–10]. Matrix cracking/matrix damage is seen here in its widest meaning, including cracks in the polymer part of the composite, delamination, and fiber-matrix debonding. Developing matrix cracks change how forces are distributed between the load bearing fibers and cause the strain fields to change. Initiation and propagation of the various forms of matrix cracks is a complex phenomenon.

Traditionally, fatigue of composites has been divided into two segments, high cycle fatigue (HCF) and low cycle fatigue (LCF). The domains of the two are defined by the failure mechanism which dominates in the final rupture of the material in question. HCF is dominated by matrix damage, while LCF by fiber failure [8,11–13]. Notably, a relatively large volume of the material is characterized using this traditional approach. The volume is the typical size of the gauge section of a test specimen of roughly 1000 mm^3. In this study, as will be explained later, fatigue is described locally around a fiber bundle, addressing a volume on the scale of a typical element in a FEA, which can be 0.2 mm^3 or less. When developing a finite element model to describe such local fatigue damage in a component, some highly stressed material (near a defect or geometric stress concentrator) may fail after few cycles as "low cycle fatigue", while material in the lower stressed regions may be in the "high cycle fatigue" domain. As such, a component that catastrophically fails after many cycles fails globally in the HCF domain, but it may have local material that also fails in the LCF domain. A FEA material model addressing local fatigue failure has to take local low and high cycle fatigue into account.

High and low cycle fatigue is, however, defined for the composite material, while the FEA model in this study considers fibers and matrix by themselves, though with some interaction effects. Since the matrix is much weaker and traditionally degrades faster due to fatigue than the fiber (higher slope of the S-N curve [14]), local matrix degradation will naturally dominate in the global high cycle fatigue range. Local fiber failure will be prevalent in the low cycle fatigue range. This study focuses on modeling a global high cycle fatigue experiment.

When using finite element models to model matrix cracking, both initiation and propagation needs to be predicted, including the propagation direction. Recent developments in such models have managed to satisfactorily predict matrix damage dominated fatigue damage propagation in laboratory test specimen having simple geometries and known direction of crack propagation, e.g., Turon [7] and Nixon et al. [15] based on the method suggested by Harper et al. [16]. Attempts to simplify the matrix crack growth by smearing matrix cracking over a larger region and modeling it by plastic behavior were reported for the static case by NASA [17], Flatscher et al. [18], and Gagani et al. [19]. It is, however, difficult to tell whether the plasticity approach matches experiments only for the particular geometry of the specimen investigated or whether it is a general way to model the material. For the static case, Rozylo [20] satisfactorily managed to model crack propagation without predefined crack directions using the cohesive zone modelling approach in combination with a user element subroutine (UEL) with promising results. Still, all of the above-mentioned models are relatively academic and not easy for the average design engineer to implement or to get the correct input data for. The models have been developed with lab experiments in mind and not real designs. In this study, the model was developed with the design engineer in mind and then tested on a complex lab experiment. This study therefore has a somewhat different format than most academic publications covering the topic, having a wider scope and less in detail investigations of the experimental results and modelling. This study would however not have been possible without the past academic literature going in depth in DIC and Abaqus in particular.

There are currently some commercial composite mechanical fatigue numerical frameworks available, most notably FEMFAT [21] and Fe-safe [22]. While the models offer simple

and fast fatigue evaluations, they do not include progressive damage and do fatigue analysis based on a static solution. The models are only tested on simple lab coupon specimen and lack experimental comparisons with local strain fields. Recent developments have expanded a modified smearing approach into mechanical fatigue, most notably by Koch et al. [23]. This takes progressive fatigue damage into account. The inherent discontinuity in the stress/strain relationship upon matrix cracking and fiber failure yields challenges in finite element analysis when attempting to reduce the material stiffness at integration points during a constant load. Koch found that a cycle jump approach with constant properties for each loading cycle had to be applied. Degradation was carried out between the jumps according to the size of the cycle jump. A similar approach is used in this work. While Koch compared the model to global experimental data, this work aims to estimate the local experimental strain data as obtained from digital image correlation monitoring of the modelled test specimen. The discrepancy between local and global properties was most notably highlighted by Sevenois et al. [24]. Sevenois argued that matrix crack initiation and propagation on the local scale happens long before catastrophic failure of typical composite fatigue test specimen. As noted by others [25–27], matrix voids affect the mechanical fatigue properties to a great degree, which was also found in the presented work here. This effect is also present in other similar materials such as concrete, where nanoparticles can be added to fill the voids and reduce microcracking [28]. Matrix voids induce matrix cracking on the micro level. It is essential to establish when matrix cracking is initiated on the local level to estimate fatigue life in a finite element model. However, so far this has not been taken into account and global cycles to failure for the material are used as input for local properties in most mechanical fatigue models. Sevenois also highlighted the scale problem. For example, atomistic bonds break long before any typical matrix crack is initiated in the structure. In engineering terms damage causing changes to the structural behavior on a component level is important. In this work the scale of interest is that of strain field changes observable through standard scale in DIC (digital image correlation). Sevenois also argued that detailed local models and sophisticated failure criteria fall short of modelling anything but a perfect structure. Matrix voids and variations in fiber volume fraction throughout the structure will make the real damage development complex. In this work, all the above has been acknowledged and addressed through parameter studies on matrix material properties. The resolution of the DIC method enables comparison between model and experiment on a very detailed level, taking into account local variations in material properties. For the fiber properties, local material properties were successfully found using a damage calculation method on the DIC data. Good correlation was found between model and experiment using the local fiber properties. The DIC methods used in this study have been elaborated in two articles explaining how to trace progressive failure in composites [29] and how to estimate a local S-N curve using DIC data [30]. DIC has recently been proven to be a valuable tool in estimating material parameters such as the fracture toughness [31] by tracing crack propagation visually. The very direct observation method (visual) and the vast amount of data make DIC a measurement method with huge potential for more exactly estimating and monitoring material parameters. That is, provided that the user has the ability to take advantage of the data using modern data tools.

This study suggests a simplified modeling approach that could be sufficient for understanding how local strain fields develop under fatigue loading in the composite material and how this may affect the global behavior. The modelling approach was implemented as a combination of cohesive surfaces and UMAT (user material subroutine) in Abaqus. A few simplifying methods were used:

i. Micro matrix failures were modeled using a continuum damage approach as changes in the stiffness matrix without directionality of the cracks.

ii. Macro (visible) matrix failures were modeled as discrete cracks permitted to propagate along predefined surfaces when certain strain states are met. They were used for through-the-thickness cracks in a ply and for delamination. Only selected macro cracks were modelled.

    iii.   Discontinuities in the stiffness due to crack growth were modeled using an on and off loading approach in combination with simplified cycle jumping [15,16].

    iv.   A range of polymer matrix properties were modeled to investigate the natural variations of material properties.

2. Experimental Setup

1 outlines the experimental split disk setup with vital dimensions included. The two holes, located at both sides of the disk, were designed to simulate extreme damage in the composite, and a tension-tension load control fatigue loading with an R-ratio of 0.1 was imposed.

The test rings were cut from filament wound specimen with a layup of hoop/axial/hoop/axial fibers as seen in cut A of Figure 1. The fiber orientation angles were $[\pm89°_2, \pm15°_1, \pm89°_2, \pm15°_1]$, typical for filament wound pressure vessels [6]. Figure 2 shows winding of the first axial layer. The fibers were HiPerTex W2020 glass fibers from 3B [32] and the resin was Epikote MGS RIMR 135 mixed with curing agent Epikure RIMH 137 [33]. The thickness of each layer was found through microscopy of the cross sections and is described in Figure 1. The holes were cut with a composite specific milling tool; 40200-HEMI produced by Seco Tools.
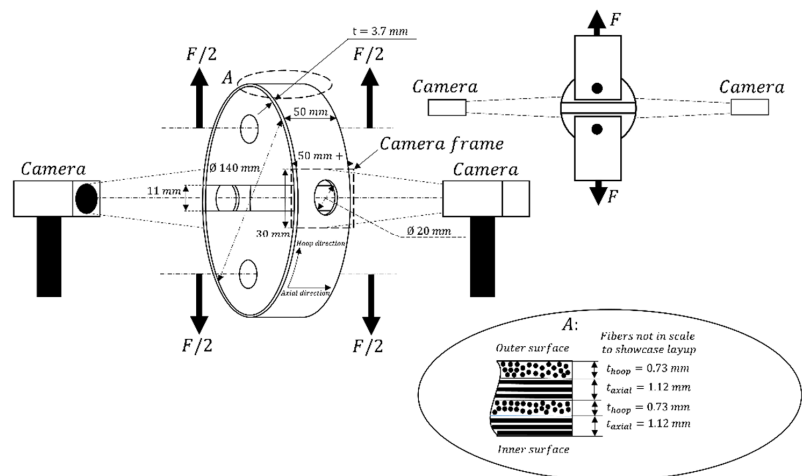
Figure 1. Experimental setup with geometry of test sample and layup; fibers not to scale.

Figure 2. Winding of the first axial layer of the pressure vessel.

Figure 3 shows the test setup in the laboratory. The cameras were timed against the load signal and images were taken at peak load with a frequency of 50 cycles between each image. The DIC data were post processed using Vic-2D from Correlated Solutions. Python scripts developed by the composite group at NTNU were used for extracting results and

performing data analysis. The resolution of the processed data was 4 points per mm^2. Adequate resolution was found through a sensitivity study trying several different resolutions.

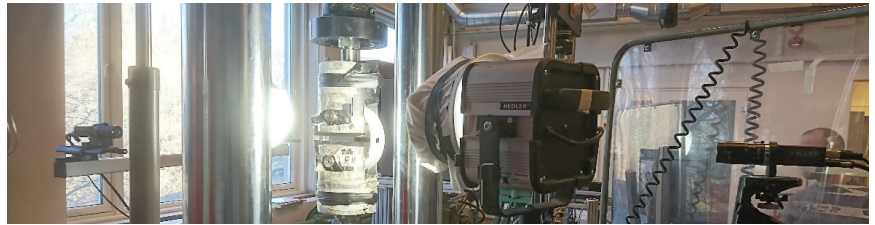**Figure 3.** Cameras and test rig with specimen installed. High intensity light was used to accommodate the short shutter speed.

3. Failure Criteria

3.1. General Approach

Failure criteria predict the onset of defined failure mechanisms. Once a state variable (here strain) in the material reaches the limit set by the failure criterion, the constitutive properties are degraded. The scale at which the failure criteria apply also needs to be defined. The scale on which the criteria operate can range from that of the component (load displacement curve from a test machine) and down to the atomistic level. A finite element analysis as used in this study typically represents the mesoscale.

This section describes the failure mechanisms and failure criteria used on the different scales and how the changes in properties are reflected in the constitutive relations. The following failure mechanisms were modeled:

i.   Micro fiber failure
ii. Micro matrix cracking (tensile and shear)
iii. Macro matrix cracking (shear failure)
iv. Macro Delamination

An UMAT material model handled the micro failure criteria inside the elements. Macro failures were modeled by a cohesive surface contact definition in Abaqus assuming that the plane of possible failure is known in advance. Figure 4 illustrates the domains of the two methods. Additionally shown are typical imperfections in a ply and sub-categories of micro and macro failure.
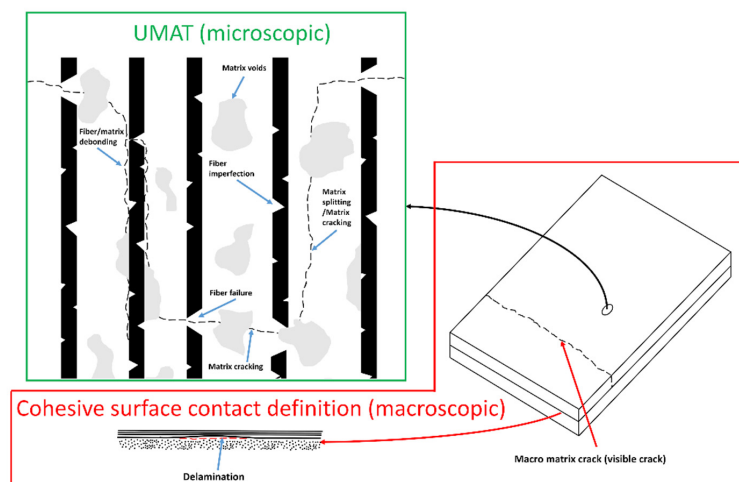

Figure 4. Overview of the failure mechanisms and which modelling method covers which mechanism.

3.2. Modelling Micro Damage with UMAT

Mechanical fatigue was described by a strain-based S-N curve in the log-log format, Equation (1):

$$\log\left(\hat{\varepsilon}_{ij}^{N}\right) = \log\left(\hat{\varepsilon}_{ij}^{O}\right) - \alpha_{ij}\log(N) \tag{1}$$

where $\hat{\varepsilon}_{ij}^{O}$ and α_{ij} are the intercept and slope of the S-N curve respectively and subscript ij denotes the strain components as defined in Figure 5. The number of cycles to failure N_{fail} was defined as in Equation (2):

$$N_{fail} = \begin{cases} \left(\frac{\hat{\varepsilon}_{ij}^{O}}{\varepsilon_{ij}^{N}}\right)^{\frac{1}{\alpha_{ij}}} \text{ for } \varepsilon_{ij} < \hat{\varepsilon}_{ij} \\ 1 \text{ for } \varepsilon_{ij} \geq \hat{\varepsilon}_{ij} \end{cases} \tag{2}$$
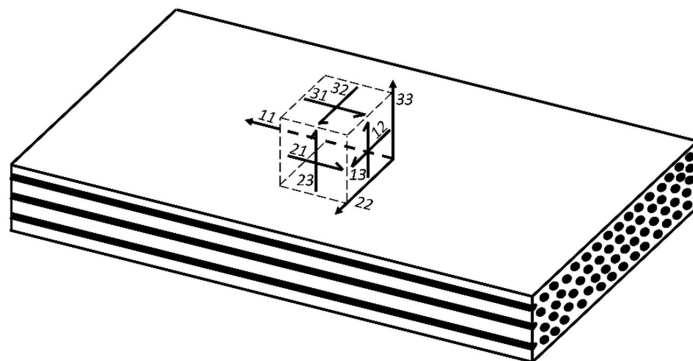

Figure 5. Definition of material directions/components.

If the static strain to failure $\hat{\varepsilon}_{ij}$ was less than $\hat{\varepsilon}_{ij}^{O}$ a cut-off was added to the S-N curve.

Since the strain field changes with the development of partial damage under cycling, the Miner sum M was used, expressed in Equation (3).

Given k number of loadblocks with N^k cycles in each load block at ε_{ij}^k strain in each load block:

$$M_{ij} = \sum_{k=1}^{k} \frac{N^k}{N_{fail}\left(\varepsilon_{ij}^k\right)} \tag{3}$$

N^k is the number of cycles at strain ε_{ij}^k and $N_{fail}\left(\varepsilon_{ij}^k\right)$ is the number of cycles to failure at strain ε_{ij}^k. k denotes the strain blocks in the Miner sum calculation. A Miner sum of 1.0 is equivalent to breaching the S-N curve failure envelope.

Instead of only calculating the Miner sum, which is a non-physical number, it was useful to define an exposure factor f_{ij}, see Equation (4). The factor describes the ratio of load to material strength at the applied strain ε_{ij} after a certain strain history described by the Miner sum. Failure happens when $f_{ij} \geq 1$.

$$f_{ij} = \frac{\varepsilon_{ij}}{\varepsilon_{res,ij}} \tag{4}$$

$\varepsilon_{\text{res,ij}}$ is Hashins's residual strain [34], expressed in Equation (5). It describes the strain to failure after partial fatigue if the material should fail in the next single cycle. It is a direct consequence of the Miner damage rule given in Equation (3).

$$\varepsilon_{\text{res,ij}} = \hat{\varepsilon}_{ij}^{O} \left[1 - M_{ij}\right]^{\alpha_{ij}} = \hat{\varepsilon}_{ij}^{1} \left[1 - \sum_{k=1}^{k} \frac{N^k}{N_{\text{fail}}\left(\varepsilon_{ij}^{k}\right)}\right]^{\alpha_{ij}} \tag{5}$$

The exposure factor enables the introduction of a partial degradation of the material before the particular failure mechanism has happened.

The exposure factor varies for the different strain components since applicable strains and S-N curves may differ. The full set of exposure factors are given in Equation (6). Note that the matrix dominated strains ε_{22} and ε_{33} are influenced by the strain ε_{11} in the fiber direction due to the Poisson's effect, as follows from Equation (6). The opposite coupling is however neglected since this coupling gives neglectable differences in ε_{11} due to the stiffness difference between longitudinal and transverse direction. As the failure criteria were defined such that failure in one matrix associated component or plane (22, 33, 12, 13, or 23) gives failure in all matrix associated components, the coupling between ε_{22} and ε_{33} was also neglected.

$$\begin{bmatrix} f_{11} \\ f_{22} \\ f_{33} \\ f_{12} \\ f_{13} \\ f_{23} \end{bmatrix} = \begin{bmatrix} \frac{1}{\varepsilon_{\text{res, 11}}} & 0 & 0 & 0 & 0 & 0 \\ \frac{V_{12}}{\varepsilon_{\text{res,22}}} & \frac{1}{\varepsilon_{\text{res,22}}} & 0 & 0 & 0 & 0 \\ \frac{V_{13}}{\varepsilon_{\text{res,33}}} & 0 & \frac{1}{\varepsilon_{\text{res,33}}} & 0 & 0 & 0 \\ 0 & 0 & 0 & \frac{1}{\varepsilon_{\text{res,12}}} & 0 & 0 \\ 0 & 0 & 0 & 0 & \frac{1}{\varepsilon_{\text{res,13}}} & 0 \\ 0 & 0 & 0 & 0 & 0 & \frac{1}{\varepsilon_{\text{res,23}}} \end{bmatrix} * \begin{bmatrix} \varepsilon_{11} \\ \varepsilon_{22} \\ \varepsilon_{33} \\ \varepsilon_{12} \\ \varepsilon_{13} \\ \varepsilon_{23} \end{bmatrix} \tag{6}$$

The consequence of failure is a specific change of the set of orthotropic elastic properties of the ply for each failure mechanism. The elastic properties were changed by stiffness reduction factors S_{ij} as given in Equations (7) and (8a,b).

$$\begin{bmatrix} E_{11} \\ E_{22} \\ E_{33} \\ G_{12} \\ G_{13} \\ G_{23} \end{bmatrix} = \begin{bmatrix} S_{11} & 0 & 0 & 0. & 0 & 0 \\ 0 & S_{22} & 0 & 0 & 0 & 0 \\ 0 & 0 & S_{33} & 0 & 0 & 0 \\ 0 & 0 & 0 & S_{12} & 0 & 0 \\ 0 & 0 & 0 & 0 & S_{13} & 0 \\ 0 & 0 & 0 & 0 & 0 & S_{23} \end{bmatrix} * \begin{bmatrix} E_{11} \\ E_{22} \\ E_{33} \\ G_{12} \\ G_{13} \\ G_{23} \end{bmatrix} \tag{7}$$

$$\begin{bmatrix} V_{12} \\ V_{13} \\ V_{23} \end{bmatrix} = \begin{bmatrix} S_{12} & 0 & 0 \\ 0 & S_{13} & 0 \\ 0 & 0 & S_{23} \end{bmatrix} * \begin{bmatrix} V_{12} \\ V_{13} \\ V_{23} \end{bmatrix} \tag{8a}$$

$$V_{21} = \frac{E_{22}}{E_{11}} * V_{12}, \quad V_{31} \; V_{31} = \frac{E_{33}}{E_{11}} * V_{13}, \quad V_{32} \; V_{32} = \frac{E_{33}}{E_{22}} * V_{23} \tag{8b}$$

The Young´s and shear moduli are denoted E_{ij} and G_{ij} and the Poisson´s ratios are v_{ij}. How the stiffness reduction factors were changed is described in Table 1. The choices behind the factors and their interaction will be explained below.

Table 1. How reduction factors are changed depending on failure criterion.

	S_{11}	S_{22}	S_{33}	S_{12}	S_{13}	S_{23}
Fiber failure ($f_{11} > 1.0$)	0.1	0.1	0.1	0.1	0.1	0.1
Matrix failure ($f_{22}, f_{33}, f_{12}, f_{13}$ or $f_{23} > 1.0$)	0.9	0.1	0.1	0.1	0.1	0.1

As can be seen in Table 1, the factors changed the stiffness extensively, from full stiffness to 10% stiffness. To ease the change, the stiffness was gradually reduced from the intact to the failed value over an exposure factor span from 0.8 to 1.0, as expressed in Equation (9). This is schematically shown in Figure 6 for a reduction from 1.0 to 0.1. Particularly for elements with an exposure factor fluctuating about 1.0, the softening eases the iterative scheme, avoiding distorted elements with a large internal stiffness difference. The largest exposure factor of components 22, 33, 12, 13, and 23 was used as basis for reducing the constitutive properties in these components, in accordance with Table 1.

$$\begin{aligned} &\text{if all } f_{ij} \leq 0.8 \text{ then } S_{ij} = 1.0 \\ \text{for largest } f_{22-23} : &0.8 \leq f_{22-23} \leq 1.0 \text{ then } S_{22-23} = 4.6 - 4.5f_{ij} \text{ and } S_{11} = 1.4 - 0.5f_{11} \\ &\text{if } f_{11} \ : 0.8 \ \leq f_{11} \leq 1.0 \text{ then } S_{11-23} = 4.6 - 4.5f_{ij} \\ &\text{if any } f_{22-23} \geq 1.0 \text{ then } S_{22-23} = 0.1 \text{ and } S_{11} = 0.9 \end{aligned} \tag{9}$$
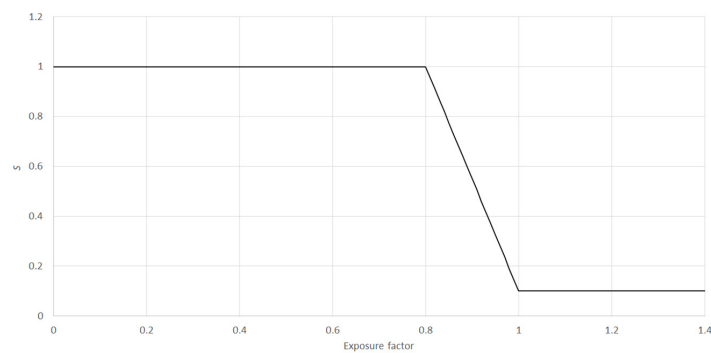

Figure 6. Schematic showing the change of stiffness with exposure factor.

3.3. Modeling Macro Damage with Abaqus Contact Definitions

Delaminations and macro shear cracks penetrating the entire thickness of a ply were described as macro damage, see Figure 4. Delaminations may occur between all the layers. The layers were therefore modeled separately with Abaqus' cohesive surface contact defined on the interfaces. Macro shear cracks were known to develop and extend at four locations in the test specimen. They initiated at the equator of the hole and extended in the loading (hoop) directions along the shear strain bands. Modelling the location of the cracks directly into the FE models significantly simplified the modeling approach.

Abaqus' cohesive surface definition was used with a triangular traction-separation response, illustrated in Figure 7 with the values from the normal direction (t_n, G_n). The separation is defined in mm between the two surfaces. The triangle is defined by an initial elastic stiffness (K) defined by the characteristic element length as given in Equation (11). Upon reaching the maximum stress (t), the contact stiffness is reduced according to the fracture energy G. The elastic stiffness (K) was defined according to suggestions by Diehl [35]. Diehl found that the contact stiffness in the elastic regime was best described using a factor of 0.05 on the characteristic element length as described in Equation (11). The characteristic length was defined as the mean element length, d, along the shear crack in the finest meshed region of the model, giving a d of 0.255 mm. Based on suggestions by Perillo [36] on the used material, the Benzeggagh-Kenane (BK) mixed mode behavior was used along with an energy mixed mode ratio with a BK exponent of 1.4. While the cohesive surface definition needs a defined crack path (here the ply interfaces and shear bands), it is possible to model fatigue macro cracks independently using cohesive zone modelling, CZM [7]. This approach does, however, demand user defined elements (UEL). While this approach is perhaps a closer representation of reality and would not necessitate pre-definition of the shear cracks and ply interfaces in the model, there are several reasons why this approach could not be used in this study. Primarily it is due to the fact that it is, to the authors' knowledge, only possible to run one user defined script (UEL or

UMAT) at a time in Abaqus. Further, CZM is very computationally expensive and would make the runtime impractical. The basic theory is however the same for CZM and the surface definition, with separation between elements and damaged defined with fracture energy. Rozylo carried out a thorough study on CZM in Abaqus and how it could model progressive cracking in buckling experiments in [20]. Rozylo found that the CZM approach was able to match the experiments well. Despite Rozylo carrying out idealized experiments the strain fields were complex giving promise to the CZM for future work.
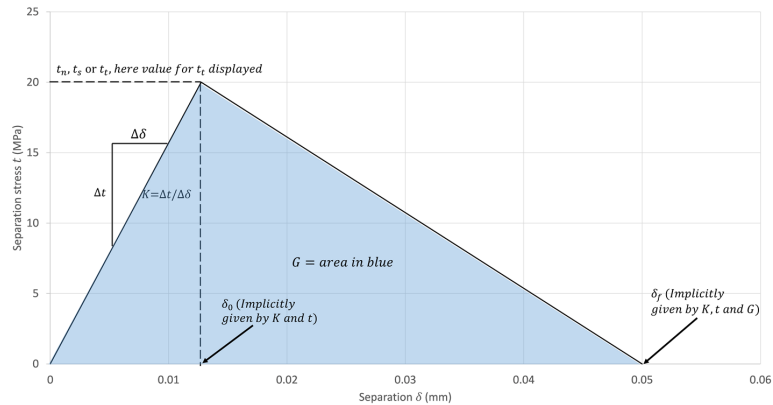

Figure 7. The shape and variables in the traction-separation response. The values on the axis are for the normal component in the traction separation contact definition.

To account for mechanical fatigue in the cohesive surface definition, the contact properties were reduced. The separation stress and the fracture energy were scaled with a factor of 0.6. This factor, 0.6, was chosen based on the graph in Figure 8 showing the S-N curve for the matrix shear with the globally reduced property in red. Details on how the S-N curve was found are given in the Material Properties section. The red line is set close to the convergence of the matrix S-N curve within the cycle span of interest, from 0–100,000 cycles; as the specimen failed at 127,814 cycles. Any strain above this threshold will lead to failure within very few cycles relative to the cycles to failure. The scaling method was done as there is no fatigue definition built into the standard delamination crack definition of Abaqus and it was not possible to the authors' knowledge to run a separate user subroutine on contact properties and micro damage UMAT simultaneously.

$$t_n = \hat{\sigma}_{22T} * 0.6 = 20.0, \ t_s = t_t = \hat{\tau}_{12} * 0.6 = 21.6 \tag{10}$$

$$K_n = \frac{t_n}{d * 0.05}, \ K_s = \frac{t_s}{d * 0.05}, \ K_t = \frac{t_t}{d * 0.05}$$
$$d = 0.255 \text{ mm} \tag{11}$$

$$G_n = 0.83 * 0.6 = 0.5$$
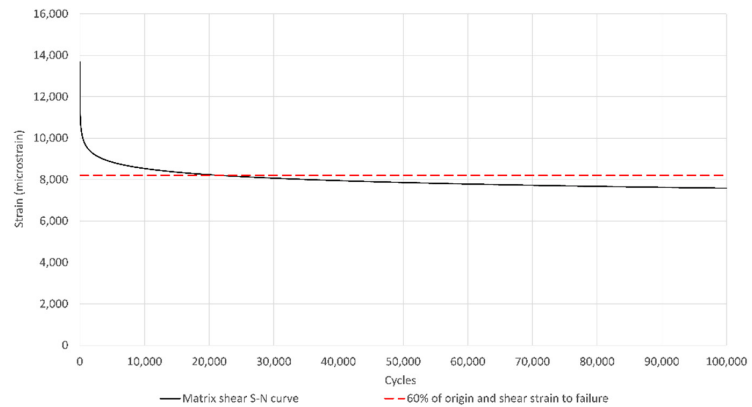$$G_s = G_t = 3.15 * 0.6 = 1.9 \tag{12}$$

Figure 8. S-N curve for the matrix shear plotted against the reduction factor on the delamination properties. See the Material Properties section for further information on the S-N curve.

4. Cycle Jump Method

4.1. Overview

Fiber and matrix material have little or no yielding once the failure criterion is met. Upon failure they cease to carry the load and the stress-strain curve is discontinuous as a result, shown schematically in Figure 9. The ideal fatigue-degradation material subroutine would iterate the stiffness based on the applied cycles and stress. The local stiffness for each cycle would be decided by a changing and discontinuous stress/strain curve as displayed in Figure 9. As cycles increase, $\hat{\varepsilon}$ and $\hat{\sigma}$ would become lower. Upon reaching $\hat{\varepsilon}$ and $\hat{\sigma}$, the routine would have to be able to handle a negative tangent stiffness. Negative tangent stiffness is in theory impossible using conventional iterative schemes. The fatigue material subroutine outlined above is therefore impossible. The problem was avoided in the presented work by using a cycle jump method, similar to that explored by Harper and Koch [16,23].
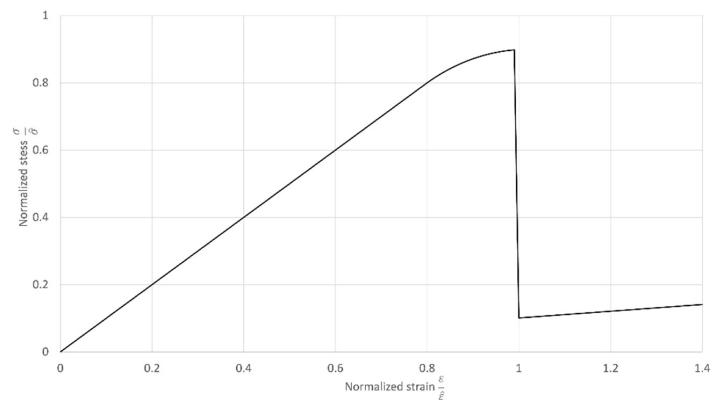
Figure 9. Schematic of a stress/strain curve for a typical fiber or matrix material normalized to the failure stress/strain.

4.2. Implementation

The cycle jump approach has two distinct phases: (i) loading and offloading and (ii) cycle iteration, similar to that explored by Koch [23]. In the loading phase, peak exposure factors and strain in all integration points are recorded. Stiffness is kept constant and not changed as the load is increased to avoid local negative tangent stiffness. When the

peak load is reached, the offloading and cycle iteration phase is initiated. Here the Miner sum is calculated on the peak strains from the loading phase and the exposure factors are changed with cycles. The stiffness is still kept constant in this phase, as the structure offloads to the strain and stress state before loading. Upon initiation of the next loading phase the stiffness is changed according to the new exposure factors from the cycle iteration and the procedure is repeated. In case of simulations with varying fatigue load, this can be achieved by loading to different loads.

Referring to Equations (6)–(8a,b), $\varepsilon_{res,ij}^{k}$ and S_{ij} are kept constant during the loading phase and ε_{ij}^{k} is changed, following the strains in the integration points. During the offloading and cycle iteration phase, ε_{ij}^{k} is kept constant at the peak strains recorded in the loading phase. ε_{ij}^{k} is therefore free from the strain in the integration points and the structure is left to unload by itself. Now $\varepsilon_{residual,ij}^{k}$ is changed according to the cycle in the given iteration. Upon initiation of the next loading phase, S_{ij} is changed according to Equation (9).

Due to the cohesive surface contact definition, the unloading phase may yield singularities in the stiffness matrix. To overcome this, damping was introduced in this phase to have the structure relax without causing singularities.

Figure 10 shows the cycle jump approach explained schematically. The damping is evident in Figure 10 as the displacement curve lags behind the loading curve in the offloading and cycle iteration phase. As the iterative scheme is dependent on the structural response from the damping, the numbers of cycles where results are available in the offloading and cycle iteration phase are not fixed; however, at the end of this phase/step they are. The cycle jumps were chosen based on experimental data in this work.
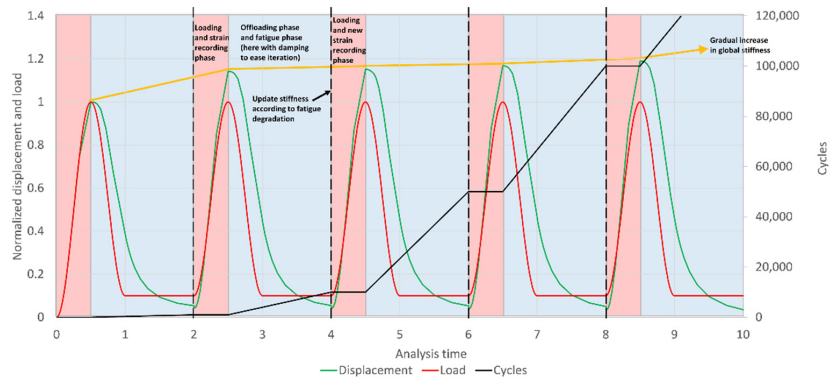

Figure 10. Schematic curves showing how the stiffness changes according to fatigue damage based on the peak strain in each in-tegration point based on the past cycle block.

For complicated models the runtime is long even with high memory and high CPU capacity computers; therefore the cycle jumps has to be placed with care and at critical points in the load history. In most cases this is at the start and end of the component's lifetime. At the start there will be initial matrix cracking and at the end of life there will be extensive fiber failure [37]. In between, the strain distribution will be relatively stable and cycle jumps may be relatively big as a result. Given a load to displacement history from an experiment, it is therefore advisable to place the loading phases at cycles where changes occur in the load to displacement history. Due to the long runtime, it is time consuming to study several different cycle jumps. This study implemented only four well-chosen cycle jumps. Despite this coarse approach, the method gave a good indication of where damage initiated and how this damage affected the strain distribution and material behavior over time. A further expansion of the method would be to include an automatic cycle jump procedure. This could be done by assigning a maximum damaged volume and having

the loading phases occur when damage extends over this specified volume. As such, the method would be completely independent of experimental data. This was done with success by Koch et al. [23] on simple models; however, it was not explored in this work due to the high computational cost. Alternatively, cycle jumps could be set at decreasing intervals until the results of a few cycle jumps converge. This procedure would be easy to implement, but would also require high computational times using a model as big as in this study.

4.3. Material Properties

Material properties of an orthotropic ply with transverse isotropic behavior were used for FEA modeling. A summary of all material properties is given in Table 2. Two main assumptions were made:

i. The plies have transverse isotropic behavior as per classic composite material models.
ii. Only material properties in the tensile direction were considered. The ring on the split disk experienced some compressive stresses. However, since these stresses were small and not in critical regions for the structural integrity, they were not considered and simply modeled with the tensile fatigue data.

Most of the material properties were measured in our laboratory during previous projects from standard coupons made of the same glass fiber and epoxy matrix. Data were obtained for unidirectional flat materials. Filament wound materials have a curvature and are strictly speaking not unidirectional. Properties were scaled to apply to filament wound material using a FEA approach by Perillo et al. [38]. The static properties in the direction of the fiber and matrix (E_{11}, E_{22}, $\hat{\sigma}_{11T}$, $\hat{\sigma}_{11C}$, $\hat{\sigma}_{22T}$, $\hat{\sigma}_{22C}$, $\hat{\tau}_{12}$) were linearly scaled to account for differences in the fiber volume fraction between the filament wound material in this study and that of Perillo.

Table 2 shows the material properties and the methods used to obtain them. Only one static property was measured for this particular study: the maximum static strain to failure of the fibers. Compared to the original maximum static strain found by Perillo of 22,150 microstrain [38], the value reported here of 40,000 microstrain is considerably greater. The value was found from DIC strain measurements taken from static split disk tests [30]. Upon catastrophic failure, 40,000 microstrain was the highest strain recorded. This maximum strain deviated by a margin of almost two from strain at the exact point of failure of 22,150 microstrain, similar to what was found by Perillo from standard coupon testing. The weakest point had similar properties to data obtained by coupon testing, as coupon tests measure the weakest part of the sample. The DIC data showed however that the local strains can be much greater without causing failure. The greatest local strain (40,000 ms) was used for the fatigue analysis.

Fatigue properties were described by strain-based S-N curves for the three in-plane material components of an orthotropic ply: fiber, transverse, and shear components. Figure 11 shows the three individual S-N curves in a linear strain presentation. In all cases the S-N curves could be well described by the log-log presentation as given in Equation (1). All testing was done for an R-ratio of 0.1 (tension-tension). This is the most relevant loading condition for pressure vessels being cycled between nearly empty and full.

Through-the-thickness shear (intralaminar shear) was measured on Short Beam Shear SBS specimen cut from the filament wound vessel with geometry according to the ASTM D2344M standard. The slope of the log-log S-N curve was found by linear regression according to Equation (1). Figure 12 shows the data points and curve fit of the SBS testing. The slope of the curve is 0.051. Nearly the same slope (0.054) was found for the same constituents tested on flat specimens by Gagani [19].
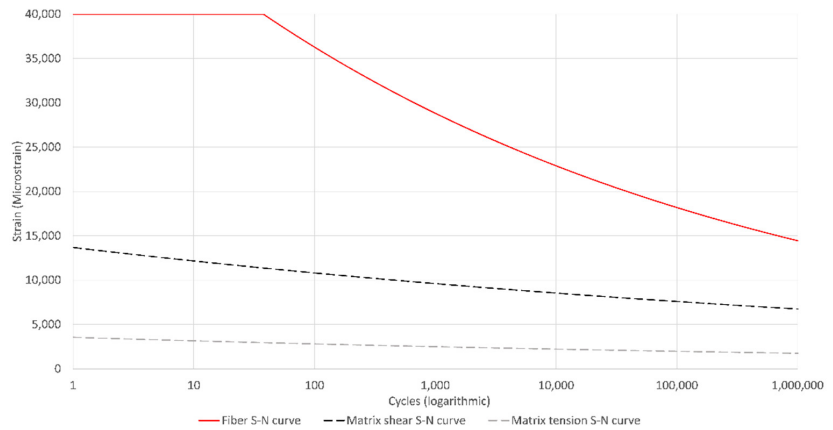
Figure 11. Three S-N curves for the fiber and the matrix directions.

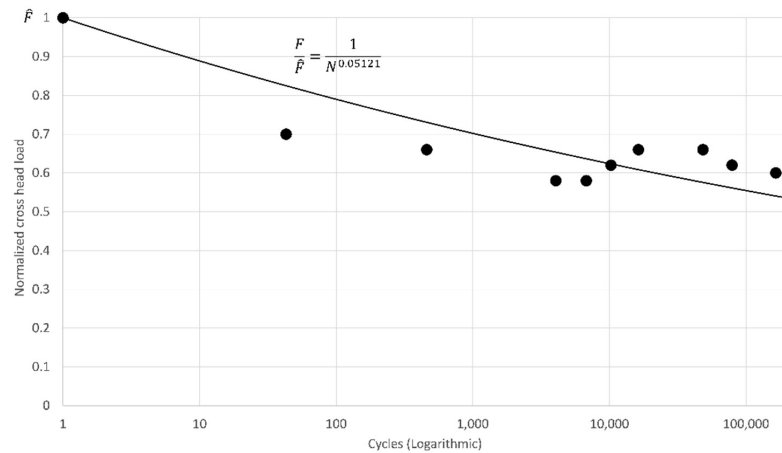$$\frac{F}{\hat{F}} = \frac{1}{N^{0.05121}}$$

Figure 12. S-N curve for the shear component with data points.

Fatigue properties for in plane matrix cracking were not measured, but taken from the intralaminar shear data. The slope from the shear data was used for the tensile matrix curve with the origin from the static properties. Using the same slope in both tensile and shear S-N curves is controversial; however, it has been shown before that the slope in the tensile matrix direction is in general low [8], as was also found for the shear.

DIC monitoring of the SBS and split disk testing revealed a high discrepancy between local and global fatigue failure and a large scatter in matrix properties. To account for the variations in local properties, a parameter study on the matrix fatigue properties was done and is reported in the Results section, changing the intercept/origin strain of the S-N curves. The parameter study made the exact knowledge of the matrix dominated S-N curves less critical, as the properties were changed in the analysis anyway to capture the experimental scatter.

Local fatigue properties of the fiber were obtained by using DIC data from testing of three split disk ring tests with a hole [30]. Strain based S-N curves were found by an iterative process. Local fiber failures were predicted using Miner sum calculations on the DIC strain data, as in Equations (1)–(3). The predictions were compared with the measured failure of the samples. The S-N curve was changed until a good match between predictions and experiments was achieved. Details of the procedure are given in [30]. The S-N curve giving the best fit with the experimental data had a slope of 0.1, the same as usually

measured for this type of material using standard coupon data [10,11,39–43]. However, the origin of the local S-N curve had to be greater than for typically obtained S-N curves to match the experimental data. The local S-N curve for fiber failure had to be shifted up by about a factor three compared to typically reported curves from coupon testing. This resulted in an intercept of the S-N curve for one cycle that is greater than the static strain found from DIC data, giving a cut-off of 30 cycles on the S-N curve.

Table 2. Material parameters.

Material Parameter	Value	Units	Test Method	Source
		Elastic stiffness properties		
E_{11}	33.06	GPa	ASTM D3039	[38]
E_{22}	9.423	GPa	ASTM D3039	[38]
E_{33}	E_{22}	GPa	Assumption	[38]
G_{12}	2.630	GPa	ASTM D3518/D3518M–13	[38]
G_{13}, G_{23}	G_{12}	GPa	Assumption	[38]
		Static properties		
$\hat{\varepsilon}_{11T}$	40,000	Microstrain	DIC data from static testing [30]	
$\hat{\varepsilon}_{11C}$	354	MPa	ASTM D3410	[38]
$\hat{\varepsilon}_{11C}$	10,725 ($\hat{\sigma}_{11C}/E_{11}$)	Microstrain	ASTM D3410	[38]
$\hat{\sigma}_{22T}$	33.4	MPa	ASTM D3039	[38]
$\hat{\sigma}_{33T}$	$\hat{\sigma}_{22T}$	MPa	Assumption	[38]
$\hat{\varepsilon}_{22T}$	3545 ($\hat{\sigma}_{22T}/E_{22}$)	Microstrain	ASTM D3039	[38]
$\hat{\varepsilon}_{33T}$	$\hat{\varepsilon}_{22T}$		Assumption	[38]
$\hat{\sigma}_{22C}$	96	MPa	ASTM D3410	[38]
$\hat{\sigma}_{33C}$	$\hat{\sigma}_{22C}$		Assumption	[38]
$\hat{\varepsilon}_{22C}$	10,182 ($\hat{\sigma}_{22C}/E_{22}$)	Microstrain	ASTM D3410	[38]
$\hat{\varepsilon}_{33C}$	$\hat{\varepsilon}_{22c}$		Assumption	[38]
$\hat{\tau}_{12}$	36	MPa	ASTM D3518	[38]
$\hat{\tau}_{13}, \hat{\tau}_{23}$	$\hat{\tau}_{12}$		Assumption	[38]
$\hat{\varepsilon}_{12}$	13,681 ($\hat{\tau}_{12}/G_{12}$)	Microstrain	ASTM D3518	[38]
$\hat{\varepsilon}_{13}, \hat{\varepsilon}_{23}$	$\hat{\varepsilon}_{12}$		Assumption	[38]
		Fatigue properties		
$\hat{\varepsilon}_{11T}^{O}$	57,500	Microstrain	DIC data from fatigue testing [30]	
$\hat{\varepsilon}_{11C}^{O}$	$\hat{\varepsilon}_{11T}^{O}$		Simplification	
$\hat{\varepsilon}_{22T}^{O}, \hat{\varepsilon}_{33T}^{O}, \hat{\varepsilon}_{22C}^{O}, \hat{\varepsilon}_{33C}^{O}$	$\hat{\varepsilon}_{22T}^{O}$	Microstrain	Simplification and assumption	
$\hat{\varepsilon}_{12}^{O}, \hat{\varepsilon}_{13}^{O}, \hat{\varepsilon}_{23}^{O}$	$\hat{\varepsilon}_{12}^{O}$	Microstrain	Simplification and assumption	
α_{11T}	0.1	-	DIC data from fatigue testing	
α_{11C}	α_{11T}	-	Simplification	
α_{12}	0.05121	-	ASTM D2344/D2344M	Figure 12
$\alpha_{22T}, \alpha_{22C}, \alpha_{33C}, \alpha_{33T}, \alpha_{13}, \alpha_{23}$	α_{12}	-	Simplification	
		Cohesive surface contact definition		
t_n	$\hat{\sigma}_{2t} * 0.6 * = 20.0$	MPa	Assumption	[38]
t_s	$\hat{\tau}_{12} * 0.6 * = 21.6$	MPa	Assumption	[38]
t_t	t_s		Assumption	[38]
G_n	$0.83 * 0.6 * = 0.5$	N/mm	ASTM D5528	[38]
$G_s = G_t$	$3.15 * 0.6 * = 1.9$	N/mm	ENF (End Notched Flexure) test [44–46]	[38]

* See section FEA model for factor explanation.

5. Finite Element Model

5.1. Geometry

The composite ring was modelled as a 1/8 model with the geometry in the schematic in Figure 1. The model can be seen in Figure 13. The layers (hoop/axial/hoop/axial) were modelled with five elements thickness each, as can be seen in Figure 14. Each layer was defined through the composite layup function in Abaqus. The layers were defined in this function as $10 \pm$ layers ($+15°, -15°, +15°, \ldots, -15°$ and $+89°, -89°, +89°, -89°, \ldots, -89°$), essentially smearing the properties.
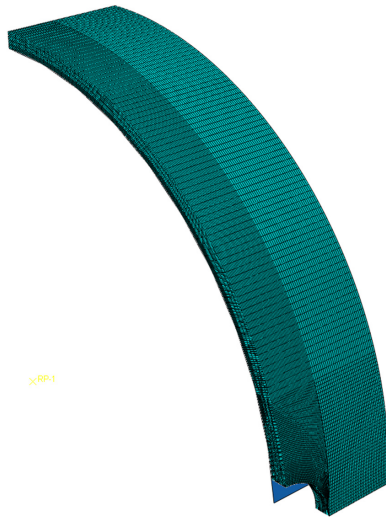

Figure 13. D Model of 1/8 of the split disk. The disk is represented by the rigid surface under the laminate.
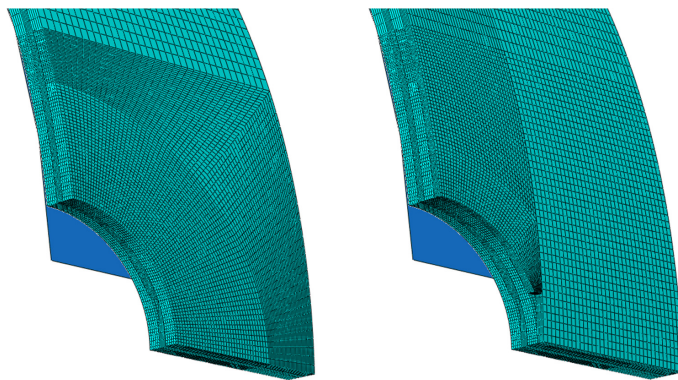

Figure 14. Detail of mesh in split disk model. To the left is from the middle axial layer, to the right is from the upper hoop layer.

The ring was meshed using hexagonal eight node reduced integration elements, C3D8R and had 223,734 elements. As explained in the Failure Criteria section, the layers had a cohesive surface contact definition defined between them to model delamination. The crack (along main shear band) evident in the top hoop layer in Figures 13 and 14 also had the cohesive surface contact definition as explained in the same section. The crack was only present in the hoop layers, while the axial layers were meshed as shown to the left in Figure 14.

5.2. Loads and Constraints

Table 3 gives detailed constraint definitions with reference to Figure 15 for surface name definitions. The cylindrical coordinate system is defined with a radial and a tangential vector.

Table 3. Overview of constraints using normal symmetry.

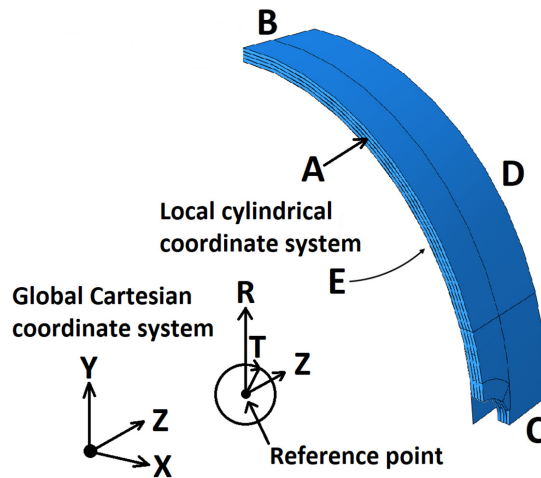| Surface	Displacement Constraints	Rotational Constraints (Around Axis)
A	Z Local	-
B	T Local	-
C	T Local	-
D	Free	-
E	R Local (with 0.05 friction coefficient in T and Z direction)	-
Center reference point	X, Z Global	X, Z Global

Figure 15. Overview of constraints, surface names, reference point, and the cylindrical coordinate system.

6. Results

6.1. Experimental Results

This study compares experimentally obtained strain fields to FEA modeling of one composite ring with a hole as shown in Figure 1, tested with the split disk test method in fatigue. The strain fields in the vicinity of the hole were measured by DIC every 50 cycles. The sample failed at 127,814 cycles, shortly after the last DIC frame at 127,768 cycles.

Figure 16 shows the cycles to displacement curve from the test machine. The dotted lines are the cycle jumps in the FEA model; these will be further explained in the FEA results section. Catastrophic layer failure/fiber failure in the individual layers happened over relatively short cycle spans indicated by sudden displacement jumps in the curve. The layer failures are highlighted with arrows and text in Figure 16.

There were four regions around the hole in the disk that concentrated strain. The regions are highlighted in Figure 17 over the contour plot of hoop strain close to catastrophic failure. The first fiber failure has already occurred as indicated by the white gap above the black rectangle. The gap was first visible at about 122,000 cycles, roughly 6000 cycles before catastrophic failure of the surface layer. This large fiber failure led to the sudden jumps in the displacement curve visible in Figure 16. It initiated progressive fiber failure

that ripped the layer across the region indicated in the black line slice in Figure 17 before it progressed to the other side of the hole.
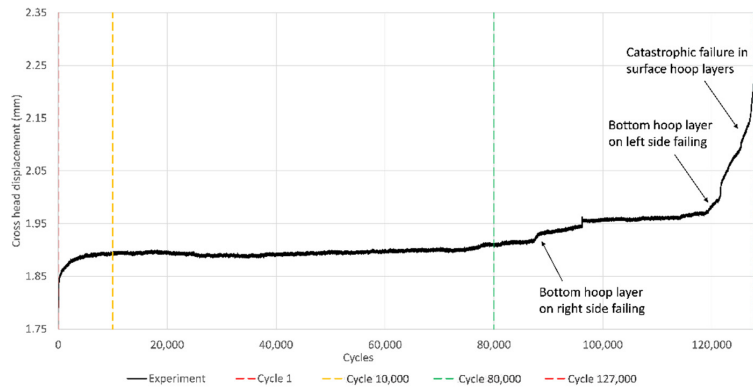

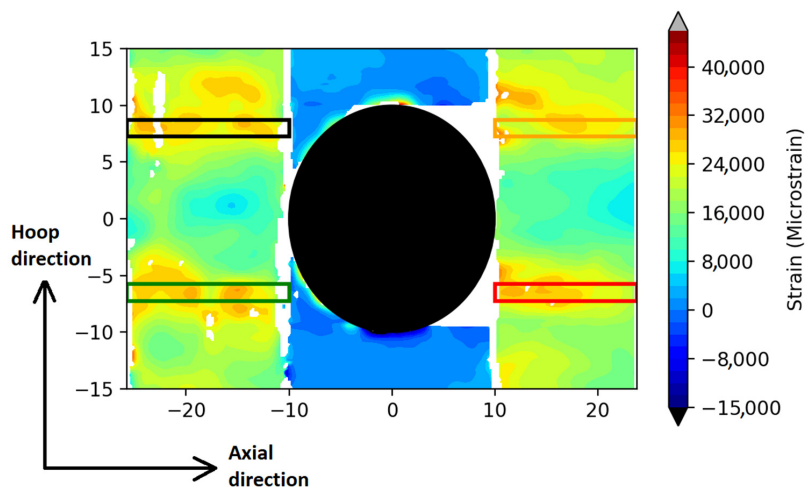**Figure 16.** Cycle to displacement curve and cycle jumps.

Figure 17. Hoop strain contour plot around the hole at cycle 127,768, shortly before catastrophic failure. The four rectangles highlight the four strain concentrations around the hole.

Intuitively there should be only two regions that concentrate strain, one on each side of the hole at the equator. Macro splits (matrix cracks through the thickness of a ply) develop at these points after very few cycles and the splits grow rapidly in the load direction. The splits and bending of the material between the splits move the strain concentrations to the ends of the splits [47] at the four regions shown in Figure 17.

Provided a perfect material, the four regions around the hole should have equal strain fields throughout the test and equal damage development. Figure 18 shows the strain curves over the length of the four regions at selected numbers of cycles. Cycle 350 was the first recorded cycle by the DIC (cycle 1 was not recorded). The x-axis is in absolute values (note: no negative x values), 10 mm is at the edge of the hole, and 24–26 mm is at the outer edge of the specimen. The curves are evidently not equal. Particularly at cycle 80,000, a factor 1.5–2 difference can be seen between the regions. The differences are due to variations in void content in the matrix, fiber density, and layer thickness; these variations can easily be seen under the microscope, as shown in Figure 19.
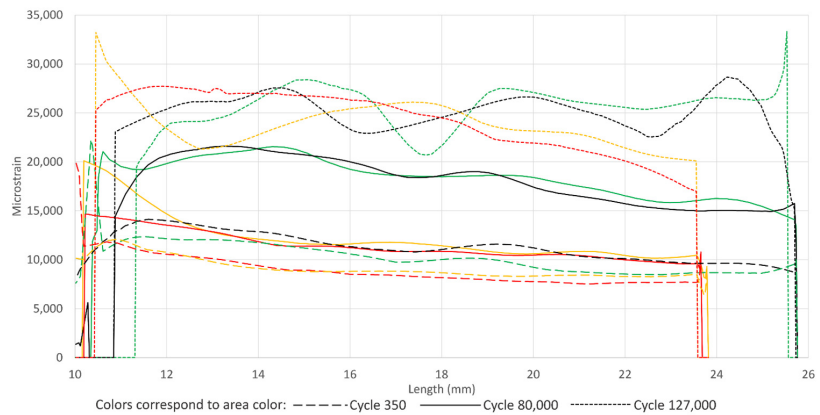
Figure 18. Hoop strain curves from the regions in Figure 17 for different cycles.
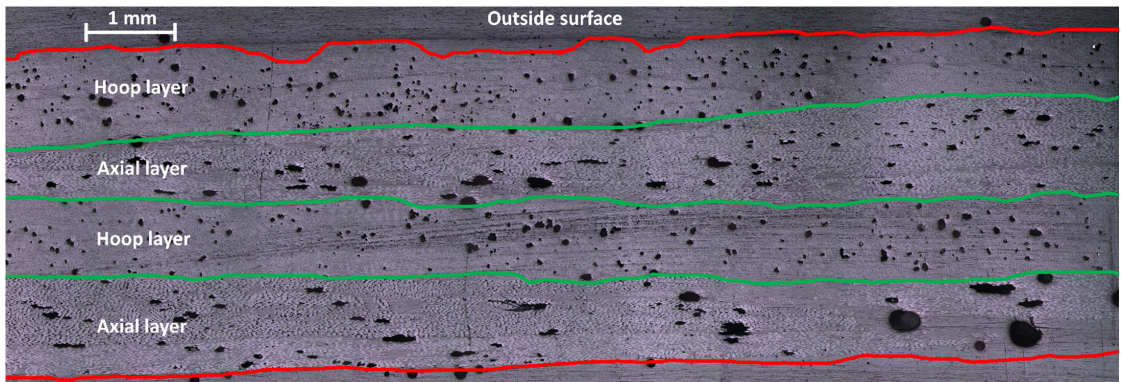

Figure 19. Microscopy of the split disk specimen. As can be seen there are many voids (black) and a big variation in layer thickness over the cross section.

It can be seen in Figure 18 that the strains measured by DIC have a quite pronounced strain concentration at the splits, at the 10 mm position, at a low number of cycles. With increasing number of cycles, the average strain increases but the strain concentration diminishes or moves even to the outer edge of the specimen. This effect is due to matrix damage spreading in the material changing the constitutive properties of the material [29].

6.2. FEA Results

The goal of the FEA modelling was to predict the correct strain field and damage development throughout the fatigue life of the specimen caused by the chosen failure mechanisms using their fatigue failure criteria with corresponding material properties. As shown in Figures 17 and 18 the specimen had big variations in the shape of the experimentally measured strain field over the surface. To capture the variations, the FEA model was run for four cases with different matrix material properties and one case with the failure mechanism in the fiber direction disabled. Tables 4 and 5 show the chosen variations of properties in the models. Model A had nominal properties as defined in the Material Properties section. Models B–D had degradation on matrix properties down to 40% of the original values. In addition, the matrix damage effect on stiffness in the fiber direction was lowered down to 0.7 for the fiber for Model C and D, while Model E had the property degradation in the fiber direction disabled. The properties for the models are a representative selection of a parameter study that explored what correlated best

with the range of experimental results. All models apart from Model A evidently deviate from the assumed physics of the problem, as defined in the Failure Criteria section. It was, however, interesting to explore what degradation was necessary to better capture the experimental results.

Table 4. Parameters for Models A to D for FEA simulations.

	Factor Applied to Nominal Static Values and S-N Curve Origin $(\hat{\varepsilon}^O_{22T}, \hat{\varepsilon}^O_{33T}, \hat{\varepsilon}^O_{22C}, \hat{\varepsilon}^O_{33C}, \hat{\varepsilon}^O_{12}, \hat{\varepsilon}^O_{13}, \hat{\varepsilon}^O_{23})$	Factor Applied to Contact Strength (t_n, t_s, t_t)	Factor Applied to Fracture Energy (G_n, G_s, G_t)	Stiffness Degradation Factor of Fiber upon Matrix Failure, S_{11}, see Table 5
Model A	1.0	$\hat{\sigma}_{22T} * 0.6$	0.6	0.9
Model B	0.6	$\hat{\sigma}_{22T} * 0.6$	0.6	0.9
Model C	0.6	$\hat{\sigma}_{22T} * 0.36$	0.36	0.6
Model D	0.4	$\hat{\sigma}_{22T} * 0.36$	0.36	0.6
Model E	0.6	0.6	0.6	0.7

Table 5. Stiffness reduction factors for Model C, D, and E.

	S_{11}	S_{22}	S_{33}	S_{12}	S_{13}	S_{23}
Fiber failure ($f_{11} > 1.0$)	0.1 (A–D)/1.0 (E)	0.1	0.1	0.1	0.1	0.1
Matrix failure ($f_{22,33,12,13,23} > 1.0$)	0.6 (C and D)/0.7 (E)	0.1	0.1	0.1	0.1	0.1

Variations in layer thickness were not included in this analysis as this is difficult to model correctly, but the effect was modeled indirectly as reduced matrix properties. The shear crack reduction factors were chosen based on the same evaluation as for models A to E.

FEA fatigue calculations were done using the cycle jump method as described previously. Figure 16 shows the cycle jumps over the cycle to displacement curve. The jumps were placed at interesting points in the cycle to displacement curve. Fiber/layer failure manifests itself as displacement jumps in the experimental curve. An increasing amount of matrix failure is expressed as the gradual increase in displacement between the fiber/layer failures particularly prominent over the first 10,000 cycles. The analysis cycle jumps were put before or at critical changes to the displacement curve. The cycle 1 jump is there to estimate the initial state, the cycle 10,000 jump to capture the initial matrix damage, the cycle 80,000 jump to capture the state just before first layer/fiber failure, and the cycle 127,000 jump to capture the state just before catastrophic failure at 127,814 cycles.

Ideally, more cycle jumps should be put between 80,000 and 127,000 cycles, considering the relatively big increase in the displacement. Due to analysis time this was, however, not feasible. The analysis time for one set of material parameters was six days on a fast 8 slot 64 GB RAM computer with an Intel Xeon W-2155 3.3 GHz CPU.

An example for comparing hoop strain fields calculated by the FEA with measured DIC data is shown in Figure 20 for Model D at 80,000 cycles. The most highly strained regions are qualitatively similar. However, the absolute values only match at a few locations. This is to be expected since the experimental data show quite high variations in the four sectors around the hole. The FE model produces the same results in each sector due to assumed symmetries.

Running the FE analysis for each matrix cracking material model described in Tables 4 and 5 allowed comparing the FEA against experimental data for different matrix properties. Figures 21–24 show the lowest and highest experimental strain across the most highly strained cross sections outlined in Figure 18 compared to the experimental results for the four models A, B, C, D, and E for cycle 1, 10,000, 80,000, and 127,000 respectively. The full colored curves correspond to colors of the regions in Figure 17. There is generally good agreement between experimental data and FEA calculated strains for all but the

127,000th cycle. The models fall between the extremes from the experiment for the 1st, 10,000th, and 80,000th cycle. This shows that the chosen matrix material models represent the various degrees of random material variations of the matrix properties fairly well.
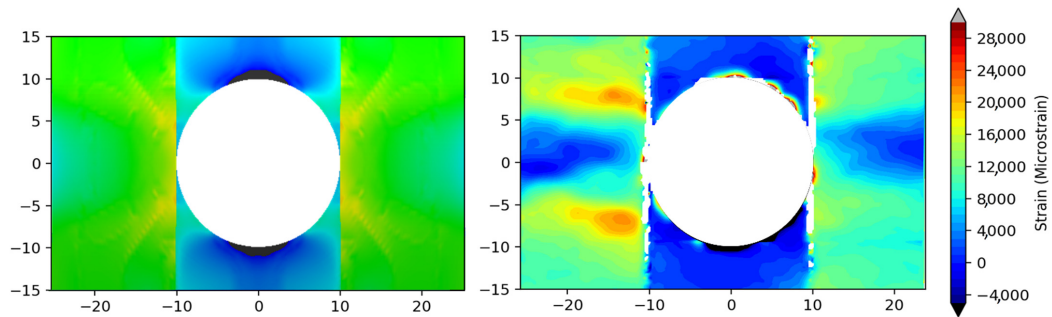

Figure 20. Hoop strain contour plot of FEA Model D at 80,000 cycles (left) compared to the experimentally measured strain (right). The color scale for the strains is the same in both plots. Both plots are for the outer ply.
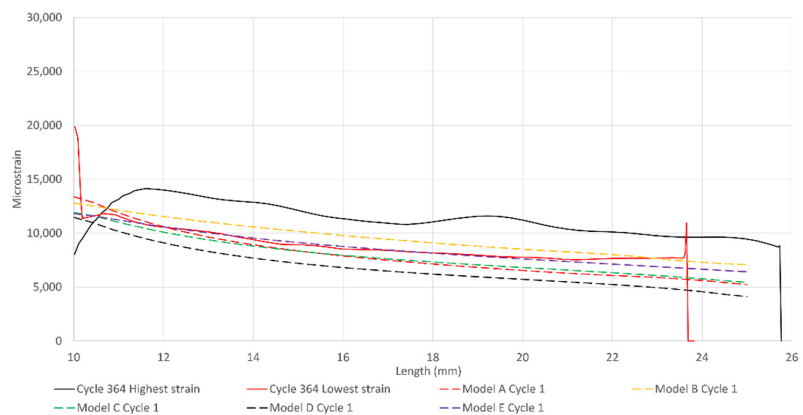

Figure 21. Lowest and highest hoop strain at cycle 364 from Figure 18 compared to the analysis results at cycle 1.

While the low strain curve from the experiment is relatively smooth throughout cycling (Figures 21–24), the high strain curve is not. The high strain curve has also got considerably greater mean strain. The strain curves when using matrix crack models C and D can be seen to have the same uneven shape and also a greater mean strain. The unevenness and greater magnitude are due to more matrix damage. It is interesting to see that the modeled strains start to fluctuate for the highly degraded matrix properties, even though the model treats the properties as the same throughout the model. The black curve in Figure 18 has the same tendency, which is the curve from the region with first observed fiber failure and also catastrophic failure. While the matrix properties are well described using the chosen envelope of degradation in models A–D, it is evident from the 127,000 cycle curves in Figure 24 that strain fields after the bottom hoop layer failure are not as well described as when predominantly matrix damage is present as for cycles 1–80,000. The experimental strains are about 40% greater than the simulated strains after first experimental layer failure. Model D can also be seen to have a substantial fiber failure at 127,000 cycles, which the other models do not have. It is, however, not consistent with where the experimental fiber failure occurred, which was at about 22 mm along the length axis in Figure 24, as commented in the Experimental Results section. The fact that the fiber failure location deviated from the experimental results was the main motivation for

disabling the fiber failure degradation in Model E. Additionally, the drastic stiffness change of fiber failure caused an extensive runtime for Model D.
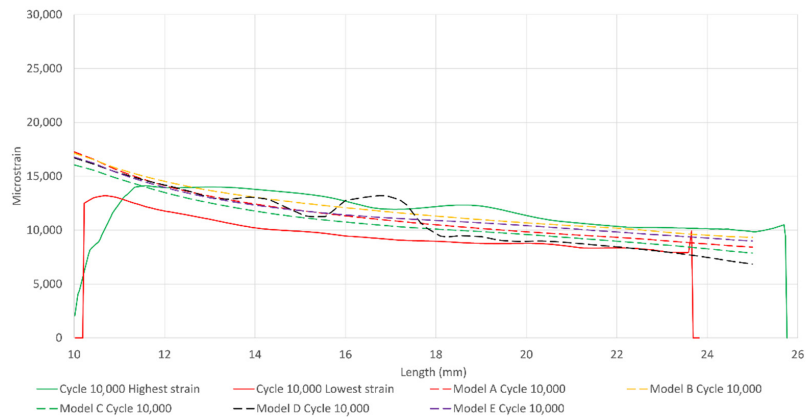

Figure 22. Lowest and highest hoop strain at 10,000 cycles from Figure 18 compared to the analysis results.
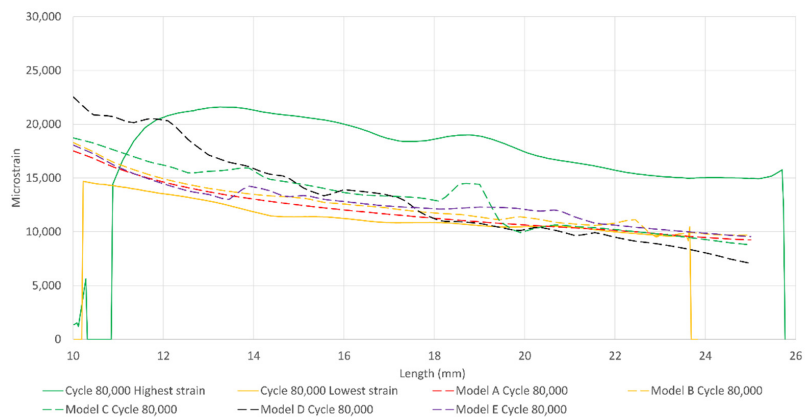

Figure 23. Lowest and highest hoop strain at 80,000 cycles from Figure 18 compared to the analysis results.

Figure 25 shows the peak exposure factor for the 22, 33, 12, 13, and 23 (matrix) components for the outer ply. The maximum was in all cases in the 22 direction. There is a region to the right of the hole at the split with a high exposure factor, corresponding with the high experimental hoop strain region in Figures 21–24. As can be seen, models A–E predict an increasing amount of matrix damage. It can be seen that the degree of strain fluctuations in the model's hoop strain graphs corresponds to the degree of matrix damage.

The FEA calculations for the onset of fiber failure (first recorded fiber exposure factor above 1.0 in any integration point) are shown in Table 6, from Equation (6). Initial fiber failure was predicted to happen in the inner hoop layer in all cases, same as in the experiment. For Model A and B it was predicted at the equator of the hole, while for models C–E it occurred at the end of the splits. The table and cycle numbers will later be discussed and suggested as design criteria.
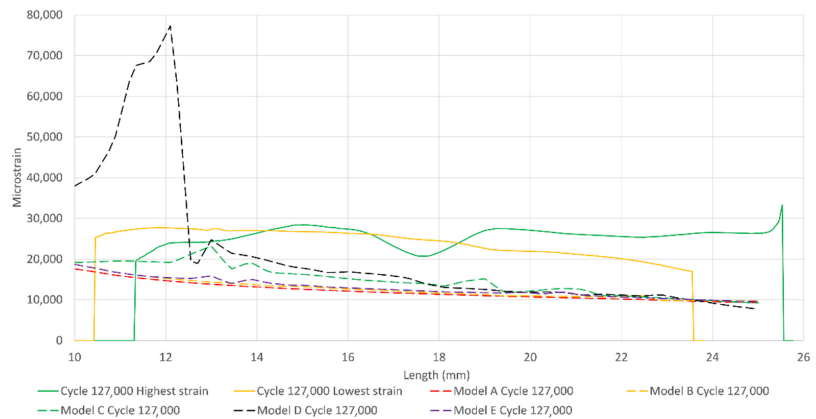
Figure 24. Lowest and highest hoop strain at 127,000 cycles from Figure 18 compared to the analysis results.
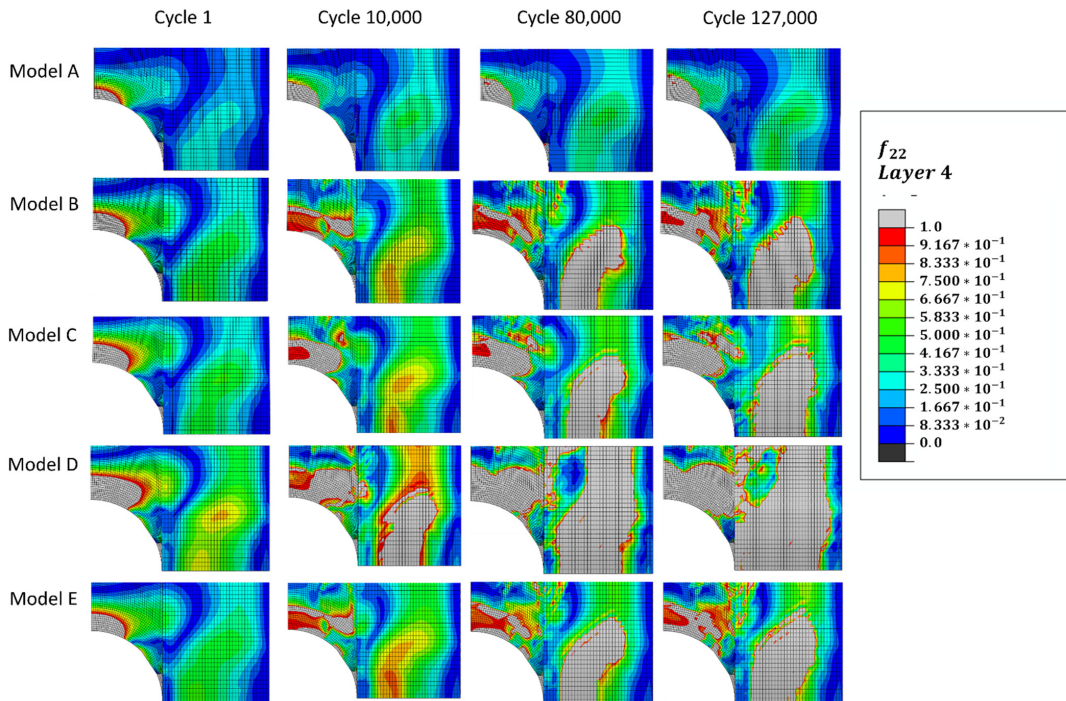
Figure 25. Exposure factor for matrix dominated fatigue failure (22 component of the surface ply). The scale is from 0 to 1.

Figure 26 shows the FEA calculated exposure factor in the fiber direction for model A, D, and E at 80,000 cycles for the bottom hoop layer. While Model A has relatively little damage in the fiber direction, Model D can be seen to have extensive damage, nearly half the load bearing cross section of the layer has an exposure factor above 1.0. Model E falls in between the two others. Model B and C are not shown; these were also in between A and D in damage extent. Catastrophic failure of the ring happened at 127,814 cycles. At that number of cycles the FEA predicted strains were lower than the experimental strains, as described above, so the accuracy of the FEA model was not too good anymore. This is

evidently due to the fact that catastrophic failure of the bottom hoop layer in the model is very difficult to model correctly. Any exposure factor evaluation in top hoop layer is there for difficult to evaluate and will not be presented.

Table 6. First fiber failure in models A–D.

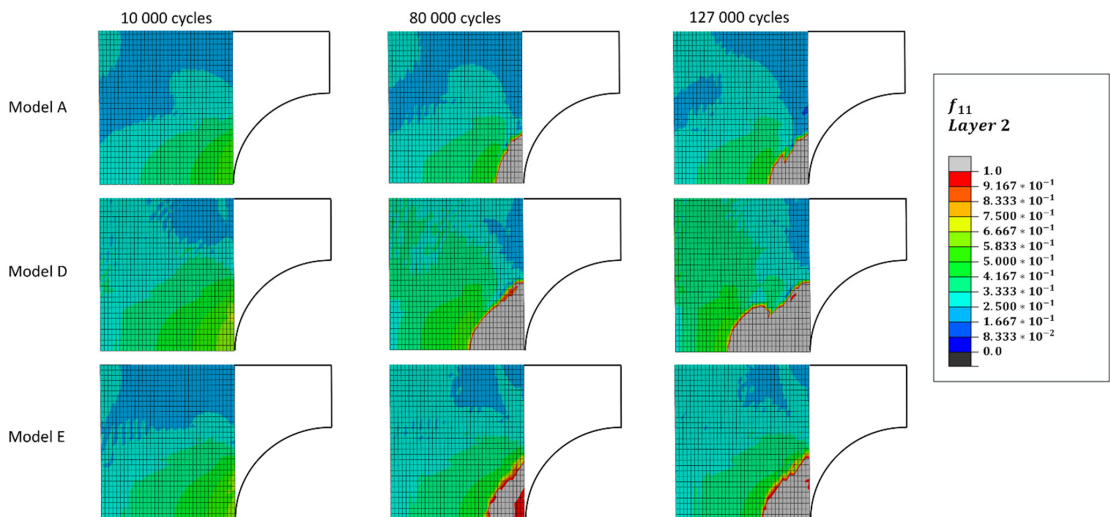| Model	Onset of Fiber Failure	Location
Model A	19,930 cycles	Hole equator
Model B	19,930 cycles	Hole equator
Model C	16,390 cycles	Split
Model D	11,400 cycles	Split
Model E	11,400 cycles	Split

Figure 26. Exposure factor in the fiber direction of the bottom hoop layer at 80,000 cycles. Only one side of the shear crack is shown as damage developed there.

While the strain plots give a good overview of the local behavior of the ring specimen, the displacement curve gives a good indication of how changes to the local stiffness affect the global behavior. Figure 27 shows Models A–E compared to the displacement from the experiment. All models predict a rapid increase in displacement within the first 10,000 cycles. This increase is due to developing matrix damage, making the sample more compliant. The experimental curve shows that this damage develops much faster, mostly within the first cycle. The discrepancy is due to the fact that the cycle 1 step was run without any damage in the FEA analysis. This is different from the experiment, where the cycle 1 loading gave initial matrix damage and evidently greater displacement than the models. The models converge with the experiment after the second step at 10,000 cycles. Putting in more cycle jumps would reduce the discrepancy, but since the focus of this study is not on the short-term behavior, no further investigations of this phase were done.

Further matrix cracking created a gradual increase of displacement for all models. The increase was lowest for model A and highest for model D, as would be expected from the material properties used in the models given in Table 4. The experimental data show a mainly flat curve up to 80,000 cycles and then a gradual increase in displacement. However, within an error of about 10% models A, B, and C match the experimental data, models C and E being the best. Model D gives a much too compliant behavior.
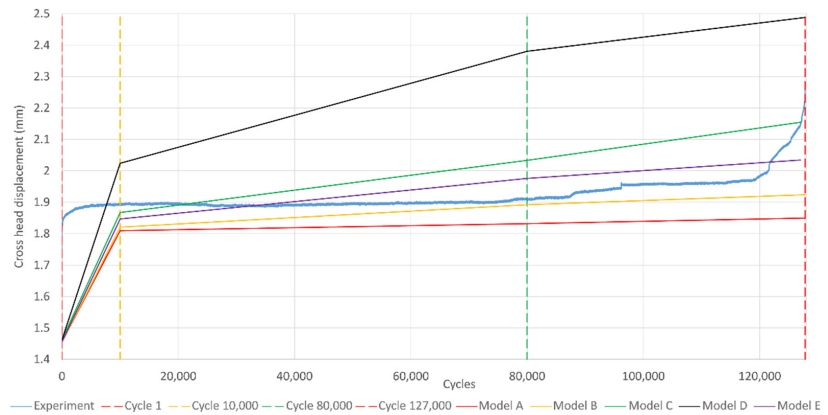
Figure 27. The displacement differential from the experiment and test compared.

The displacement curves show that the models did not properly account for spreading of fiber failure. Displacement increases due to matrix cracking were, however, relatively well described, as evident between 1 to 10,000 cycles. The experimentally observed jumps in the displacement curve due to fiber failure are difficult to capture with such few cycle jumps.

The macro shear crack length is shown in Figure 28. The crack length is defined as the length of the crack where the cohesive parameters $\delta_0/t_n/t_t/t_s$ in Figure 7 were exceeded. The shear crack length as defined by the gaps in the DIC contour plot (see Figures 17 and 20) is shorter than this, as voids first come when there is a visual shear crack. It can however be seen that shear crack modeled by FEA extended outside the frame of the DIC (15 mm) for all the models at almost all cycles.
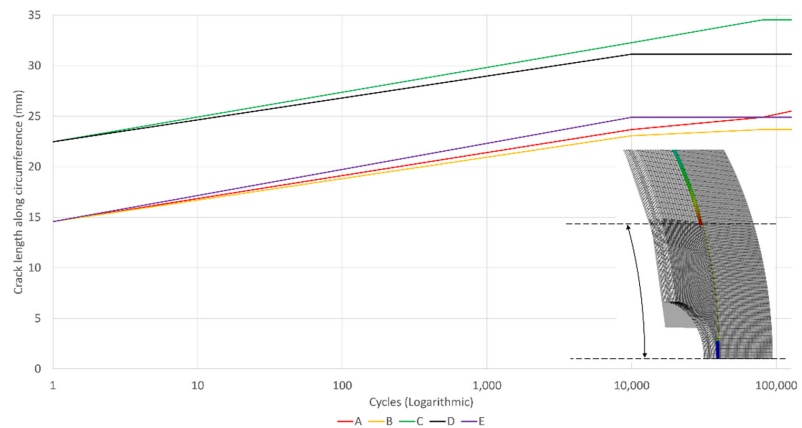
Figure 28. Shear crack length (length that has breached δ_0 in Figure 7) along the circumference of the FEA model.

Delaminations were not measured experimentally except for some visual investigation of the edges of the ring specimen during testing (see Figure 29). The cracks highlighted with red arrows in Figure 29 are evidently macro cracks, but were not included in the model as they have much less effect on the strain distribution in the loadbearing layers compared to cracks in the hoop layers, while also being harder to predict. Figure 30 shows the delaminations in the models between layer 3 and 4, as they were the most extensive. As can be seen, the delaminations differ from the experiment when comparing Figures 29 and 30. The delaminations in

the experiment run through the equator between layer 3 and 4 and are more extensive than in the model. The discrepancy is likely due to the fact that the macro cracks created free edges inside the specimen which delaminations could grow from due to more shear stress in the layer interfaces. The cracks on their own reduced the bending stiffness while also causing delaminations to grow and are the likely reason for the apparent low bending stiffness of the material in the split. The low bending stiffness gives the low strain in the center of the disk in the experiment compared to the model, as shown in Figure 20.

Figure 29. Macro cracks (red arrows) extending through the middle axial layer with delamination on either side of the middle axial layer (green arrows).
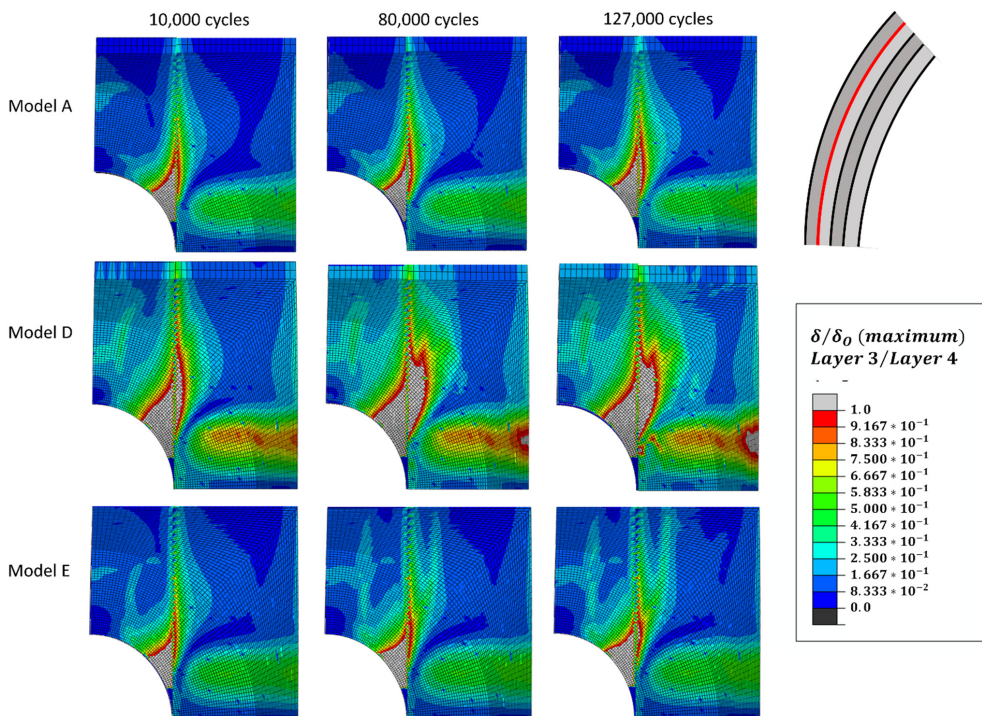

Figure 30. FEA delamination between the most delaminated layers in the model, layer 3 and 4, as indicated in the schematic.

7. Discussion

The experimental strain field measurements performed by high frequency DIC have shown that the local variations in material properties significantly change the strain. Figures 17 and 18 show the differing strains in the highly strained and critical regions. Using simple symmetry arguments, the strains in the four quadrants around the hole of the ring test should be the same for a component with identical material properties.

The local changes in material properties are a result of the production process and natural variations in material properties. Especially for the filament wound material investigated here, local variations in fiber content, fiber placement, and presence of voids are quite pronounced, amplifying these effects compared to better-controlled materials, such as prepregs. However, to some extent these variations are present in all composite materials.

Modeling the random variations of the material´s behavior is a challenge. This work used a simplified approach by modeling the ring specimens several (five) times with a constant set of material properties for each modeling run. The initial matrix properties and their degradation characteristics were changed for the different runs. The high frequency DIC measurements allowed comparing experimental fatigue strains with FEA simulations on a high level of detail.

Looking at up to 80,000 cycles, the comparison showed that the nominal material properties (model A) described the least damaged parts of the specimen well. Model D with degraded properties described the most damaged part of the specimen well. Model B, C, and E were between the two. Modeling the entire specimen with a constant set of matrix properties is not ideal, as it deviates from the real physical conditions, but the agreement between experiments and FEA shows that this simplified approach manages to capture the strain envelope reasonably well. The approach should be sufficient for most practical purposes. Model D was the only model that had enough fiber damage to show on the strain curves, with strains in the fiber direction up to 0.8%. However, the fiber failure occurred at a different spot from the experiment. Seeing as the modeling method did not capture fiber failure correctly, Model E was run without any degradation of fiber failure associated properties and with degradation of matrix properties in between Model D and Model C.

The FEA calculates that the first local fiber failure happens already at 10,000–20,000 cycles for all models. This is the first point in the models with an integration point showing an exposure factor above 1.0 for the fiber direction. Due to the initial matrix cracking phase being more or less the same for all models, the first registered exposure factor above 1.0 falls within a short cycle window. However, as stated above, it was concluded that the method falls short of modelling catastrophic fiber failure correctly. The reason being that the experiment consisted of many strong and weak fibers, while the model treats all fibers the same. Such a drastic event as fiber failure therefore becomes difficult to model correctly due to statistical variations in the experiment. To model it better, some failure criteria that initiate fiber failure when a region of a certain size has an exposure factor above 1.0 may be better. However, this is a computationally expensive approach. The modelling method in Model E may therefore be the most fit for purpose as it gives the user an idea of how big a region may give fiber failure without the added computational cost of modeling the failure (relative to the other models, Model E was computationally faster with less iterations). Knowing when the exposure factor in the fiber direction reaches 1.0 in the model may be a good design input, as it occurs about a decade before catastrophic failure, which gives a reasonable safety factor for design purposes. Most importantly, the modelling gives a good indicator of how the strain fields will develop throughout the fatigue life. As can be seen, the general trend is the same for all models, with a flattening of the strain field with increasing cycles and damage. Considering the material model's poor ability to correctly model the progression of fiber failure, but good capability to model matrix damage, it can be said that it is more fit for modelling components with a high cycle fatigue issue rather than low cycle.

After initial local fiber failure, further local fiber failures develop according to the FEA. As shown in Figure 26, the region with local fiber damage spreads mainly in the

loading/hoop direction along the splits and across the width of the specimen. The first global response from fiber damage between 80,000 and 90,000 cycles, as seen in Figure 16, is due to an accumulation of local fiber failure that can connect via matrix damage to create a more global crack. The current FEA model is not capable of describing the accumulation of fiber damage properly, as element deletion or contact breaching has to be used in addition to stiffness reduction of the elements to properly characterize the failed regions. Such routines are computationally expensive. The FEA model should be accurate up to first fiber failure. Afterwards, the model shows reasonably well what is happening in the ring specimen, but it should be seen more as a qualitative characterization. Model D and E with the weak matrix describe much more fiber damage than models A, B, and C with a stronger matrix, as would be expected.

Catastrophic failure happens at 127,814 cycles; a decade after the first fiber failure was predicted. The progressive development of damage leads to fluctuations in the strain field across the width, both in FEA predictions and in experimental DIC measurements. It seems that these fluctuations indicate the onset of serious fiber damage, damage that leads to a global response of the structure. The first fluctuations were already seen for the C, D, and E models at 80,000 cycles, see Figure 23. The fluctuations are very pronounced at 127,000 cycles, see Figure 24, even though the absolute strain values between experiment and FEA do not agree too well. These fluctuations could potentially be used as a non-destructive evaluation (NDE) method indicating imminent catastrophic failure. Qualitatively it can be observed that local fiber failures develop and spread without causing a recognizable global response. Matrix damage increases in parallel. Once a combination of local fiber damage and sufficient matrix damage exists, the benign local fiber failures can rapidly combine into global fiber damage causing macroscopic/catastrophic failure.

The FEA used here addresses all failure mechanisms and degradation of material properties after failure, creating a full progressive mechanical fatigue analysis. It is based on very simple maximum strain failure criteria and easily obtained material data. Nevertheless, the set of input data needed is large, as shown in Table 2. The good agreement with experimental results up to first fiber failure is an indication that the modeling approach was successful. It is worth looking at some of the simplifications made. All micro failure mechanisms, axial and shear matrix cracking, and local fiber failure, are described by simple non-interacting maximum strain criteria. The scatter in experimental data, especially the large effects of locally varying material properties, dominates the result, making the simple failure criteria adequate. Whether the simple criteria would also work under more complex multiaxial loading conditions is currently unclear and would need further experimental work to find the answer. In principle the cycle jump approach described here can be easily extended to more complex failure criteria if needed.

Another simplification was to prescribe in advance that the dominant shear crack would develop from the equator of the hole in the ring specimen parallel to the load direction in the hoop layers. This simplification reduced the computational effort significantly. For simple and well-defined loading conditions, the position of the shear cracks can be easily estimated in advance and possibly confirmed by simple experiments. The experimentally observed axial cracks were not modeled in advance and subsequently ignored by the FEA. It was argued here that these cracks were not critical for the ring specimens tested. In principle such cracks could be easily added. If the loading directions are completely unknown, the prescribed crack direction can be a severe limitation and the macro shear crack will matter more, as investigated by Turon [7].

The planes in which delaminations would develop were prescribed in the same way as for the shear cracks. This simplification should work well under most loading conditions. However, the method for defining the macro matrix crack and delamination is somewhat in contrast to other studies covering this topic, taking a highly simplified approach. Figure 28 shows the crack length defined through breaching of δ_0 in Figure 7. Compared to the gaps in the strain field in Figure 20 it may appear that the actual shear crack is shorter than the modeled; however, the gaps may appear long after the material has cracked and certainly

long after the elastic regime defined by δ_0 is breached. The gaps simply indicate when the DIC is not able to pick up any displacement in the speckle pattern. The key role of the shear crack from a strain distribution perspective is to hinder transfer of shear strain across the crack line leading to a greater strain at the 10 mm position in the strain graphs in Figures 21–24. The strain at the 10 mm position in the curves in Figures 21–24 varies very little even though the C and D models have a shear crack twice as long as the A and B models. This indicates that for the split disk ring, the shear crack length is not critical for getting the right strain field in the peak strain regions as long as the crack is longer than a certain minimum. This is an attribute of the modeled geometry. In other applications the macro shear crack will matter more, as investigated by Turon [7]. For future work, it could be possible to combine the methods from the UMAT in this work into a UEL with CZM. As demonstrated by Rozylo [20], the CZM approach is robust and able to predict crack paths in complex strain fields. With the cycle jump approach in the UMAT presented here it would be possible to make a UEL that takes into account both macro and micro cracking, making for a very robust progressive fatigue model. The runtime would very likely be an issue; however, simpler models than the one in this study would be sufficient to serve as a proof of concept and with the computers of tomorrow runtime may not be a worry in the future.

Another simplification was the use of the cycle jump method. As found in previous studies, the method seems to work well. The analysis steps were chosen here based on experimental results. It was a convenient way to identify the critical steps, but only possible if experimental data are available. To increase applicability and improve accuracy, a better estimation of cycle jumps would be needed. This could be done by convergence of strain or damage over time by running several models with different cycle jumps. These models could be more coarsely meshed or only contain parts of the full model. More elaborate approaches to estimate cycle jump size and position already exist for simpler models [7,15,23] and should be possible to implement on larger models as well.

It seems a good balance of simplicity of the FEA and accuracy of the results was found for this study. Adding more complexity to the FEA, especially fiber matrix interaction effects and cycle jump iteration schemes, may get closer to the physics of the behavior of the composite, but also increases dramatically the computational effort. Whether a more complex model will improve the results remains to be seen, because usually further uncertain assumptions need to be added on a detailed level. The variation in material properties remains in all cases and requires using a worst-case approach for design calculations at the end.

Traditional design calculations would use S-N curves for fiber dominated failure obtained from coupon tests and apply them to the stress/strain concentration points in the structure. For this material an S-N curve with the origin at 22,150 microstrain [36] would yield very conservative first fiber failure estimates. In this study the highest strain near the hole was around 1.5 to 1.8%. This would lead to 100 to 1000 cycles to failure, far below the actual catastrophic failure. The reason for the mismatch is using an S-N curve describing large catastrophic failure on the scale of a few cm to local non-critical damage development at a stress concentration.

The FEA shown here uses an S-N curve describing local fiber failure taking local material variations of the matrix into account. This curve is more realistic for use in stress/strain fields with large gradients. Since the accuracy of the FEA currently drops after first local fiber failure, a designer could use the first fiber failure for the weak material D as a design criterion. The predicted cycles to failure are then 10,000, which are much more than predicted by the traditional method. It should still be a reliable approach, because the FEA is fully capable of reproducing local strain fields. This approach is basically designing for first ply failure, a method widely used for static analysis. The approach has been applied before in the FADAS mechanical fatigue model for simple test coupons by Passipoularidis et al. [48]. The FEA can be used further to estimate the location of final

catastrophic failure and it could indicate how the strain fluctuations would look that would develop as a warning before catastrophic failure.

8. Conclusions

A finite element analysis (FEA) material model describing mechanical fatigue of composites by a progressive degradation model using the cycle jump method was developed. It is aimed at pressure vessel applications and focuses on fatigue behavior under tensile load cases, such as that found in industrial pressure vessels. It uses typical failure criteria for transversely orthotropic materials and degrades the stiffness in each material direction based on the Miner sum damage calculation with log-log S-N curves. The model is relatively simple and requires only the typical input parameters used for composite laminate analysis.

Strain fields from FEA were compared with DIC strain fields from split disk testing of a composite ring specimen. Extensive variations in damage development and strain fields were measured by DIC over the specimen due to variations in void content, layer thickness, and fiber volume fraction. The strain in the four regions around the split disk hole varied with a factor of 1.5 to 2 at the most over the course of cycling. To address the variations, the FEA model was run with a parameter study on matrix properties. The most damaged regions (with strain 1.5 to 2 times higher than the least damaged) were best modeled by using S-N curves for matrix properties degraded by 40% compared to the original values. The original values described damage in the regions with less defects well. The experimental strain fields fell at or between the modelled material cases, showcasing how much variation there can be in a typical filament wound material. Considering the 1.5 to 2 factor difference, a reduction of 40% in strength for the matrix can be considered reasonable.

Initial fiber failure could be characterized by an S-N curve measured locally (about 0.5 mm range) by DIC. Despite the curve´s high strength values, fiber failure was predicted conservatively within a decade of the experimental failure, much better than using traditional S-N curves obtained from typical coupon specimens. The model did, however, fall short of being able to correctly describe catastrophic fiber failure (accumulation of local fiber failures), due to its relatively simple nature and the sudden nature of catastrophic fiber failure. The experimental results showed that regions developing fluctuations in the strain fields were the areas where catastrophic fiber failure was initiated. The weak matrix model showed the same fluctuations in the FEA. These fluctuations can be measured by DIC and can be used as a warning for eminent failure. The results indicate that fiber failure and matrix failure are linked.

It can be concluded that the developed model is sufficient to model the complex strain and damage state in a split disk test if run with weak and strong matrix properties. The model is able to show how the strain fields develop and what shape the fields will attain in regions suspect to catastrophic fiber failure.

Author Contributions: Conceptualization, E.H., N.P.V. and A.T.E.; methodology, E.H. and A.T.E.; software, E.H.; validation, E.H., N.P.V. and A.T.E.; formal analysis, E.H.; investigation, E.H.; resources, E.H.; data curation, E.H.; writing—original draft preparation, E.H.; writing—review and editing, E.H., N.P.V. and A.T.E.; visualization, E.H.; supervision, N.P.V. and A.T.E.; project administration, E.H. and A.T.E.; funding acquisition, A.T.E. All authors have read and agreed to the published version of the manuscript.

Conflicts of Interest: The authors declare no conflict of interest.

Glossary

	General	Material Direction Specific
Material direction, with examples:		ij
Fiber direction	-	11
Matrix direction	-	22
In plane shear direction	-	12
Through thickness direction	-	33
General sign of peak/max value	^	$\hat{ij}^-$
Tensional property	T	ijT
Compressive property	C	ijC
Strain	ε	ε_{ij}
Residual strain	ε_{res}	$\varepsilon_{res,ij}$
Cycles	N	-
E-modulus	E	E_{ij}
Shear modulus	G	G_{ij}
Traction components:		
Normal component (Mode I)	n	
First shear component (Mode II)	s	
Second shear component (Mode III)	t	
Max traction	t	t_n, t_s, t_t
Contact stiffness	K	K_n, K_s, K_t
Fracture energy	G	G_n, G_s, G_t
Separation	δ	$\delta_n, \delta_s, \delta_t$
Max separation	δ_f	$\delta_{fn}, \delta_{fs}, \delta_{ft}$
Max elastic separation	δ_0	$\delta_{0n}, \delta_{0s}, \delta_{0t}$
Property at a given number of cycles N	^{N}	$^N_{ij}$
Exposure factor		f_{ij}
Slope of S-N curve	α	α_{ij}
Origin of S-N curve	^{O}	$^O_{ij}$
Cumulative damage (Miner sum)	M	M_{ij}
Property in a load block in a Miner sum.		^{k}
Example of symbols:		
Intercept in tensional fatigue curve for fiber		$\hat{\varepsilon}^O_{11T}$
Max static strain in tensional transverse (matrix) direction		$\hat{\varepsilon}_{22T}$

References

1. US Departement of Energy (DOE)/GO-102005-1741. Hydrogen, fuel cells and infrastructure technologies program. Multi-Year Research. In *Development and Demonstration Plan*; US Departement of Energy: Washington, DC, USA, 2005.
2. Crawford, M. Virtual Testing of Composite Pressure Vessels. The American Society of Mechanical Engineers. 2020. Available online: https://www.asme.org/topics-resources/content/virtual-testing-of-composite-pressure-vessels (accessed on 17 June 2020).
3. Leh, D.; Saffré, P.; Francescato, P.; Arrieux, R. Multi-sequence dome lay-up simulations for hydrogen hyper-barcomposite pressure vessels. *Compos. Part A* **2013**, *52*, 106–117. [CrossRef]
4. Ribeiro, M.L.; Vandepitte, D.; Tita, V. Damage Model and Progressive Failure Analyses for Filament Wound Composite Laminates. *Appl. Compos. Mater.* **2013**, *20*, 975–992. [CrossRef]
5. Gentilleau, B.; Bertin, M.; Touchard, F.; Grandidier, J.-C. Stress analysis in specimens made of multi-layer polymer/composite used for hydrogen storage application: Comparison with experimental results. *Compos. Struct.* **2011**, *93*, 2760–2767. [CrossRef]
6. Berro Ramirez, J.P.; Halm, D.; Grandidier, J.-C.; Villalonga, S.; Nony, F. 700 bar type IV high pressure hydrogen storage vessel burst—Simulation and experimental validation. *Int. J. Hydrogen Energy* **2015**, *40*, 13183–13192. [CrossRef]
7. Turon, A.T. *Simulation of Delamination in Composites under Quasi-Static and Fatigue Loading Using Cohesive Zone Models*; University of Girona: Girona, Spain, 2006.
8. Talreja, R.; Watt, W. Fatigue of composite materials: Damage mechanisms and fatigue-life diagrams. *Proc. R. Soc.* **1981**, *378*, 1775.
9. Pupurs, A.; Varna, J. Modeling mechanical fatigue of UD composite: Multiple fiber breaks and debond growth. In Proceedings of the 5th International EEIGM/AMASE/FORGEMAT Conference on Advanced Materials Research, Nancy, France, 5 November 2009.
10. Curtis, P.T. Tensile fatigue mechanisms in unidirectional polymer matrix composite materials. *Int. J. Fatigue* **1991**, *13*, 377–382. [CrossRef]

11. Harik, V.M.; Klinger, J.R.; Bogetti, T.A. Low-cycle fatigue of unidirectional. *Composites Int. J. Fatigue* **2002**, *24*, 455–462. [CrossRef]
12. Lemaitre, J.; Sermage, J.P.; Desmorat, R. A two scale damage concept applied to fatigue. *Int. J. Fract.* **1999**, *97*, 67–81. [CrossRef]
13. Turon, A.; Costa, J.; Camanho, P.P.; Dávila, C.G. Simulation of Delamination in Composites under High-Cycle Fatigue. *Compos. Part A Appl. Sci. Manuf.* **2007**, *38*, 2270–2282. [CrossRef]
14. Mandell, J.F.; Huang, D.D.; McGarry, F.J. Fatigue of Glass and Carbon Fiber Reinforced Engineering Thermoplastics. *Polym. Compos.* **1981**, *2*, 137–144. [CrossRef]
15. Nixon-Pearson, O.J.; Hallett, S.R.; Harper, P.W.; Kawashita, L.F. Damage development in open-hole composite specimens in fatigue. Part 2: Numerical modelling. *Compos. Struct.* **2013**, *106*, 890–898. [CrossRef]
16. Harper, P.W.; Hallett, S.R. A fatigue degradation law for cohesive interface elements—Development and application to composite materials. *Int. J. Fatigue* **2010**, *32*, 1774–1787. [CrossRef]
17. NASA CompDam—Deformation Gradient Decomposition (DGD). NASA. 2019. Available online: https://github.com/nasa/CompDam_DGD (accessed on 20 January 2019).
18. Flatscher, T.; Pettermann, H.E. A constitutive model for fiber-reinforced polymer plies accounting for plasticity and brittle damage including softening—Implementation for implicit FEM. *Compos. Struct.* **2011**, *93*, 2241–2249. [CrossRef]
19. Gagani, A.I.; Kraukalis, A.; Sæter, E.; Vedvik, N.P.; Echtermeyer, A.T. A novel method for testing and determining ILSS for marine and offshore composites. *Compos. Struct.* **2019**, *220*, 431–440. [CrossRef]
20. Rozylo, P. Experimental-numerical study into the stability and failure of compressed thin-walled composite profiles using progressive failure analysis and cohesive zone model. *Compos. Struct.* **2021**, *257*, 113303. [CrossRef]
21. Brunbauer, J.; Gaier, C.; Pinter, G. Computational fatigue life prediction of continuously fibre reinforced multiaxial composites. *Compos. Part B* **2015**, *80*, 269–277. [CrossRef]
22. Safe Technology Limited. *Safe. Technology Limited: Produktinformationsblatt Fe-Safe/Composites Powered by He-Lius: Fatigue—Composite Durability Analysis Software for Finite Element Models*; Sheffield, Safe Technology Limited: Sheffield, UK, 2010.
23. Koch, I.; Zscheyge, M.; Tittmann, K.; Gude, M. Numerical fatigue analysis of CFRP components. *Compos. Struct.* **2017**, *168*, 392–401. [CrossRef]
24. Sevenois, R.D.B.; Garoz, D.; Gilabert, F.A.; Spronk, S.W.F.; Paepegem, W.V. Microscale based prediction of matrix crack initiation in UD composite plies subjected to multiaxial fatigue for all stress ratios and load levels. *Compos. Sci. Technol.* **2017**, *142*, 124–138. [CrossRef]
25. Chambers, A.R.; Earl, J.S.; Squires, C.A.; Suhot, M.A. The effect of voids on the flexural fatigue performance of unidirectional carbon fibre composites developed for wind turbine applications. *Int. J. Fatigue* **2006**, *28*, 1389–1398. [CrossRef]
26. Chowdhury, K.A.; Talreja, R.; Benzerga, A.A. Effects of Manufacturing-Induced Voids on Local Failure in Polymer-Based Composites. *J. Eng. Mater. Technol.* **2008**, *130*, 021010. [CrossRef]
27. Sisodia, S.; Gamstedt, E.K.; Edgren, F.; Varna, J. Effects of voids on quasi-static and tension fatigue behaviour of carbon-fibre composite laminates. *J. Compos. Mater.* **2014**, *49*, 2137–2148. [CrossRef]
28. Niewiadomski, P.; Hoła, J. Failure process of compressed self-compacting concrete modified with nanoparticles assessed by acoustic emission method. *Autom. Constr.* **2020**, *112*, 103111. [CrossRef]
29. Hugaas, E.; Echtermeyer, A. Filament wound composite fatigue mechanisms investigated with full field DIC strain monitoring. *Open Eng.* **2021**, *11*, 401–413. [CrossRef]
30. Hugaas, E.; Echtermeyer, A.T. Estimating S-N curves for local fiber dominated fatigue failure in ring specimens representing filament wound pressure vessels with damage. *Compos. Part C Open Access* **2021**, *5*, 100135. [CrossRef]
31. Golewski, G.L. Evaluation of fracture processes under shear with the use of DIC technique in fly ash concrete and accurate measurement of crack path lengths with the use of a new crack tip tracking method. *Measurement* **2021**, *181*, 109632. [CrossRef]
32. 3B. *HiPertex W2020 Datasheet*; 3B: Hoeilaart, Belgium, 5 May 2015.
33. Momentive. *Technical Datasheet Epikote Resin MGS RIMR 135 and Epikure Curing Agent MGS RIMH 134—RIMH 137*; Momentive: New York, NY, USA, 5 May 2006.
34. Hashin, Z. Cumulative damage theory for composite materials: Residual life and residual strength methods. *Compos. Sci. Technol.* **1985**, *23*, 1–19. [CrossRef]
35. Diehl, T. Modeling Surface-Bonded Structures with ABAQUS Cohesive Elements: Beam-Type Solutions. In Proceedings of the ABAQUS User's Conference, Boston, MA, USA, 25–27 May 2004.
36. Perillo, G. Numerical and Experimental Investigation of Impact Behaviour of GFRP Composiites. Ph.D. Thesis, NTNU—Norwegian University of Science and Technology, Trondheim, Norway, 2014.
37. Toubal, L.; Karama, M.; Lorrain, B. Damage evolution and infrared thermography in woven composite laminates under fatigue loading. *Int. J. Fatigue* **2006**, *28*, 1867–1872. [CrossRef]
38. Perillo, G.; Vedvik, N.P.; Echtermeyer, A.T. Numerical and experimental investigation of impact on filament wound glass reinforced epoxy pipe. *J. Compos. Mater.* **2014**, *49*, 723–738. [CrossRef]
39. Ramesh, T. Fatigue of Composite Materials. In *Modern Trends in Composite Laminates Mechanics*; Altenbach, H., Becker, W., Eds.; International Centre for Mechanical Sciences (Courses and Lectures); Springer: Vienna, Austria, 2003; Volume 448.
40. Zhang, Z.; Hartwig, G. Relation of damping and fatigue damage of unidirectional fibre composites. *Int. J. Fatigue* **2002**, *24*, 713–718. [CrossRef]

41. Broutman, L.J.; Sahu, S. A New Theory to Predict Cumulative Fatigue Damage in Fiberglass Reinforced Plastics. In Proceedings of the Composite Materials: Testing and Design (Second Conference), Anaheim, CA, USA, 20–22 April 1971; ASTM International: West Conshohocken, PA, USA, 1972; Volume ASTM STP 497, pp. 170–188.

42. Owen, M.J.; Bishop, P.T. Fatigue properties of glass-reinforced plastics containing a stress concentrator. *J. Phys. D Appl. Phys.* **1973**, *6*, 2057–2069. [CrossRef]

43. Eliopoulos, E.N.; Philippidis, T.P. A progressive damage simulation algorithm for GFRP composites under cyclic loading. Part I: Material constitutive model. *Compos. Sci. Technol.* **2011**, *71*, 742–749. [CrossRef]

44. Davies, P.; Kausch, H.H.; Williams, J.G. Round-robin interlaminar fracture testing of carbon-fibre-reinforced epoxy and PEEK composites. *Compos. Sci. Technol.* **1992**, *43*, 129–136. [CrossRef]

45. Tsai, G.-C. Design of Composite ENF Specimens and Conduct Three-Point Test to Calculate Mode II Fracture Toughness. In Proceedings of the 9th International Conference on Engineering Education, San Juan, Puerto Rico, 7 July 2006.

46. Davies, P.; Blackman, B.R.K.; Brunner, A.J. Standard Test Methods for Delamination Resistance of Composite Materials: Current Status. *Appl. Compos. Mater.* **1998**, *5*, 345–364. [CrossRef]

47. Chen, J.F.; Li, S.Q.; Bisby, L.A.; Ai, J. FRP rupture strains in the split-disk test. *Compos. Part B Eng.* **2011**, *42*, 962–972. [CrossRef]

48. Passipoularidis, V.A.; Philippidis, T.P. Fatigue life prediction in composites using progressive damage modelling under block and spectrum loading. *Int. J. Fatigue* **2011**, *33*, 132–144. [CrossRef]